Electronic structure and ultrafast fragmentation dynamics of polycyclic aromatic hydrocarbons

DISSERTATION

zur Erlangung des Doktorgrades
an der Fakultät für Mathematik, Informatik und Naturwissenschaften
Fachbereich Physik
der Universität Hamburg

angefertigt am
Deutschen Elektronen-Synchrotron,
ein Forschungszentrum der Helmholtz-Gemeinschaft

Diksha Garg

Hamburg, Deutschland
2023

Gutachter der Dissertation:	Prof. Dr. Melanie Schnell
	Prof. Dr. Nils Huse
Zusammensetzung der Prüfungskommission:	Prof. Dr. Melanie Schnell
	Prof. Dr. Nils Huse
	Prof. Dr. Ludwig Mathey
	Prof. Dr. Per Eng-Johnsson
	Prof. Dr. Stefan Schippers
Vorsitzender des Prüfungsausschusses:	Prof. Dr. Ludwig Mathey
Datum der Disputation:	24.03.2023
Vorsitzender des Fach-Promotionsausschusses PHYSIK:	Prof. Dr. Günter H. W. Sigl
Leiter des Fachbereichs PHYSIK:	Prof. Dr. Wolfgang J. Parak
Dekan der Fakultät MIN:	Prof. Dr.-Ing. Norbert Ritter

List of Publications

1. D. Garg, J. W. L. Lee, D. S. Tikhonov, P. Chopra, S. Maclot, A. L. Steber, S. Gruet, F. Allum et al. "Fragmentation dynamics of fluorene explored using ultrafast XUV-Vis pump-probe spectroscopy." Frontiers in Physics (2022): 450

2. J. W. L. Lee, D. S. Tikhonov, P. Chopra, S. Maclot, A. L. Steber, S. Gruet, F. Allum et al. "Time-resolved relaxation and fragmentation of polycyclic aromatic hydrocarbons investigated in the ultrafast XUV-IR regime." Nature Communications 12, no. 1 (2021): 1-11.

3. A. K. Lemmens, P. Chopra, D. Garg, A. L. Steber, M. Schnell, W. J. Buma, and A. M. Rijs. "High-resolution infrared spectroscopy of naphthalene and acenaphthene dimers." Molecular Physics 119, no. 1-2 (2021): e1811908.

Abstract

The astrochemical importance of polycyclic aromatic hydrocarbons (PAHs) is widespread, and a complete understanding of these PAHs' photophysical and photochemical properties is of great interest to the astronomical community. The absorption of interstellar radiation by these molecules initiate various physical and chemical processes including fragmentation, ionization, and excitation. These processes are explored dynamically and statically in this thesis. The dynamic studies extract the vibronic relaxation lifetimes of the excited PAH ions and neutrals and their excited fragments, whereas the static experiments reveal the fragmentation patterns of the PAHs and the electronic structure of their cations. These studies are worked out as a part of two different experiments performed at the large-scale facilities at Deutsches Elektronen-Synchrotron (DESY) in Hamburg, namely the Positron-Elektron-Tandem-Ring-Anlage (PETRA) III and the Free-electron LASer in Hamburg (FLASH).

The first set of experiments is performed using Near Edge X-ray Absorption Fine Structure (NEXAFS) spectroscopy with the small-sized PAH phenanthrene ($C_{14}H_{10}$) in the gas phase. The electronic structure at the carbon K-edge is retrieved for the $C_{14}H_{10}^+$ and $C_{14}H_9^+$ ions. The effect of dehydrogenation on the NEXAFS spectrum can be observed as well.

In the second set of experiments, we employ ultrafast pump-probe spectroscopy using time-of-flight mass spectrometry and velocity map imaging methods. These experiments deal with disentangling the patterns of fragmentation and studying the stability of the excited states of the PAH fluorene when it interacts with intense radiation available in the laboratory, which serves as an alternative to the harsh radiation present in the interstellar medium. To target more than one type of radiation, two such experiments are performed varying the pump pulse. One, in which the fluorene molecules are irradiated with extreme ultraviolet pulses at 30.3 nm (40.9 eV photon energy), which corresponds to the He II emission. In this case, the single photon absorption is the driving mechanism for the fragmentation of fluorene giving a dense mass spectrum. In the second experiment, the fluorene interacts with highly intense near-infrared radiation, and the combination of multiphoton and tunnel ionization processes is observed.

In experiments, the extreme ultraviolet radiation from the FLASH and the

infrared radiation from a Ti:Sa optical laser have femtosecond pulse durations that are a prerequisite to observing ultrafast dynamics. The dynamics initiated in the molecules by the pump radiation (extreme ultraviolet and infrared) are probed using a femtosecond pulse in the visible spectral range with a wavelength of 405 nm, which is obtained by the second harmonic generation of Ti:Sa optical laser. The relaxation lifetimes of the vibronically excited fluorene ions in their different charge states and the subsequent fragments are shown to span durations from a few femtoseconds to a few picosecond timescales.

Using the techniques of NEXAFS spectroscopy and the time-resolved ultrafast pump-probe spectroscopy, we are able to address the elementary properties of PAHs such as electronic structure, fragmentation pathways, and vibronic relaxation lifetimes. These properties can contribute toward elucidating the fundamental properties of PAH molecular systems in their neutral and cationic form. These results give an insight into the interaction of PAHs in extreme radiation, which is pertinent to exploring the vast interstellar medium.

Kurzzusammenfassung

Die astrochemische Bedeutung von polyzyklischen aromatischen Kohlenwasserstoffen (engl. polycyclic aromatic hydrocarbons, PAHs) ist weit verbreitet und ein vollständiges Verständnis der photophysikalischen und photochemischen Eigenschaften von PAHs ist für die Astronomie von großem Interesse. Die Absorption von interstellarer Strahlung durch solche Moleküle regt verschiedenste physikalische und chemische Prozesse an, wie Fragmentation, Ionisation und Anregung. In der vorliegenden Arbeit werden die dynamischen und statischen Eigenschaften dieser Prozesse untersucht. Dynamische Studien geben Aufschluss über die vibronischen Lebensdauern von angeregten ionisierten sowie neutralen PAHs und deren angeregten Fragmenten, während statische Experimente die Fragmentationsmuster der PAHs und die elektronische Struktur ihrer Kationen entschlüsseln. Diese Studien werden an zwei Großbeschleunigern am Deutschen Elektronen-Synchrotron DESY durchgeführt, namentlich die Positron-Elektron-Tandem-Ring-Anlage (PETRA) III und der Freie-Elektronen Laser in Hamburg (FLASH).

Die erste Experimentierreihe untersucht mit Hilfe von Röntgen-Nahkanten-Absorptions-Feinstruktur-Spektroskopie (engl. Near-Edge X-ray Absorption Fine Structure, NEXAFS spectroscopy) kleinere PAHs wie Phenanthren ($C_{14}H_{10}$) in der Gasphase. Damit kann die elektronische Struktur an der Kohlenstoff K-Absorptionskante für $C_{14}H_{10}^+$ und $C_{14}H_9^+$ erhalten werden. Auch wird der Effekt der Dehydrierung auf das elektronische Spektrum beobachtet.

In einer zweiten Reihe von Experimenten wird ultraschnelle Pump-Probe Spektroskopie kombiniert mit Time-of-Flight Massenspektroskopie und Velocity Map Imaging Methoden. Diese Experimente behandeln die Aufschlüsselung von Fragmentationsmustern und die Stabilitätsstudie angeregter Zustände von dem PAH Fluoren, wenn es mit intensiver Strahlung aus dem Labor wechselwirkt, welche als Alternative zu der starken Strahlung im interstellaren Medium dient. Um verschiedene Arten von Strahlung abzudecken, wurden zwei Experimente mit unterschiedlichen Pumppulsen durchgeführt: Auf der einen Seite wurden die Fluorenmoleküle mit extrem ultravioletten (XUV) Pulsen bei einer Wellenlänge von 30,3 nm (40,9 eV Photonenenergie) bestrahlt, welches der He II Emission entspricht. In diesem Fall ist die Ein-Photon-Absorption der treibende Mechanismus für die Fragmentation von

Fluoren, was ein dichtes Massespektrum ergibt. Auf der anderen Seite wechselwirkt Fluoren im zweiten Experiment mit hochintensiver nahinfraroten (IR) Strahlung, und eine Kombination aus Multiphotonen- und Tunnelionisation wird beobachtet.

In diesen Experimenten liegen die Pulsdauern der XUV Pulse und der IR Pulse, die von FLASH bzw. von einem optischen Laser erzeugt werden, im Bereich von Femtosekunden, was eine Voraussetzung für die Beobachtung ultraschneller Dynamiken ist. Die Dynamiken, die in den Molekülen durch die Pumpstrahlung (XUV und IR) eingeleitet werden, werden mittels Femtosekundenpulsen im sichtbaren Spektralbereich bei 405 nm geprobt, welche durch die Erzeugung der zweiten Harmonischen von einem Ti:Sa Laser erhalten werden. Es wird gezeigt, dass die Relaxationszeiten der vibronisch angeregten Fluorenionen in ihren verschiedenen geladenen Zuständen und der nachfolgenden Fragmente Zeitskalen von wenigen Femtosekunden bis hin zu einigen Pikosekunden umfassen.

Die Anwendung von NEXAFS-Spektroskopie und zeitaufgelöster ultraschneller Pump-Probe-Spektroskopie ermöglicht uns, elementare Eigenschaften von PAHs wie ihre elektronische Struktur, Fragmentationsprozesse und vibronische Lebensdauern zu untersuchen und damit die Wechselwirkung zwischen PAHs und extremer Strahlung besser zu verstehen. Dieses Wissen trägt zum grundlegenden Verständnis über die molekularen Systeme von PAHs in ihrer neutralen und kationischen Form bei, die für die Erforschung des ausgedehnten interstellaren Mediums von Bedeutung sind.

to the curiosity of researchers that keeps Science growing

Abbreviations

Δt time delay between the pump and the probe pulse.

m/z mass over charge ratio.

AIB aromatic infrared band.

AM analyzer dipole magnet.

API application programming interface.

ATI above threshold ionization.

BAM bunch arrvial time monitor.

BBO beta-barium borate.

BL1 beamline 1.

CAMP CFEL-ASG Multi-Purpose instrument.

CCD charged-coupled device.

DAQ data acquisition.

DESC Delay Stage for CAMP.

DESY Deutsches Elektronen-Synchrotron.

DI double ionization.

DIB diffuse interstellar band.

DM demerger magnet.

ECRIS electron cyclotron resonance ion source.

FEL free-electron laser.

FLASH Free-electron LASer in Hamburg.

HDF5 hierarchical data format.

HOMO highest occupied molecular orbital.

IC internal conversion.

IR infrared.

ISC intersystem crossing.

ISM interstellar medium.

IVR intramolecular vibrational energy redistribution.

IYvsDelay ion yield *vs.* pump-probe delay time.

KER kinetic energy release.

LUMO lowest unoccupied molecular orbital.

MB merged-beam.

MCP microchannel plate.

MO molecular orbital.

MPI multiphoton ionization.

NEXAFS Near Edge X-ray Absorption Fine Structure.

PAH polycyclic aromatic hydrocarbon.

PETRA Positron-Elektron-Tandem-Ring-Anlage.

PImMS pixel imaging mass spectrometry.

PIPE Photon-Ion spectrometer at PETRA III.

RF radio-frequency.

SI single ionization.

SOMO singly occupied molecular orbital.

SPD single particle detector.

TD-DFT time-dependent density functional theory.

TDS transverse deflecting radio frequency structure.

TI tunnel ionization.

TOF time-of-flight.

TOF-MS time-of-flight mass spectrometry.

UIR unidentified infrared.

UMO unoccupied molecular orbital.

UV ultraviolet.

Vis visible.

VLS variable line spacing.

VMI velocity-map imaging.

XAS X-ray absorption spectroscopy.

XES X-ray emission spectroscopy.

XPS X-ray photoelectron spectroscopy.

XUV extreme ultraviolet.

Contents

Chapter 1

Introduction

1.1 PAHs and the interstellar medium

For decades there has been a steep growth in the interstellar medium (ISM) related research. The average particle number densities of the diffuse molecular clouds and dense molecular clouds in the ISM are known to be $\sim$100 to 500 cm^{-3} and $>10^4$ cm^{-3}, respectively, which is still much lower than the particle number densities achievable even *via* ultra-high vacuum pumps $\sim$10^7 cm^{-3} in the laboratory [1]. Despite this low density of the ISM, there is a rich molecular inventory with the first molecular detections taking place in the early 1930s [2–4]. After these detections, the list of molecules is still piling up consisting of over 270 molecules ranging from 2 to 70 atoms so far [5]. It is interesting to notice that this list includes a large number of organic molecules that can serve as possible precursors to prebiotic molecules.

Detection of these molecules would not have been possible without radio astronomy and rotational spectroscopy, which relies on detecting the features arising from the emission or absorption of interstellar radiation. These features are then assigned based on laboratory spectroscopy. Besides the detection of over 270 molecules, unassigned features are widespread, in particular, the features appearing in the infrared emission spectrum called unidentified infrared (UIR) bands and in the absorption spectrum called diffuse interstellar band (DIB).

The mystery of the peaks forming in the UIR bands that were measured in the 1970s and 1980s in the planetary nebula and the HII regions [6] was addressed when the vibrational modes observed in these features were attributed to polycyclic aromatic hydrocarbons (PAHs) and their clusters in neutral and cationic form [7–10], which led dubbing UIR band to aromatic infrared band (AIB). The PAHs are organic molecules comprising multiple fused benzene rings and are estimated to constitute $\sim$10% of the total galactic carbon [11–14]. It is recently, that this well-known speculation of UIR bands being attributed to the PAHs got strengthened

with the detection of pure and substituted PAHs [15–17] in the ISM.

The absorption of ultraviolet (UV), visible (Vis), and infrared (IR) radiation gives rise to the absorption spectra near the stars that are present behind the diffuse interstellar clouds. The assignment of over 300 hundred of these DIB bands is a withstanding concern to the astronomical society [18]. Amongst these, two bands could be assigned to the buckminsterfullerene in its cationic form C_{60}^+ *via* laboratory work in the year 2015 [19], which is shown in Figure 1.1a. The formation of such a large molecule in the ISM builds curiosity amongst many researchers. There are many mechanisms brought forward to understand the formation of this molecule given in Ref. [20, 21]. One mechanism of which includes the top-down approach in which large PAHs are thought to dehydrogenate, leading to curving and folding of the geometrical structure to build up fullerenes [21] as shown in Figure 1.1b. The presence of the fullerene in the cationic state diverted the interest to explore the cationic species including PAH cations. The interaction with UV radiation can lead to ionization and dehydrogenation processes in PAHs. Thus, PAH cations and their dehydrogenated and fragmented derivates are widely studied [22–24]. In this thesis, the electronic structures of cationic phenanthrene and its dehydrogenated state are investigated using Near Edge X-ray Absorption Fine Structure (NEXAFS) spectroscopy, and the dehydrogenation effect on the electronic spectrum of the cationic phenanthrene is also discussed briefly.

Apart from dehydrogenation and ionization, the interaction of PAHs with intense radiation leads to carbon backbone fragmentation. The fragmentation and ionization processes are observed to be dependent on the size of the PAHs. Ionization processes are observed to be dominant over fragmentation processes for large PAHs (e.g. coronene $C_{24}H_{12}$) as compared to the small-sized PAHs (e.g. anthracene $C_{14}H_{10}$) in the Ref. [24]. For the small-size PAHs, the fragmentation is still relevant and recent observations from the James Webb Space Telescope illustrate the destruction of this class of molecules in space [25]. In order to understand the rich molecular fragmentation dynamics of these molecules, it is important to further elucidate the preferred fragmentation pathways and timescales on which they occur. For example, the loss of acetylene units from the PAHs is an established fragmentation pathway, which supports the possibility of the well-known hydrogen abstraction acetylene addition (HACA) mechanism proposed as one of the formation mechanisms of PAHs. The acetylene units needed to form PAHs may be provided due to the destruction of other PAHs. A detailed investigation of possible fragmentation pathways would lead to a better understanding of the formation mechanisms of these astrochemically relevant molecules.
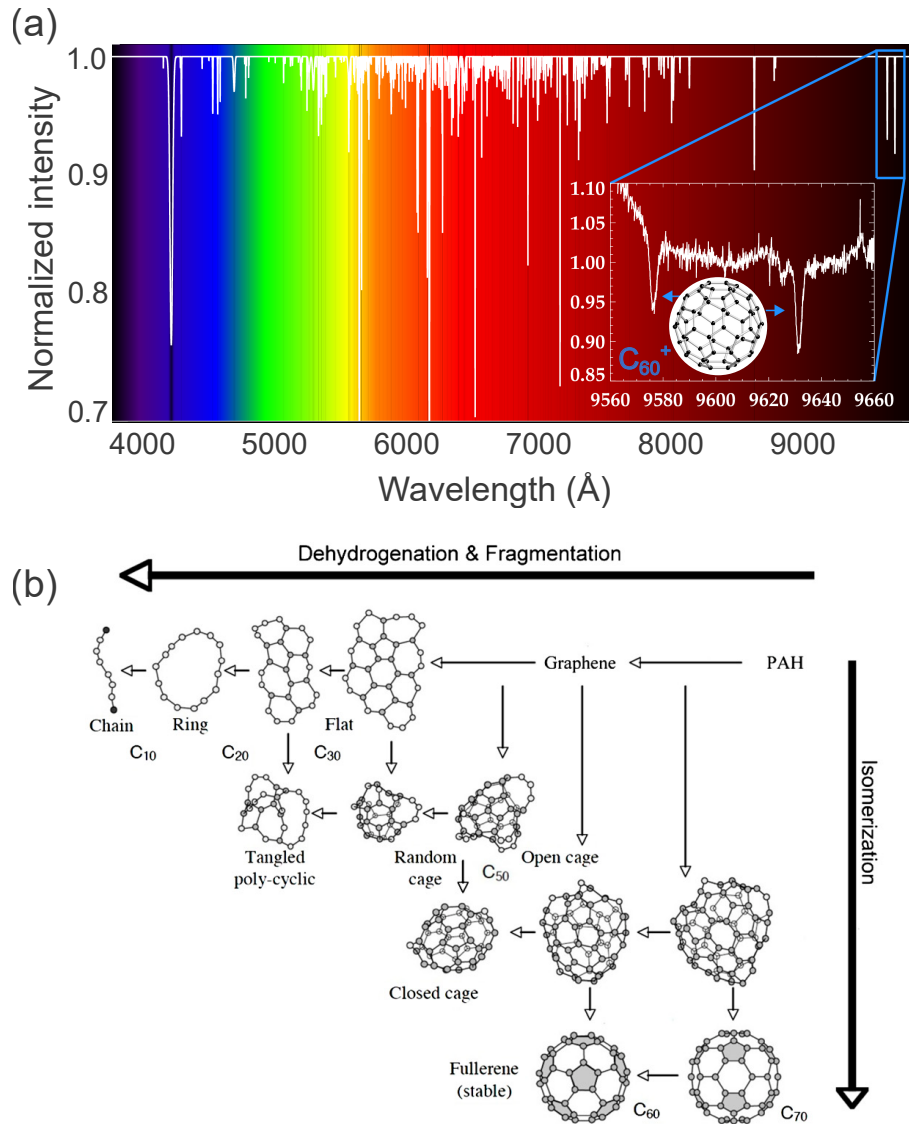
Figure 1.1: (a) The absorption features observed in diffuse interstellar bands (DIB). Two features of these DIB bands are assigned to the cationic C_{60}^+ fullerene species. (b) A top-down mechanism for the formation of fullerenes in the interstellar medium (see Ref. [21]). The stepwise dehydrogenation and fragmentation of a large PAH can lead to the curving and folding of the carbon backbone, which can lead to the formation of fullerene. Figure adapted from Refs. [21, 26].

As the information on the formation mechanisms and pathways is important, the elaborated dynamical studies of these systems are as crucial. In the literature, it is

3

illustrated that once these PAHs interact with intense radiation, they are subjected to get ionized and excited to their vibronic states. The relaxation of these highly excited vibronic states of the PAHs and their cations can happen non-adiabatically [27, 28]. The non-adiabatic relaxation to lower-lying excited states is reported to happen in a few femtoseconds to a few picosecond timescales, thus the investigation enters the regime of femtochemistry [27–29].

The research field of investigating the chemical processes happening at femtosecond timescales is referred to as femtochemistry for which Prof. Ahmed H. Zewail received the Nobel prize in chemistry in 2001 [30]. This field evolved from investigating a few atom systems [31] to systems as big as proteins and DNA [32]. Methods (theoretical and experimental) are developed to reveal the intermediate and transition states of the reactions from the reactant to the products and to probe the fragmentation timescales. In this work, the interaction of PAHs with intense extreme ultraviolet (XUV) and infrared (IR) radiation is investigated. The resulting fragmentation and relaxation dynamics are revealed using time-resolved femtosecond pump-probe spectroscopy. In this thesis, the interaction of the PAH fluorene with XUV photons with a photon energy of 40.9 eV is addressed. In addition to this, the stability of fluorene when interacting with intense near-infrared radiation has also been explored.

1.2 Spectroscopic methods

Spectroscopy investigates the interaction of matter with electromagnetic radiation and unmasks the properties of either of the two. The low density of the interstellar medium [1] makes the investigation of unimolecular reactions important, where gas-phase spectroscopy can be used.

The electronic structure of gas-phase PAHs can be investigated through various techniques that are described in Ref. [33] and the references therein. Briefly, laser induced fluorescence (LIF) is one of these techniques that involves recording the emitted fluorescent photons to investigate the ground and excited electronic states when the gas phase molecules interact with the photons generated from a tunable laser. Time-resolved fluorescence spectroscopy can provide information on non-radiative processes. Instead of measuring photon emission, the formed ions and electrons can be recorded by employing resonant two-color two-photon ionization (R2C2PI). The absorption of the first photon by the molecule is tracked with the help of the second photon that ejects the electron present in the excited state of the molecule resulting in ionization. R2C2PI provides additional information on the mass of species that are formed.

For PAH cations, non-radiative and thus non-fluorescent features dominate, and resonant multiphoton dissociation (RMPD) is useful. In the RMPD technique, the

formation of ions upon photon absorption can be recorded. Another tool to investigate ions is cavity ringdown spectroscopy (CRDS), where the decay of the ringdown time serves as the absorption feature. The CRDS technique can be coupled with the discharge of neutral PAHs, and the electronic spectrum of gas-phase PAH ions can be obtained.

In this thesis, photon absorption is recorded to investigate the electronic structure of gas-phase PAH cations. The range of the photon energy used to measure the absorption spectrum is different from those used in the above-mentioned spectroscopic techniques. We used X-ray photons to excite electrons in the core shell of cationic phenanthrene and obtained the NEXAFS spectrum at the carbon K-edge. These mentioned techniques are complementary to each other and probe different regions of the electronic structure. Probing core electrons (which carry element-specific information) can provide information on major structural changes, for example, carbon backbone rearrangement, when compared to different mass/charge ratio derivatives of cationic phenanthrene.
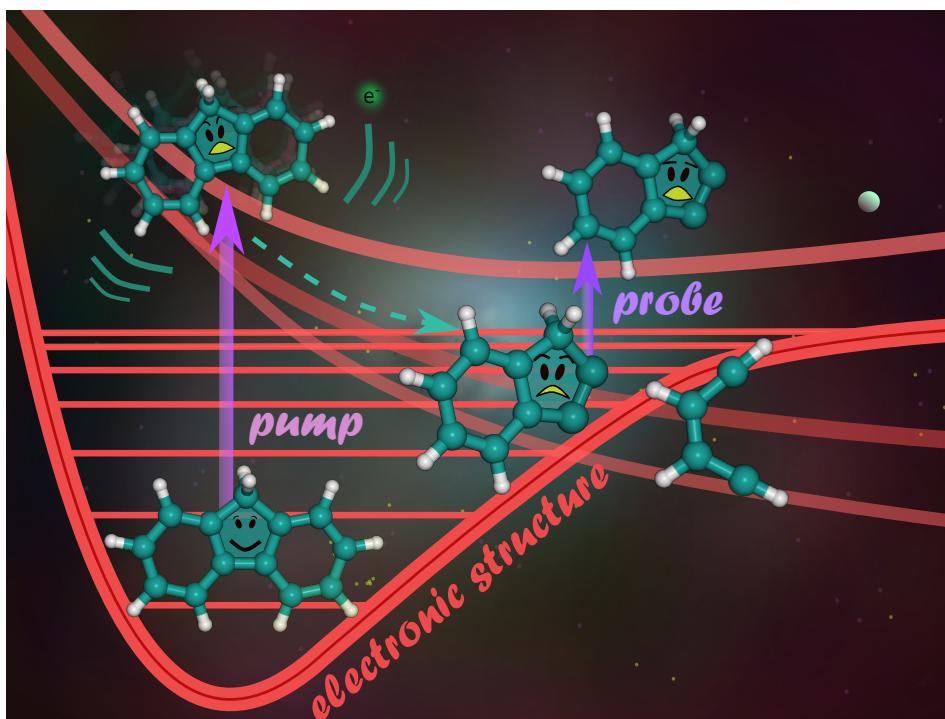
Figure 1.2: A graphical entry summarizing the investigated processes *via* time-resolved pump-probe spectroscopy and Near Edge X-ray Absorption Fine Structure (NEXAFS) spectroscopy.

Apart from recording the electronic spectrum by scanning the photon energy,

we also recorded the photoelectrons and the photoions at a fixed wavelength in order to investigate the relaxation and fragmentation of the neutral and cationic species of the PAH fluorene. To unravel ultrafast relaxation and fragmentation dynamics, femtosecond time-resolved pump-probe spectroscopy is widely employed. The simultaneous detection of the photoelectrons and the photoions also made it possible to extract information about the molecules' preferred fragmentation pathways under the respective experimental and radiative conditions. Figure 1.2 summarizes the processes that are investigated during the course of the thesis.

1.3   PETRA III and FLASH user facility

The large-scale user facilities at the Deutsches Elektronen-Synchrotron (DESY) research institute in Hamburg, Germany are exploited during the experiments that are discussed in this thesis. The NEXAFS spectroscopy, in this work, is performed using the third-generation synchrotron radiation facility PETRA III and the time-resolved pump-probe spectroscopy is done employing the XUV radiation obtained from the FLASH. The working principles of the two techniques and their application in the current work are addressed.

PETRA III can provide photon energies between 150 eV to 200 keV. This energy range is well suited to perform the NEXAFS spectroscopy at carbon K-edge, for which a photon energy range of 270 eV to 310 eV is needed along with tunable X-ray wavelength. The working principle that allows the PETRA III facility to provide tunable X-ray photon energy with high photon flux is described in detail in reference [34]. In brief, to generate the intense X-ray beam, the electron bunches at an energy of 6 GeV are kept in a 2.3 km long storage ring. The PETRA III storage ring is depicted in Figure 1.3. Max Von Laue is one of the three experimental halls at PETRA III, which are encircled. There are multiple beamlines in this Max Von Laue experimental hall illustrated in Figure 1.3. All beamlines in the storage ring are comprised of segments, which function as wigglers, undulators, or bending magnets. Due to the transverse acceleration of the electron bunches in these segments, radiation is emitted. The P04 variable XUV beamline makes use of such a segment consisting of an undulator (see Figure 1.3), namely advanced planar polarized light emitter (APPLE), which provides photons of energy ranging from 220 eV to 3 keV. A monochromator, placed in the P04 beamline, is used to scan through the photon energy, which facilitates the high-resolution absorption spectroscopy at the carbon K-edge.

PETRA III storage ring

e⁻

`Max Von Laue'

Advance Planar Polarized Light Emmitter-2
(APPLE-2) undulator at P04

linearly horizontal
polarization

linear hor.	~220-3000 eV
circular	~240-3000 eV
linear ver.	~280-3000 eV
linear ±90°	~470-3000 eV
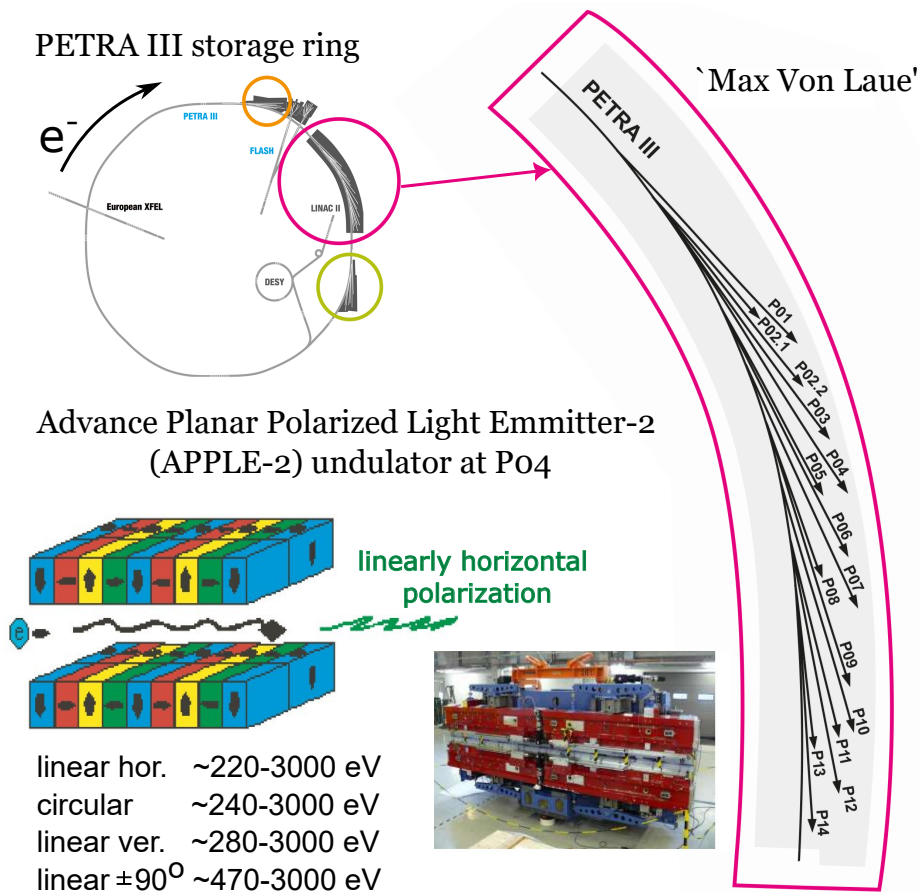
Figure 1.3: PETRA III storage ring comprising of three experimental halls that are encircled. Each experimental hall consists of several beamlines. Beamlines operating at the Max Von Laue hall are depicted. The P04 beamline uses the 4.9 meter long APPLE-2 undulator to emit radiation in the photon energy range of 220 to 3000 eV. The achievable photon energy range in different polarization settings using APPLE-2 undulator is given. Figure adapted from Ref. [35].

To perform pump-probe spectroscopy with femtosecond time resolution, ultrashort pulses are employed. In order to investigate the interaction of fluorene with XUV photons (40.9 eV) corresponding to the He II emission line, the ultrashort XUV pulses from the free-electron laser (FEL) at FLASH I are exploited. FLASH I makes use of fixed gap undulators as shown in Figure 1.4 where the electron bunches, generated from the radio frequency (RF) gun and accelerated by a superconducting linear accelerator, oscillate in phase with the alternating magnetic field of the undulators,

and coherent, monochromatic, and ultrashort radiation is produced. The possibility of using the ultrashort soft X-ray photon beam with over 10^{11} photons per pulse along with the ability to perform time-resolved pump-probe spectroscopy makes this facility an ideal choice for our experiments.
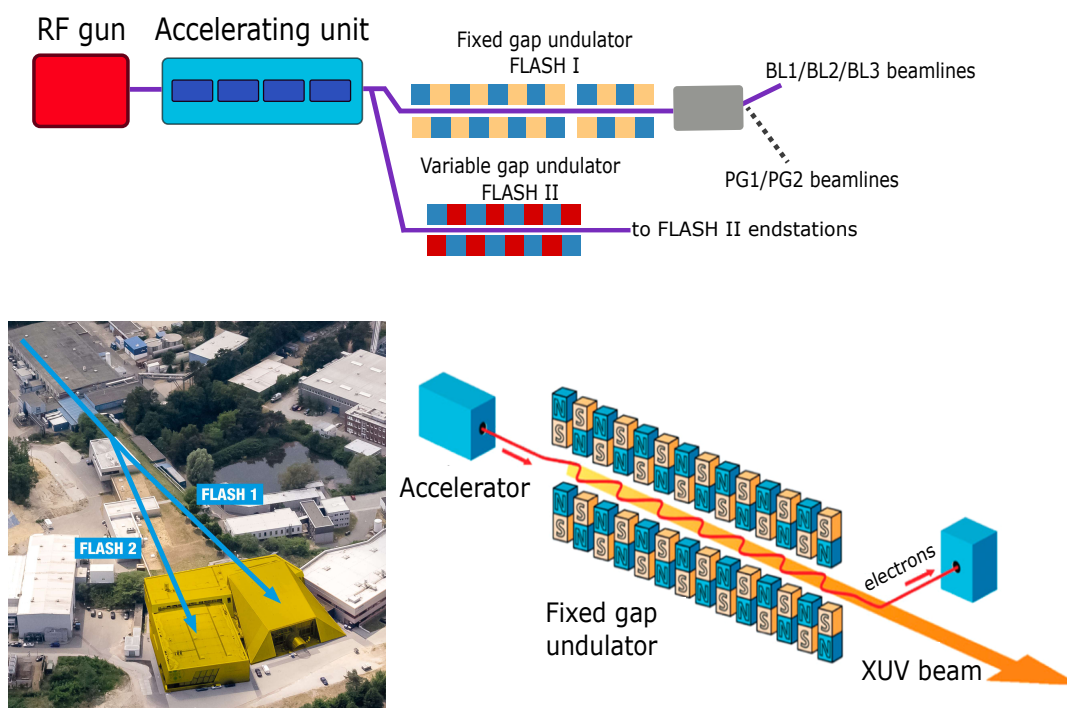
Figure 1.4: Schematic illustrating production of XUV beam at FLASH. The radio frequency (RF) gun is used first to inject the electrons into the superconducting accelerating unit, where the electrons are accelerated at relativistic speed. The output from the superconducting accelerating unit is guided to fixed-gap and variable-gap undulator. The FLASH I uses fixed-gap undulator to emit the coherent XUV beam as shown. Figure adapted from Refs. [35, 36].

1.4 Outline of the thesis

This thesis gives a detailed insight into the electronic structure and relaxation dynamics of the PAH molecules using two different spectroscopic techniques. Along with investigating the fragmentation and ionization processes, after the interaction of PAHs with the XUV radiation, the molecular dynamics beyond Born-Oppenheimer

condition are addressed. The outline of the thesis chapters is as follows.

The theoretical background of the used techniques is discussed in Chapter 2, which is subdivided into two sections. In the first Section 2.1, the core-electron spectroscopy is described briefly, and then the significance of NEXAFS is highlighted. After that, the theoretical calculations performed to interpret experimentally obtained NEXAFS spectrum are explained in detail incorporating the effect of the vibrational motions of the ions. In Section 2.2, the theoretical background of the femtosecond pump-probe spectroscopy and the enabling observational methods, namely, time-of-flight mass spectrometry (TOF-MS) and velocity-map imaging (VMI), are described.

The experimental techniques are described in Chapter 3, which is also divided into two sections. In Section 3.1, the experimental technique to obtain the NEXAFS spectra with a thorough explanation of the ion and photon beam is described in detail. In Section 3.2, the generation of the individual elements of the experiments such as the femtosecond XUV, IR, and Vis photon beams are explained. The preparation of the molecular beam as well as the method to perform the pump-probe spectroscopy are also mentioned in this section.

The data analysis routine is described in Chapter 4. In Section 4.1, the details of fitting the experimentally obtained NEXAFS spectra with the Voigt profile are provided. In Section 4.2, an elaborate explanation of the in-house built analysis scripts used for the FLASH analysis is given with the aid of appropriate schematics.

The results are presented in two separate chapters. Chapter 5 provides insight into the electronic structure of phenanthrene monocation and its dehydrogenated state. Chapter 6 highlights the fragmentation and the relaxation dynamics of fluroene investigated using pump-probe spectroscopy when pumped with the XUV radiation corresponding to the He II emission line (see Section 6.2) and when pumped with intense infrared (IR) radiation (see Section 6.3).

Chapter 2

Theoretical background

2.1 Investigating the electronic structure of PAH cations

The electronic structures of molecules and molecular ions provide insights into their chemical reactivity and reflect their geometric structure. We address the electronic structure of monocationic phenanthrene and its dehydrogenated state. A general schematic of the approximated molecular orbital (MO) structure of ionized or charged molecule with the energy levels is shown in Figure 2.1. Typically, there are core MOs, occupied MOs, unoccupied molecular orbitals (UMOs), and the continuum region. Theoretically, the electrons in the core orbitals can be described by atomic orbitals unlike the electrons present in the valence orbitals. While the core electrons deliver important element-specific information, the valence electrons participate in bond formation, and the MOs are delocalized over more than one atom. Therefore, core electron spectroscopy can be employed to examine the element-specific information and also to reveal the complete electronic structure of the molecules and molecular ions.

2.1.1 Core electron spectroscopy

Usually, core electron spectroscopy involves X-ray photons to excite or ionize the core electrons leaving behind a hole in the core orbitals and thus producing a core excited state. Apart from X-ray flashlamps, synchrotron radiation emitting X-ray photons is generally used for spectroscopic purposes. Usage of synchrotron radiation for spectroscopy can be attributed to its high intensity, coherent property at a specific X-ray beam wavelength, and ability to continuously tune this wavelength.

There are several possible processes that can happen upon the interaction of the molecules with these X-ray photons that are described in the following. Generally,

if the emission of the photons is measured, it is called X-ray emission spectroscopy (XES), whereas if the absorption of the photons is measured, then it is termed X-ray absorption spectroscopy (XAS). The ionization or excitation of the electron from the core orbital creates a core hole that decays over time. Depending upon the way in which this core hole decays, the XAS and XES methods can be classified further.
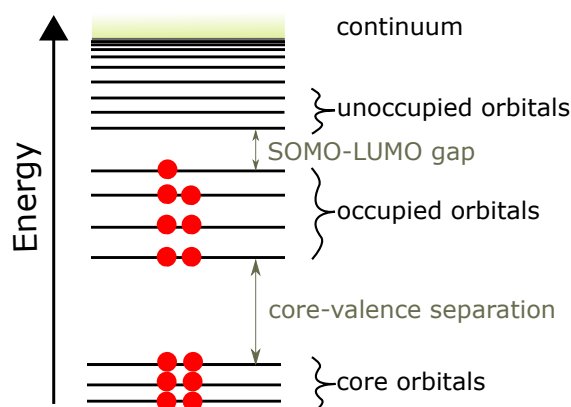
Figure 2.1: A schematic representation of a typical orbital structure for a polyatomic molecule depicting the energy gap between singly occupied molecular orbital (SOMO) and lowest unoccupied molecular orbital (LUMO).

The detection of a photoelectron, which is created as a result of direct ionization of the core electron by the incident X-ray photon is called X-ray photoelectron spectroscopy (XPS) as depicted in Figure 2.2. Emission of the photoelectron from the core orbital leaves behind a core hole, which can decay either radiatively or non-radiatively. The radiative process involves the transition of an electron from the valence MOs to the core MO, emitting a photon in the fluorescence or phosphorescence regime. This is known as XES. The photon instead of getting emitted can also ionize another electron from the valence MO. This process is called the Auger-Meitner decay process, also depicted in Figure 2.2.

In addition to ionizing the core electron (XPS), the absorption of the X-ray photon can excite the electron to the UMOs, also leaving behind a core hole. The direct measurement of this X-ray photon absorption probability is known as XAS (Figure 2.3). The core hole created after the X-ray absorption can decay either radiatively or non-radiatively. Radiative decay involves the transition of an electron from the valence MO to the core hole emitting a photon, and the process is called resonant X-ray emission spectroscopy (RXES). Since the electron is excited to further UMOs, the RXES provides the electronic structure of UMO in addition to the electronic structure occupied MO, which can also be extracted from XES (explained previously). This emitted photon can further eject the electron either from the UMO (participator

12

decay) or from the valence MO (spectator decay). The process is called resonant Auger-Meitner electron spectroscopy (RAES). We employed the XAS technique by exciting the electron from the deepest core orbital to the UMOs to explore the site-selective electronic structure of PAH cations. The technique is described in the next subsection.
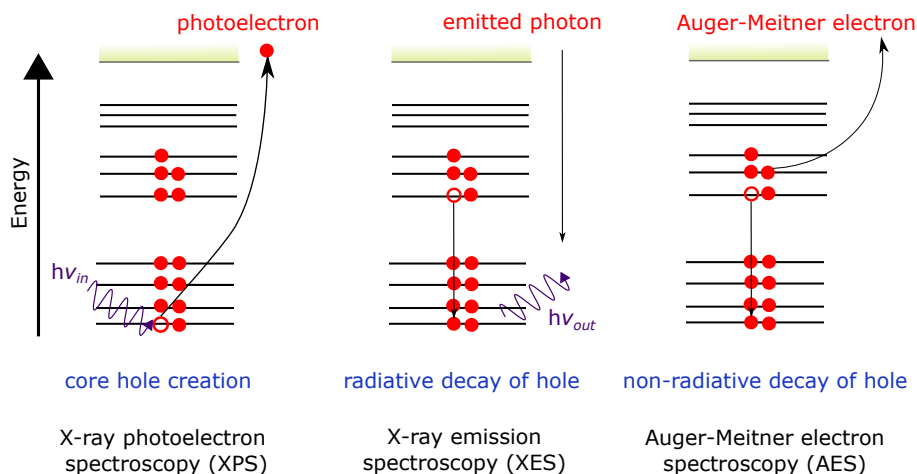
Figure 2.2: The schematic of core hole creation *via* emission of a photoelectron and its subsequent decay processes.
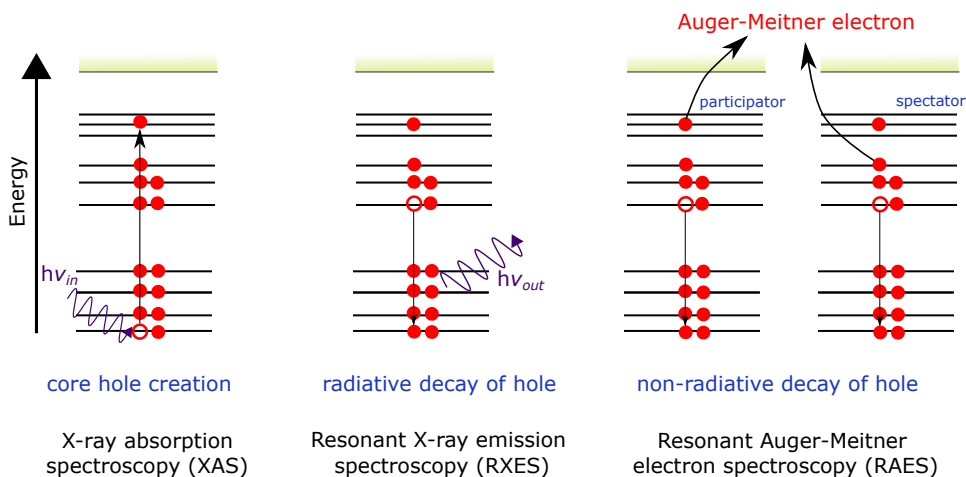
Figure 2.3: The schematic of core hole creation *via* excitation of a core electron and its subsequent resonant decay processes.

2.1.2 Near edge X-ray absorption fine structure spectroscopy (NEXAFS)

While performing the NEXAFS spectroscopy, the electrons from the core orbitals are excited to the bound UMOs or to the continuum. The incident photon energies can be scanned to obtain a NEXAFS spectrum. The observed spectral peaks represent the probability of transition of a core electron to UMO. When the photon energy is equivalent to the binding energy of a core electron, an abrupt increase in the transition probability is observed in the spectrum, and this is known as the absorption edge. In the case where the core electron is described by the principal quantum number $n = 1$, the absorption edge is denoted as K-edge absorption. Likewise, for $n = 2$, 3, etc. the absorption edge is known as L-, M-, etc. edges respectively. These spectroscopic notations are given in Ref. [37]. The core binding energy of the electrons is different for different atoms and molecules, e.g., the core binding energy of the bare carbon atom is 283.8±0.4 eV, while for oxygen it is reported as 532.0±0.4 eV [38]. Since the transitions from the core orbitals to UMOs are involved, the NEXAFS spectroscopy can provide element-specific information.

The curve in Figure 2.4 depicts three regions that can be investigated by tuning the photon energy that is produced by the synchrotron radiation. Region I and region III are far from the near-edge regime and are out of the scope of this thesis. Region II in Figure 2.4 depicts the regime near the absorption edge, and the transitions from the core shell to the unoccupied levels are probed. Usually, the photon energy range to achieve these transitions is around 10 eV below and 20 eV above the absorption edge. In addition to providing the site-selective chemical environment information, the NEXAFS technique [39] [40] is also beneficial in probing the final state of the transition, and hence the UMOs structure can be investigated as well. Therefore, it can differentiate between different arrangements of atoms in molecules, for example, between fully saturated or aromatic molecules, unlike the XPS technique, which is solely based on the electron binding energy in the initial state. We used the NEXAFS technique in our work to explore the UMOs of PAHs in different charge and dehydrogenation states (see Section 3.1) that were not investigated yet. Our experiments are supported with theoretically calculated XAS spectra explained in detail in the next section.

2.1.3 Calculations of NEXAFS spectra

Quantum-chemical calculations are performed to obtain the X-ray absorption spectrum using the ORCA 4 program package [41]. Since X-ray absorption involves the calculation of the excited state electronic structure, the time-dependent density functional theory (TD-DFT) is employed [42–44] along with the core-valence separation approximation. The near-edge X-ray absorption spectrum is obtained by fixing the
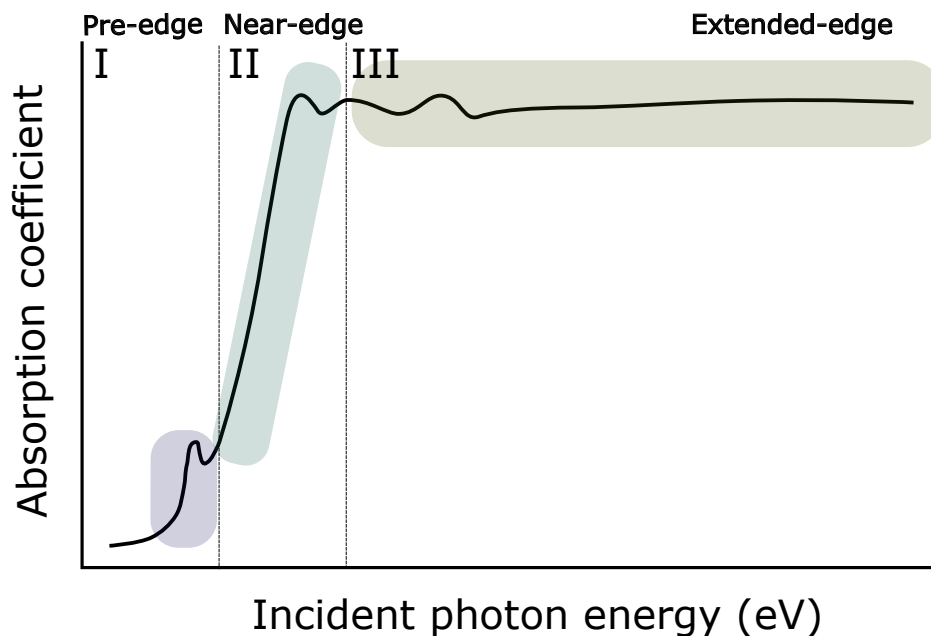
Figure 2.4: A typical curve depicting the absorption coefficient *vs.* incident photon energy (eV). Different details of the electronic structure of molecules/molecular ions can be probed in different regions (I/II/III).

initial and final orbitals to the carbon K-edge core orbitals ($1s$ orbitals) and the UMOs, respectively.

The process followed to perform the theoretical calculations to obtain the X-ray absorption spectrum is summarized in the schematic in Figure 2.5. Two molecular ion systems, namely the phenanthrene monocation ($C_{14}H_{10}^+$) and its dehydrogenated state ($C_{14}H_9^+$), are studied. For each system, the absorption intensity in the final spectrum is calculated using the expression in Figure 2.5. The expression represents a Maxwell-Boltzmann average that is performed over the contributions from individual isomers of the molecular system. Only the isomers having relative ground state energies (where the structure with the minimum energy is the reference) below 10,000 K are considered for the calculations. 10,000 K is a chosen high threshold value, which is estimated to take into account the isomers produced *via* ECRIS. These ground state energies are calculated using the B3LYP/def2-TZVPP method for both systems.

For $C_{14}H_{10}^+$, the geometry optimization was performed for both the doublet
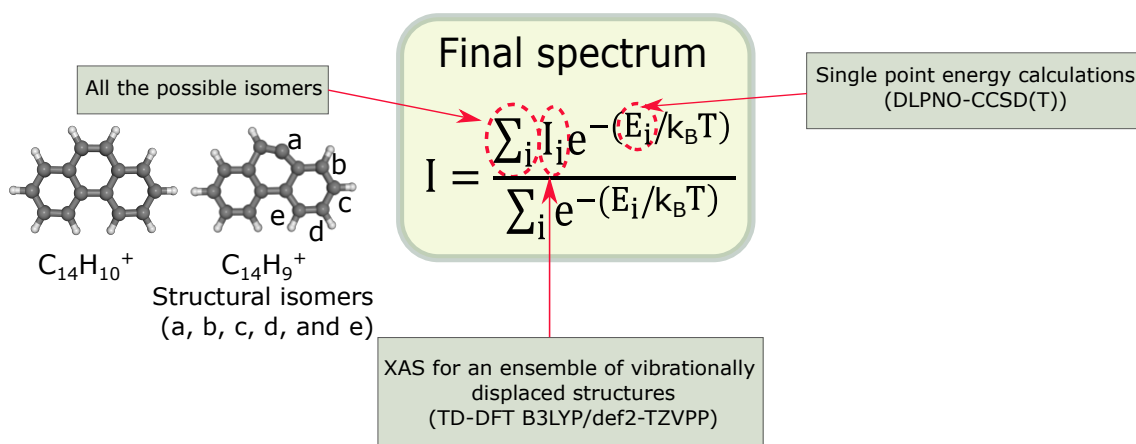
Figure 2.5: The schematic of theoretical vibrational averaging calculations. Five unique structural isomers of dehydrogenated phenanthrene monocation ($C_{14}H_9^+$) are investigated, which are named a, b, c, d, and e, depending upon the position of hydrogen loss.

$^2C_{14}H_{10}^+$ and quadruplet spin multiplicities $^4C_{14}H_{10}^+$. The ground state energies for the two states are given in Table 2.1. The given energy values are relative to the energy value obtained for the doublet state geometry. Further analysis is performed only for the doublet spin state as the optimized geometry for the quadruplet spin state possesses an energy value higher than 10,000 K.

Ions	Relative energy	
	(eV)	(K)
$^2C_{14}H_{10}^+$	0.0	0.0
$^4C_{14}H_{10}^+$	3.1	35,834

Table 2.1: Optimized energy of the parent monocation using B3LYP/def2-TZVPP considering both the doublet $^2C_{14}H_{10}^+$ and the quadruplet state $^4C_{14}H_{10}^+$.

For $C_{14}H_9^+$, since the dehydrogenation of phenanthrene can happen from five unique positions depicted by letters 'a' to 'e' in Figure 2.5, we have five isomers for which the geometry is optimized considering both the singlet and the triplet electronic states. The energy values are plotted for all these ten structures in Figure

16

2.6. Since all the energy values are below 10,000 K, these five isomers in singlet and triplet spin multiplicities are considered to obtain the final spectrum.
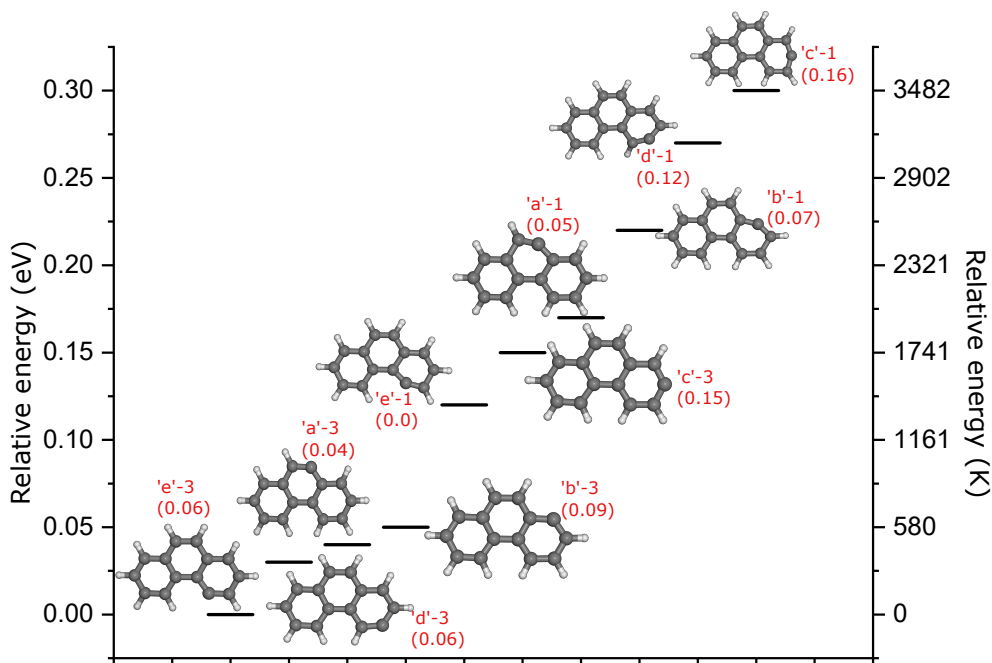
Figure 2.6: Optimized geometries for five structural isomers (denoted with letters 'a' to 'e') of $C_{14}H_9^+$, considering both the singlet ('1') and the triplet electronic state ('3'), using the B3LYP/def2-TZVPP method. The optimized structures are plotted against their relative energy values given in both eV and K units. Single point relative energies are calculated using the DLPNO-CCSD(T)/def2-TZVPP method and are given in parentheses in eV. All the relative energies are the energies relative to the structure with the minimum ground-state energy.

For each structure that is selected, the X-ray absorption intensity (I_i) is calculated, where i depicts the index of the selected structure, for example, for $C_{14}H_9^+$, i iterates from one to ten (five isomers in each singlet and triplet states). I_i includes the contribution of the electric dipole, magnetic dipole, and quadrupole transition probabilities. The I_i is obtained considering the fact that during the experiments, the ions are in their vibrationally ground and excited states. To obtain the contribution from vibrationally excited modes, the NEXAFS spectrum is calculated using the TD-DFT B3LYP/def2-TZVPP method for a set of displaced structures representing a thermal ensemble. The combination of these calculated spectra provides us with the intensity (I_i). Other density functionals in addition to B3LYP were also explored

17

for these calculations, and the results are summarized in Section 8.1.1 of the Appendix. The final spectrum is calculated by averaging the spectra of the different structures following the Maxwell-Boltzmann distribution as written in the equation in Figure 2.5. While averaging, single-point relative energies calculated using the DLPNO-CCSD(T)/def2-TZVPP method are used. For the $C_{14}H_9^+$ structures, these values are added in parentheses in eV units in Figure 2.6.

2.2 Fragmentation dynamics of PAHs on femtosecond time scales

2.2.1 Ultrafast time-resolved pump-probe spectroscopy

Chemical processes like bond breaking and bond formation are known to happen on femtosecond timescales, and the need for ultrashort pulses in combination with pump-probe studies is indispensable to investigate ultrafast processes [30]. In typical pump-probe spectroscopy, the molecules are pumped with energy resulting in excitation, dissociation, and/or ionization of the molecules depending upon the energy provided by the pump pulse. The dynamics initiated by the pump pulse can be revealed with the help of another pulse referred to as the probe pulse. The arrival time of the probe pulse relative to the pump pulse can be varied, and the relaxation of the excited molecular system (excited by the pump pulse) can be observed as a function of increasing delay time. The order of magnitude (in time) of the pulse duration of the two pulses and the delay time plays a significant role while investigating time-resolved molecular dynamics. Clearly, the pulse durations of the two interrogating pulses (pump and the probe pulse) should be comparable to the interconversion timescales of the system of interest. Moreover, the delay time between the two pulses should also be in the range of a few femtosecond to hundreds of femtoseconds to achieve a decent time resolution.

The fragmentation and relaxation dynamics of astrochemically relevant small-sized PAH fluorene ($C_{13}H_{10}$) is explored as the objective of this work. The interaction of the harsh radiation present in the interstellar medium [45] with the PAHs excites them in their rovibronic states, and the consequent processes involved can be visualized *via* the schematic shown in Figure 2.7. After pumping the molecules to the rovibronic states of the next ionization level, the subsequent relaxation to lower-lying states occurs at different timescales. The radiative relaxation of electronic states happens typically on much slower timescales than the non-radiative processes [46], which is not the topic of interest in this work. We focus on the non-adiabatic relaxation processes involving intramolecular vibrational energy redistribution (IVR), intersystem crossing (ISC), internal conversion (IC), and dissociation happening on the ultrafast timescales

that are represented in Figure 2.7. IVR processes involve transitions amongst different vibrational levels possessing the same electronic and spin state.
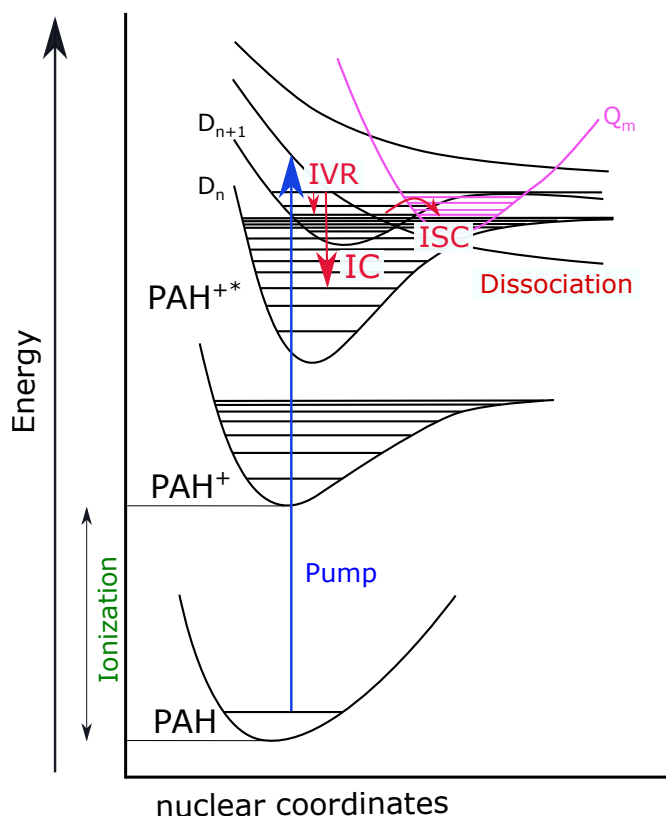
Figure 2.7: Depending upon the photon energy and the pulse intensity, the pump pulse can produce ionized PAHs in their rovibronic states denoted by 'PAH^{+*}'. The relaxation happens *via* non-adiabatic processes, i.e., intramolecular vibrational energy redistribution (IVR), intersystem crossing (ISC), internal conversion (IC), and non-adiabatic dissociative processes, that can be explored by an ultrafast probe pulse arriving at varied delay times. Here, n and m are the whole numbers varying from one to infinity. The notations 'D_n' and 'Q_m' denote the doublet and quadruplet spin state of the nth and mth electronic states, respectively. These spin states are chosen as examples.

The ISC occurs as a result of spin-orbit coupling of two different electronic spin states, whereas in IC processes, the spin is conserved, and therefore the transitions happen amongst different electronic systems of the same spin. Due to the large degrees of freedom of these molecules, the excited electronic states of the system can

be closely spaced, and the Born-Oppenheimer approximation breaks down [27–29, 47, 48]. To investigate these non-radiative processes, ultrafast pump-probe spectroscopy techniques are well suited and contribute to understanding these π-extended systems, along with computationally expensive and challenging theoretical work, see for example Refs. [49–52].

2.2.2 Observational methods to perform pump-probe spectroscopy

There exist various observational methods that are compatible with pump-probe spectroscopy, depending upon the interest of the experiment. Some examples of what can be observed are the absorption of the photons, emission of the electrons and photons, diffraction of the electron, time-of-flight (TOF) of the electrons and ions, velocity map images of the electrons and ions, etc. [28, 53, 54]. The observational methods that we used as tools to acquire time-resolved information are time-of-flight mass spectrometry (TOF-MS) and velocity-map imaging (VMI), which are recorded as the delay time between the pump and probe laser is varied. These methods are described in detail in the following sections.

2.2.2.1 Time-of-flight mass spectrometry (TOFMS)

The working principle of a typical TOF mass spectrometer was first proposed in 1946 by Stephens [55], stating that *"In traveling down the vacuum tube, ions of different M/e have different velocities and consequently separate into groups spread out in space"*. TOF can be typically defined as the time that an ion takes from the point of formation to the point of detection in a spectrometer. The TOF is dependent on the velocities of the ions. Thus the heavier ions with low velocity would be able to cover less distance in space than the lighter ions, and therefore are subjected to separating out in space. Two years after this principle was proposed, *i.e.*, in 1948, the technique was experimentally realized by Cameron and Eggers [56]. It was later in 1955 when the commercial experimental instrument by Wiley and McLaren gained importance [57]. In their work, they observed that the ions with the same mass over charge ratio (m/z) (mass, m, and charge, z) have a finite distribution in the arrival times, which was reported to be due to the fact that ions have spatial distribution and kinetic energy distribution at the time of formation. A TOF spectrometer was then devised to optimize for the space and the energy resolution.

The design of the simplest TOF mass spectrometer is described here to evaluate the dependence of the TOF on the m/z of ions, shown in Figure 2.8(a). Consider positive ions with charge 'z' and mass 'm' originated in the source region 'S' with initial velocity zero.
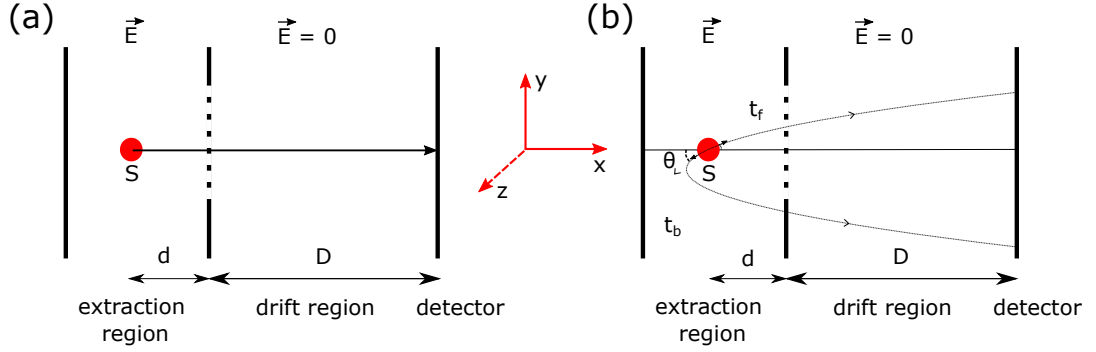
Figure 2.8: The schematic illustrates the ion originating from the source region 'S', extracted by the field $\overrightarrow{E}$, passed to the detector through the field free region. (a) The simple case of an ion originating along the time of flight axis (x-axis) is represented. (b) An example of two equal m/z ions with equal momentum in opposite directions produced as a result of dissociation in the same event. One of these two ions originates in the forward direction at an angle θ w.r.t the x-axis. The other one originates in the backward direction of the field. The TOF of the ions produced in the forward and the backward direction are labeled as 't_f' and 't_b', respectively.

The ions are then extracted towards the drift region by the electric field $\overrightarrow{E}$ in $+x$ direction. Finally, these ions are stopped at the detector after passing through the field-free (drift) region. The TOF is defined as the time taken by these ions from 'S' to the detector given by Equation 2.1,

$$\text{TOF} = t_\mathrm{d} + t_D \tag{2.1}$$

where t_d and t_D are the time taken in the extraction region of width 'd' and the drift region of width 'D', respectively. In the extraction region, the electrostatic force (zE) on the ion can be equated to the mass times the acceleration given by Equation 2.2,

$$zE = m\left(2\frac{\mathrm{d}}{t_\mathrm{d}^2}\right) \tag{2.2}$$

which after solving gives Equation 2.3.

$$t_\mathrm{d} = \sqrt{\frac{2m\mathrm{d}}{zE}} \tag{2.3}$$

The ions enter the drift region with velocity $v = zEt_\mathrm{d}/m$. The time taken in the

21

field-free region would be D/v and is given by Equation 2.4.

$$t_D = \frac{Dm}{zEt_d} \tag{2.4}$$

The final TOF is given by Equation 2.5, which shows that a fixed geometry of the spectrometer, TOF can be observed to be directly proportional to m/z.

$$\text{TOF} = \sqrt{\frac{m}{z}} \sqrt{\frac{1}{2E\text{d}}} (\text{D} + 2\text{d}) \tag{2.5}$$

A more realistic example is depicted in Figure 2.8(b), which shows the case of dissociation of a dication into two ions of equal masses $X_2^{2+} \rightarrow X^+ + X^+$. Due to the conservation of momentum, the initial pathway of these two ions will be opposite to each other after dissociation. Ion X_f^+ is the ion having the velocity component in the forward direction ($+x$) and will take less time to travel to the detector than the backward projected ion X_b^+. The TOF for X_b^+ and X_f^+ are denoted by t_b and t_f respectively. Due to different velocities at the time of formation in spite of a similar m/z, there will be a spread in the TOF observed in the spectrum, which can be given by $t_b - t_f$.

As mentioned before, the finite source region and the initial velocity distribution are the two main reasons for the finite spread in the TOF spectra. It is demonstrated in Ref. [57] that the spatial resolution can be improved by modifying the ratio of the voltages of the extractor and repeller plates, whereas the initial velocity spread can be improved by reducing the distance between the two voltage plates.

The essence of TOF-MS lies in its capability to distinguish between species with different m/z ratios. This is particularly useful to know what charged species are being formed in an experiment *via* measuring the TOF spectra. However, no structural information could be obtained. In the case of pump-probe experiments, the TOF spectrum can be acquired as a function of pump-probe delay time. We monitor time-resolved TOF in order to reveal the fragmentation and relaxation dynamics of PAHs in their different charged states.

2.2.2.2 Velocity-map imaging (VMI)

In the above-discussed TOF-MS method, the kinetic energy release (KER) information is carried in the temporal structure of the spectrum. A 2D imaging technique can be employed to obtain the KER and the angular distribution [58] of the initial velocity vectors of the ions [59]. This information is retrieved from the 2D spatial image. Hence, the resolution is limited by the quality of mapping the velocity-vector distribution on the detector [60]. The VMI technique, which was first reported by Eppink and Parker [60], demonstrated the exploitation of the 2D imaging technique

to its full potential. The resultant VMI conditions that were achieved in Ref. [60] cause the charged species traveling with the same initial velocity to be mapped on the same position on the detector irrespective of their finite source region. This VMI technique increased the resolution of the images to a great extent as compared to the conventional 2D imaging technique. The typical experimental setup to perform VMI is summarized here and discussed in detail in Ref. [60].

As shown in Figure 2.8, there are three electrodes to guide the charged particles, namely, the extractor, the repeller, and the ground plate. In the Wiley-McLaren setup, grid electrodes were used that were shown to work well in providing a highly resolvable time-of-flight mass spectrum. However, for imaging purposes, these grid electrodes cause blurring of the images as shown in the work by David Chandler [61]. The presence of the grids also caused reduced transmission of the signal. By replacing these grid electrons by open electrodes (electrodes with holes), drastically improved images could be obtained to perform VMI. The setup making use of these open electrodes is called an imaging lens setup. This imaging lens setup provides in principle 100% transmission of the signal. The use of open electrodes in the VMI conditions allowed focusing of the charged particles with the same velocity on the same position of the detector. The achievement of the superposition of the ions with the same velocity on the same position of the detector during the VMI conditions is called the "deblurring" effect.
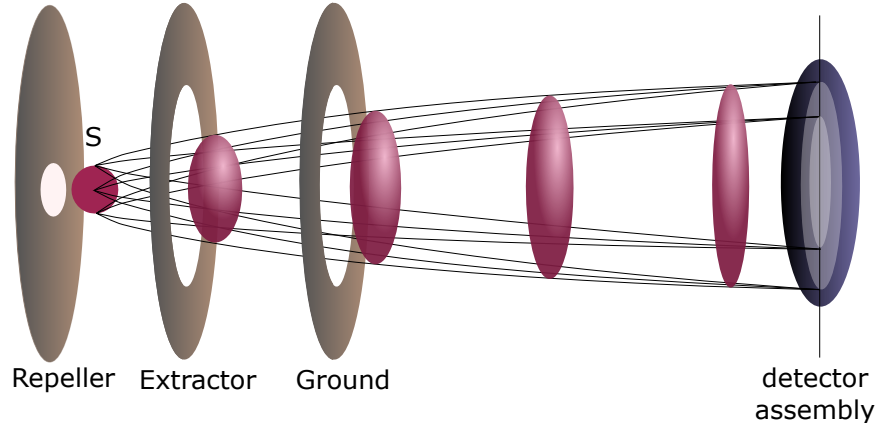
Figure 2.9: A typical VMI setup with imaging lens setup is shown. In the source region 'S', the so-called Newton spheres are produced, expanded, and guided further through the extractor and ground plate to the VMI detector assembly. The figure illustrates that the ions produced with the same velocity vector reach the detector at the same position irrespective of the initial formation position.

A schematic of VMI setup is shown in Figure 2.9 [62]. The ions are produced

23

in the finite source region and their 3D initial velocity vector distribution can be denoted by so-called "Newton spheres" [63], depicted by a red sphere. As the sphere passes through the extractor and the ground electrodes, the 2D projection of the 3D velocity vector distribution is obtained at the detector. When operated in the VMI conditions, it can be observed that the ions with the same initial velocity vector are focused on the same position of the detector. The radial and angular coordinates of this 2D image formed as a result of a squashed Newton sphere can be used to reconstruct the initial 3D velocity distribution. This reconstruction can be performed using mathematical tools like Abel inversion and Hankel transformation that assume the initial 3D velocity distribution to be cylindrically symmetric.

We employed TOF-MS in combination with the VMI to achieve resolution in both the velocity and the m/z domains, respectively. The resolution in the velocity and therefore the momentum domain enables us to differentiate between the dissociation processes happening in different momentum regions. In the case of pump-probe experiments, the velocity map images can be acquired as a function of pump-probe delay time. We monitor time-resolved and momentum-separated ion yields in order to investigate the dynamics of the fragmentation processes throughout the work.

Chapter 3

Experimental techniques

3.1 NEXAFS spectroscopy at PETRA III

The permanent end-station PIPE (Photon-Ion spectrometer at PETRA III) [64] is set up at the variable polarization XUV beamline P04 of the synchrotron PETRA III at DESY in Hamburg. This instrument is used to carry out experiments in the gas phase where both ions (either atomic or molecular) and ionic clusters can be investigated. The performance profile of the beamline P04 is tabulated in Table 3.1. The PIPE end-station offers two chambers, one realizing a merged-beam setup, where the ion beam and the photon beam are co-axial, and the other realizing a crossed-beam setup, where the two beams are perpendicular. The latter is used to perform cold target recoil ion momentum spectroscopy (COLTRIMS)[65, 66], which is not applied as part of this thesis, so it will not be discussed here any further. Instead, we used the merged-beam setup to perform NEXAFS spectroscopy involving the absorption of soft X-ray photons by the PAH cations of interest. Absorption causes the core-shell electrons to be excited/ionized at the carbon (C) K-edge.

Parameters	Values
Photon energy	250 - 3000 eV
Resolving power	$>10^4$ (up to $>3 \cdot 10^4$) @1 keV
Photon Flux	$>10^{12}$ photons/s up to $5 \cdot 10^{12}$ photons/s
Spot size of beam at sample	$10 \cdot 10 \ \mu m^2$ / $50 \cdot 50 \ \mu m^2$
Polarization (switching rate)	circular, linear hor./vert. (<0.1 Hz)

Table 3.1: Parameters for the beamline P04 performance [67]

The following three subsections outline the experimental details. In the first subsection, the preparation of the ion beam is described, followed by the details about the interaction region between the photon beam and the ion beam in the next subsection. Finally, the last subsection explains the process of measuring the relative absorption cross sections.

3.1.1 Molecular ion source at PIPE

In this subsection, first, the molecular sample preparation is described followed by the description of the electron cyclotron resonance ion source (ECRIS), which is used to produce the ion beams. After this, the composition of the ion beam produced from the ion source is shown.

3.1.1.1 Molecular sample

The molecule of interest, namely phenanthrene, can be bought commercially, and further sublimated to the gas phase. To bring the molecules into the gas phase, the powdered sample can be directly introduced into the ion source through a stainless steel crucible. This crucible is inserted into an oven, which can be resistively heated up to 180°C, producing vapor of the sample. Another method of heating the sample is *via* heating tape. However, using this method, a temperature higher than 200°C cannot be reached in the current setup. These vapors can then seep into the ion source. We purchased a phenanthrene sample (melting point 101°C) in powder form from Sigma-Aldrich with 98 % purity. The sample was heated to 120°C to bring the molecules into the gas phase. The vapors were passed into the ionization chamber through the gas inlet (shown in Figure 3.1).

We are interested in investigating cations, which can be created by several methods, electron impact ionization being one of them. The fundamental process of electron impact ionization to generate cations is illustrated by the following Equations 3.1 and 3.2:

$$\mathrm{PAH} + \mathrm{e}^- \rightarrow \mathrm{PAH}^+ + 2\mathrm{e}^- \tag{3.1}$$

Similarly, higher charge states can be achieved:

$$\mathrm{PAH}^{k+} + \mathrm{e}^- \rightarrow \mathrm{PAH}^{(k+1)+} + (k+2)\mathrm{e}^-; k > 1 \tag{3.2}$$
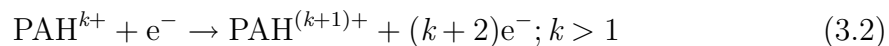
The ionization cross sections are known to decrease with increasing charge state 'k'. To knock out electrons from the molecules or atoms, the e^- kinetic energy should be greater than the valence shell ionization threshold. Electron heating in plasma can be used to achieve the required electron kinetic energy. To produce the ion beam, the high-velocity electrons from the plasma can be passed through the sample gas resulting in ionization and dissociation. This process of bombarding energetic electrons onto the vapor to produce cations is implemented in the ECRIS [68].
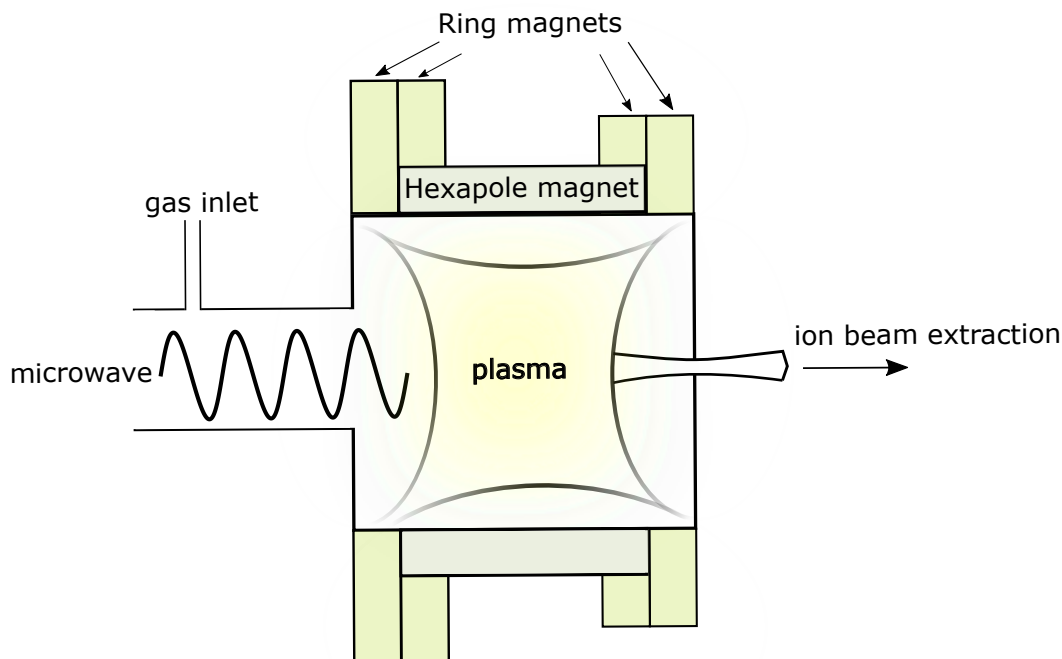
Figure 3.1: Schematic of the ECRIS, the molecules of interest seep into the ECRIS through the gas inlet. The microwave discharge creates a plasma confined by the ring and hexapole magnets. The plasma electrons gyrate and ionize the molecules to form an ion beam that is extracted in the extraction region.

3.1.1.2 Electron cyclotron resonance ion source (ECRIS)

The schematic illustrating the functioning of ECRIS is shown in Figure 3.1, and the working principle can be explained as follows. There are two main regions of the ECRIS, the first is the ion production region and the second one is the ion extraction region. The plasma is generated in the first region *via* microwave discharge of the background gas in a magnetic field and is further confined using a combination of two constant magnetic fields. The ring magnets provide axial plasma confinement that allows the forward and backward motion of the electrons. The hexapole magnet ensures the radial confinement of the plasma. The combination of these two magnetic fields gives rise to the spiral motion of electrons in the plasma, having a natural gyration frequency in the microwave region. When the external microwave frequency matches the natural gyration frequency of electrons, the electrons heat up. These electrons bombard the sample, and the electron impact ionization leads to the formation of ions that move in circular paths. These ions are finally extracted by puller electrodes.

To summarize, ECRIS works based on plasma confinement and electron heating with microwave radiation. Overall, there are two kinds of ion sources, one in which permanent magnets are used, and are called an all-permanent magnet ECRIS. The second kind allows the adjustment of this magnetic field for optimal performance. This second kind is employed when ions with high charge states are required. However, for these experiments, the achievement of high charge states was not desired, and therefore we employed the 10 GHz all-permanent ECRIS.

We used the ECRIS at a pressure of the order of a few 10^{-5} mbar and a microwave frequency of 9.66 GHz [69]. The ECRIS was operated at a power of 39.7 W. The ion beam is extracted with an extraction voltage (U_{acc}) of +6 kV. Finally, we obtained a continuous ion beam with a current of the order of a few nA.

3.1.1.3 Ion beam composition

The molecular ions are guided to the next stage with the help of a series of electrostatic lenses and deflectors where the ions can be m/z selected using a double-focusing analyzer dipole magnet (AM) with two four-jaw slits before and after the magnet. The magnetic field strength of the AM is scanned and the ion current is recorded by the Faraday cup. This magnetic field strength can be calibrated to the mass over charge ratio (m/z). The resultant m/z versus ion current plot can be used to determine the composition of the ion beam produced by the ECRIS.

The calibration equation to transform the magnetic field 'B' information into the m/z is described in the following. The charge of the ion in the beam is denoted by the product $z_{\text{ion}} \cdot$e, where z_{ion} is the charge state and e is the fundamental electronic charge. The extraction of the ion beam from the ECRIS at a potential of +6 kV provides kinetic energy to the ions of mass m_{ion} accelerated to the velocity v_{ion}, which can be calculated by equating the kinetic energy of the ions to the electric potential energy (Equations 3.3 and 3.4).

$$\frac{1}{2} m_{\text{ion}} v_{\text{ion}}^2 = z_{\text{ion}} e U_{\text{acc}} \tag{3.3}$$

$$v_{\text{ion}} = \sqrt{\frac{2 z_{\text{ion}} e U_{\text{acc}}}{m_{\text{ion}}}} \tag{3.4}$$

After extraction, the ion beam passes through the dipole magnet with a bending angle of 90°. The Lorentzian force acting on the ions due to the magnetic field is balanced by the centripetal force.

$$\frac{m_{\text{ion}} v_{\text{ion}}^2}{r} = z_{\text{ion}} e v_{\text{ion}} B \tag{3.5}$$

where 'r' is the curvature of the motion and is equal to the bending radius (one meter) of the magnet with the magnetic field 'B'.

After further rearrangement of equation (3.5), the relation between the magnetic field and the m/z can be determined (Equation 3.6).

$$B = \sqrt{\frac{m_{\mathrm{ion}}}{z_{\mathrm{ion}}}} \sqrt{\frac{2eU_{\mathrm{acc}}}{r^2}} \tag{3.6}$$
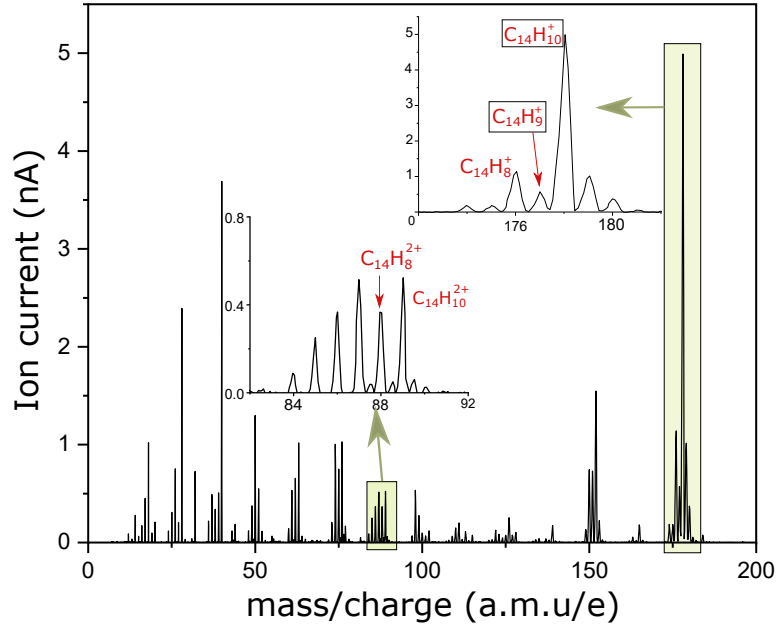
Figure 3.2: Mass spectrum showing the primary ions formed *via* the ECRIS. The green shaded region on the right of the mass spectrum shows the dehydrogenated ($C_{14}H_9^+$ and $C_{14}H_8^+$) and parent ($C_{14}H_{10}^+$) monocations, and the left green shaded and zoomed-in view depicts the dehydrogenated ($C_{14}H_8^{2+}$) and parent ($C_{14}H_{10}^{2+}$) dications. For the sake of clarity, only the ions that were investigated are illustrated in the zoom-in sections.

The calibrated mass spectrum is shown in Figure 3.2. It is evident from the mass spectrum that the electron bombardment in the ECRIS could not only ionize the phenanthrene molecules but also dissociate its' carbon backbone. The magnetic field of the AM can be kept constant in order to select a specific m/z of the ions amongst all the observed ions in the mass spectrum. This pre-photon-interaction ion beam is referred to as the primary ion beam throughout the text. We are interested in studying the effect of different degrees of dehydrogenation and ionization on the electronic structure and thus we chose different specific primary ions to perform the experiments. The selected primary ions are highlighted in Figure 3.2. The respective

selected primary ion beams are guided further to the merged-beam (MB) interaction region to carry out NEXAFS spectroscopy.

3.1.2   Interaction of the ion beam with the photon beam

In this subsection, the experimental procedure is highlighted. The experimental setup of the PIPE end-station is depicted in Figure 3.3. The green-shaded region indicates the molecular ions formed in the ECRIS. The analyzer dipole magnet (AM) located after the ECRIS m/z selects the ion of interest, which is illustrated by the yellow-shaded region (as explained in the previous section). The primary ion current is recorded using the Faraday cup (FC), which is placed on the way to the merged-beam (MB) interaction region. The primary ion beam is then collimated to the MB interaction region (red-shaded region) with the help of slits. In the 1.7 meters long interaction region between the ions and photon beams, the photon beam enters coaxially from the right shown by the magenta arrow. During the experiments described here, the photon energy was kept in the range of 280 eV to 310 eV to perform core-shell ionization and excitation of the selected primary ion carbon atoms. The merged-beam technique was employed since it offers a large interaction region for the photons and ions to interact ($\sim$ 1.7 m) [70]. This is advantageous for ionic targets specifically because of their lower target densities ($10^6/cm^3$ [70]) that make it challenging to study them with other techniques as compared to neutral gas species that have enough density to be studied with for example the crossed-beam interaction technique.

Post interaction, the absolute photon flux is measured with the photodiode (PD) at the extreme left of the experimental setup as illustrated in Figure 3.3. The product ion beam is deflected from the photon axis using the demerger magnet (DM). The DM also separates the primary ion beam from the ions produced as a result of photoionization (photoions). The primary ion current is recorded by the Faraday cup in the vacuum chamber of the DM. The photoions are stopped at the single particle detector (SPD). The demerger magnetic field is scanned to determine the composition of the product ion beam recorded at the SPD.

In order to distinguish between the product ions formed as a result of photon absorption and as a result of collisions with the residual gases, the signal at the SPD was recorded with and without the photon beam as shown in Figure 3.4. To make the distinction between the photon signals with and without photons more prominent, the monochromator, placed at the P04 beamline to scan the photon energy entering from PETRA III, was operated in the zeroth order. Therefore, instead of a monochromatic photon beam, we use a polychromatic photon beam with a much higher (more than 10 times than a monochromatic beam) photon flux (the so-called pink beam).
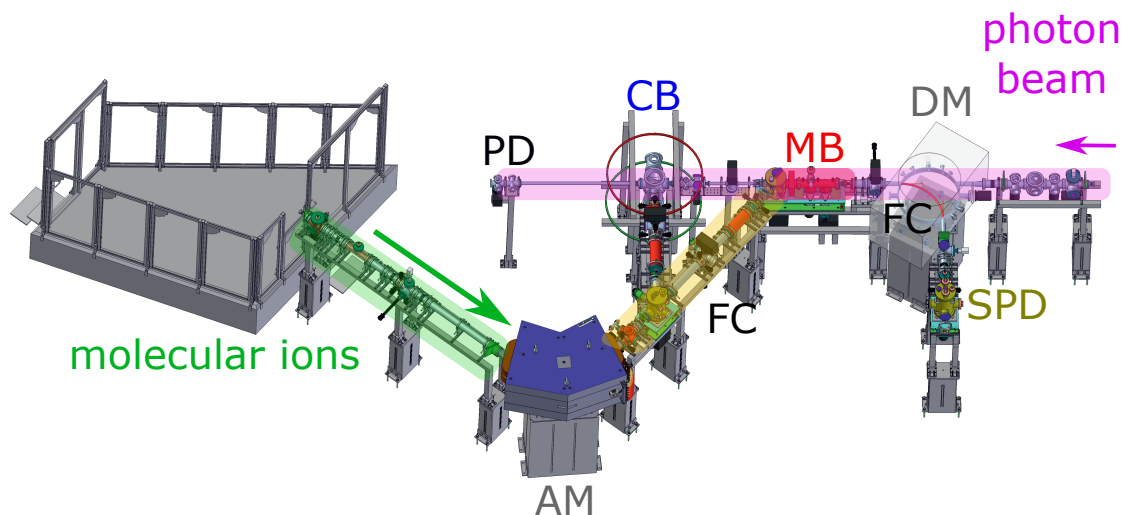
Figure 3.3: The photon-ion spectrometer at PETRA III is shown. The shaded regions illustrate the respective beams present at these positions. The green arrow depicts the molecular ions formed by the electron cyclotron resonance ion source (ECRIS) (not shown here) that enter the analyzer dipole magnet (AM). The yellow-shaded region depicts the presence of the primary ion beam consisting of only a single m/z selected ion. This primary ion beam can be either guided to the crossed-beam (CB) interaction region or the merged-beam (MB) interaction region where it interacts with the photon beam (in the magenta region) entering from the opposite direction. After the interaction, the photon flux is measured at the photodiode (PD) at the extreme left of the setup, and the product ions are deflected off the photon beam axis *via* the demerger magnet (DM) that also separates the primary ion beam from the product ions. The primary ions still present after the interaction with the photons are stopped at the Faraday cup (FC) in the DM vacuum chamber and the product ions are guided to the single particle detector (SPD). Figure is adapted from Ref. [70]

The photon energy was kept centered above the carbon K-edge at 295 eV. Figure 3.4 shows the mass spectrum of the product photoions formed after the absorption of photons by the primary parent monocations $C_{14}H_{10}^+$ in red and the product ions

formed without any photons in black. The increased signal at the m/z ratios 58.6, 59.3, and 89 shows the production of $C_{14}H_8^{3+}$, $C_{14}H_{10}^{3+}$, and $C_{14}H_{10}^{2+}$, respectively, as the photon absorption effect. These product ions formed after the photon absorption by the phenanthrene monocations were m/z selected individually to measure the relative cross sections of the photon absorption process. Finally, the NEXAFS spectrum is obtained by scanning the photon energy to obtain the relative absorption cross sections.
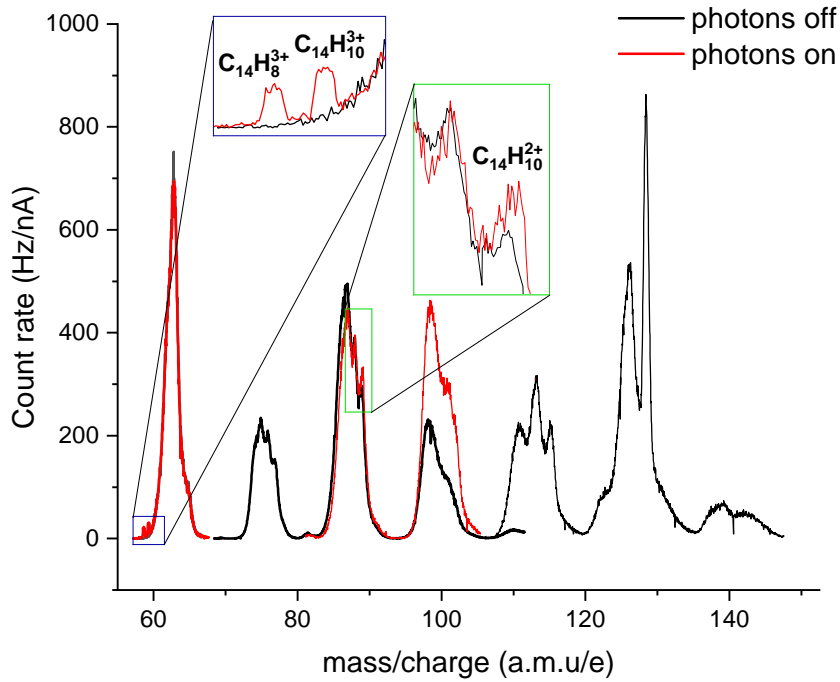
Figure 3.4: The product ions formed in the merged-beam interaction region are shown when the phenanthrene monocation $C_{14}H_{10}^+$ was m/z selected as the primary ion. The zoom-in depicts clear changes in the mass spectrum as a result of photon absorption by $C_{14}H_{10}^+$. the highlighted product ions were selected individually to carry out relative cross section measurements.

3.1.3 Measured photon absorption cross section

This subsection provides details about the absorption cross sections that are measured during the experiments, followed by further correction and calibration applied to the measured values.

The PIPE setup enables to measure absolute absorption cross sections σ by normalizing the product ion count rate R on the absolute photon flux ϕ_{ph}, the number density of primary ions in the interaction region determined from their ion

current I_{ion}, velocity v_{ion}, and charge $q_{ion} \cdot$e, the primary ion and the photon beam overlap factor F_L, and the detection efficiency η.

$$\sigma = R\frac{q_{ion}\mathrm{e}v_{ion}}{\eta I_{ion}\phi_{ph}F_L} \tag{3.7}$$

The beam overlap factor F_L was not measured for this study due to time constraints during the granted beamtime, but the qualitative overlap of the photon beam and the ion beam was ensured, and hence relative absorption cross sections could be measured.

The measured relative cross sections were corrected for the background signal by subtracting the residual gas signal, which was measured in the photons off condition. To ensure accurate monochromator calibration, known photo ionization resonant values were used for carbon monoxide (CO) gas at 287 eV [71]. This calibration results in an 81±2 meV shift in the measured photon energy. The photon energy values were also corrected for the Doppler shift that is experienced by the ions moving with speed v_{ion}. The following equation thus gives the photon energy in the rest frame of the moving primary ions.

$$h\nu = h\nu_c\sqrt{\frac{1+\beta}{1-\beta}} \tag{3.8}$$

where hν is the calibrated photon energy, and β is the velocity of the primary ions with respect to the speed of light 'c'.

For the present experiments, the NEXAFS spectrum is measured around the carbon K-edge and thus the cross sections were measured for the photon energy range from 280 eV to 310 eV with a 0.01 eV step size. The photon uncertainty was oberved to be in the range of 50 to 200 meV. The relative cross sections were measured for ten different pathways, amongst them, five are discussed here and others are discussed in Ref. [72].

3.2   Time-resolved pump-probe spectroscopy

Elementary molecular processes including chemical bond breaking or making are known to happen on femtosecond timescales. Ultrashort pulses are an exceptional tool for investigating these ultrafast molecular processes. We employed the Free-electron LASer in Hamburg (FLASH) [73] to explore the femtochemistry of PAHs using a time-resolved pump-probe spectroscopy. The experimental details are discussed in the following sections. First, the origin and specifications of the ultrashort pulses that were directed at the molecules during the experiments are outlined. Then the molecular beam source is briefly discussed followed by the experimental procedure.

3.2.1 Free-Electron Laser and optical pump-probe laser at FLASH

The experiments are performed at the permanent C̲FEL A̲SG M̲ulti-P̲urpose (CAMP) end-station based at the BL1 at FLASH I [74]. The CAMP end-station is designed and equipped to perform electron- and ion- spectroscopy, imaging, and pump-probe experiments. Overall, we performed two kinds of experiments, one is the XUV-Vis pump-probe experiment and the other is IR-Vis pump-probe experiment. The XUV pulses are generated from FLASH. Whereas, the IR and Vis pulses are produced from the Ti:Sapphire optical laser. The beam transportation from the respective source of pulse generation to the experimental chamber is described for the FEL beam and then for the Ti:Sapphire optical laser.

3.2.1.1 Pathway of FEL beam to CAMP experimental chamber

The schematic of the FEL beam pathway to the CAMP end-station is shown in Figure 3.5. The radio-frequency (RF) photoinjector emits electron bunches. These electron bunches are accelerated to relativistic velocities in the superconducting accelerator unit and then guided to the undulator where micro bunches are formed. These electron micro bunches generate spatially coherent X-ray radiation. Since it is coherent and has laser-like properties, it is called a FEL. At FLASH, the electron bunches are distributed between two different undulators. The fixed gap undulator provides the radiation to the FLASH I experimental hall, whereas the variable gap undulator is used for FLASH II. At FLASH I, the FEL beam is passed through a series of transport mirrors to five different beamlines as shown in Figure 3.5.

The experiment described in this thesis was performed at BL1. After the beam is transported through the BL0M0 mirror, the single-shot photon energy spectrum is recorded *via* a variable line spacing (VLS) grating spectrometer. The pulse energy can be attenuated on the user side by changing the filters in the filter wheel consisting of several filters of various transmissions. After filtration, the beam is passed through more transport mirrors that are coated with carbon and nickel and offer different transmissions depending on the photon energy of interest. We performed experiments with 40.9 eV XUV photon energy for which we got 62% transmission of the pulse energy from these transport mirrors.

The beamline is also equipped with an optional Delay Stage for CAMP (DESC) unit that facilitates the XUV-pump and XUV-probe experiments. Finally, to focus the beam into the CAMP chamber two plane-elliptical micro-focusing Kirkpatrick-Baez (KB) mirrors are used [75].
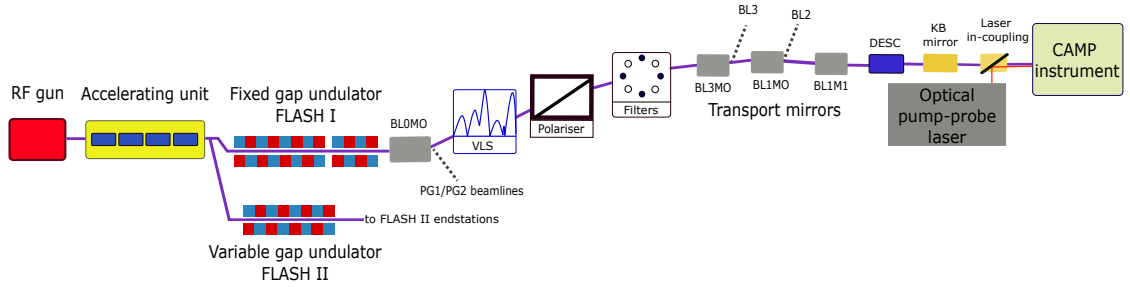
Figure 3.5: The pathway of the FEL beam from its source of origin to the CAMP instrument is depicted (not to scale). The FEL beam is generated by accelerating the electron bunch, produced by the radio-frequency (RF) gun, in the superconducting accelerating module. The produced bunches then pass through the varying magnetic field, that is, undulators where the formed electrons' micro bunches emit coherent X-ray radiation. FLASH I uses the fixed gap undulator, unlike FLASH 2 where a variable gap undulator is used. The formed FLASH I beam is then transported to various beamlines through transport mirrors BL0M0, BL3M0, BL1M0, and BL1M1. The radiation is measured and if needed, attenuated on the way to the instrument using the VLS grating spectrometer and filters, respectively. Delay Stage for CAMP (DESC) is an optional unit that enables XUV-pump XUV-probe experiments. The beam is finally focused into the CAMP experimental chamber using Kirkpatrick–Baez (KB) mirrors [75]. The optical pump-probe laser housed in the laser hutch is coupled to the setup using the laser in-coupling unit consisting of a drilled mirror that passes the FEL straight through a small hole in the mirror and reflects the optical radiation.

The measured XUV beamline parameters are recorded on the FLASH data acquisition (DAQ) system. As soon as the FEL beam enters the FLASH I experimental hall upstream of the undulator, there is a gas monitor detector (GMD, not shown in the figure) to measure the pulse energy and the pulse position of the beam. The photon energy measured *via* the VLS spectrometer is recorded as well. FLASH can provide photon energies in the range of 4.2 to 51 nm. In our experiments, XUV photons with 30.3 nm (40.9 eV) are used with a pulse duration of 80 to 90 fs. This pulse duration range is extracted from the pulse length of the electron bunch. The electron bunch pulse length was determined using a transverse deflecting radio frequency structure (TDS) of a specific design, known as Lola, which is explained in Ref. [76]. This LOLA-type TDS is employed at the FLASH to measure the electron pulse duration [77]. Other XUV beamline parameters are tabulated in Table 3.2.

Besides the possibility of carrying out the time-resolved XUV-pump and XUV-probe experiments, the combination of the XUV FEL beam and the beam from the Ti:Sa pump-probe laser based in the FLASH I experimental hall [80] provides experimental flexibility described in brief below. The XUV beam and the optical laser

Parameters	Values
Photon energy	4.2 - 51 nm
Pulse duration (FWHM)	$<$30-200
Pulse energy	1 - 500 µJ
Photons per pulse	10^{11} to 10^{14}
Peak power	1-5 GW

Table 3.2: XUV FEL beam performance at FLASH I [78, 79]

beam are aligned near-collinearly in the CAMP instrument by means of a drilled mirror (laser in-coupling unit) designed for spatial overlap of the laser with the XUV beam, as indicated in Figure 3.5.

3.2.1.2   Optical laser beam pathway to CAMP experimental chamber

The Ti:Sa optical laser centered at 810 nm (IR pulse) wavelength is housed in a laser hutch that is approximately 10 meters away from the CAMP experimental chamber. The second and third harmonics can be generated from the laser, and the outputs can be delayed with respect to the fundamental pulse with the help of a fitted delay stage, thus making pump-probe experiments independent of the FEL feasible. The schematic of this laser is shown in Figure 3.6. After the IR beam enters the CAMP end-station, it is split into two beams with the help of a beam splitter. One part of the beam is then passed through a single beta-barium borate (BBO) crystal where second harmonic generation occurs, providing a beam centered at 405 nm (Vis pulse). The second part of the beam remains as it is. For IR-Vis pump-probe experiments the IR and Vis pulses are aligned collinearly to each other using a dichroic mirror that transmits the Vis pulse arriving after a variable delay (induced by the optical delay stage) and reflects the IR pulse to the focusing optics. After this, the laser parameters are measured using the photon diagnostics unit. In the photon diagnostics unit, there is a beam sampler that reflects approx. 4% of the beam into camera 1 and camera 2 to measure the laser spot properties at the near-field and far-field regions.

In addition to the second harmonic generation, third harmonic generation is also possible (not shown in the figure) which provides pulses centered at 267 nm (UV pulse). A few mJ of pulse energy can be achieved with $\sim$50 fs pulse duration measured *via* the auto-correlator optimized at 810 nm. The photon energy is measured using a photodiode that is calibrated with a power meter, which is used to measure the pulse intensity operated at a 10 Hz repetition rate. The typical range of the pulse

energy at the fundamental wavelength (810 nm) is 5 to 10 mJ.
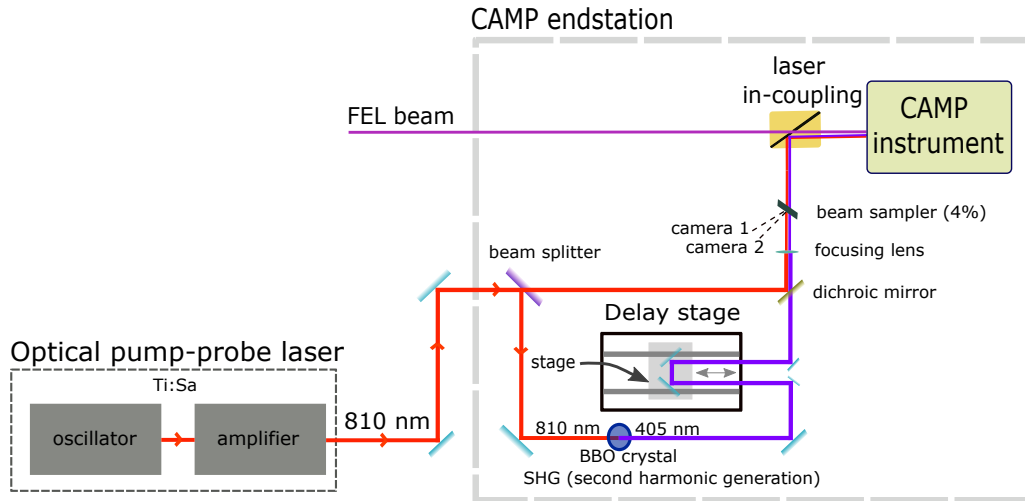
Figure 3.6: The optical Ti:Sa pump-probe laser is housed in the laser hutch that is situated near the CAMP end-station (approximately 10 meters away). The figure is not scaled to distances. The schematic of the optical beam pathway is represented where the optical components needed for focusing are not shown here. The beam splitter splits the fundamental IR beam (810 nm) into two beams. One part of the beam remains as it is shown by the red arrow. Another part is passed through a beta-barium borate (BBO) crystal to generate the second harmonic providing us the 405 nm radiation in the Vis range. The delay stage is used to provide an optical delay in the arrival of the Vis pulse compared to the 810 nm fundamental if moved to the left. The stage can be moved back and forth, which allows to scan over the delay times and perform time-resolved experiments. The time-delayed Vis pulse is then aligned collinearly with the IR pulse using the dichroic mirror that transmits the Vis pulse and reflects the IR pulse. The output of the laser is then guided to the CAMP chamber with the help of drilled mirror (laser in-coupling unit) where the laser is overlapped spatially with the XUV beam (if needed).

We performed XUV-Vis and IR-Vis pump-probe experiments by varying the delay between the two pulses. The delay is controlled with the help of the delay stage housed in the CAMP end-station. The schematic of the delay stage is shown in Figure 3.6. This optical delay stage setup has a motor that enables the stage to move back and forth and hence induces an optical delay in the Vis pulse if moved to the left and vice versa. The stage can be moved with the precision of one micron. We thus can scan the variable delay in the range of about ten nanoseconds with a

few femtoseconds step sizes. To ensure the reliable measurement of this delay time that depends on the position of the stage, an encoder is mounted on the delay stage to record this motor position. Since the encoder is linked to the DAQ system, exact motor position values are recorded that provide precise measurements of the delay time between the XUV and the Vis pulse and also between the IR and the Vis pulse.

When we perform the pump-probe experiments involving the combination of the FEL and the optical laser, the synchronization between them becomes crucial [81]. Throughout the FEL facility, the reference trigger to all the devices is controlled by the optical master laser oscillator. The synchronization of the arrival time of the two pulses (FEL and the optical pulse) needs to be done with a precision of the order of a few femtoseconds since this limits the temporal resolution of the time-resolved experiments. The major source of the jitter in the FEL arrival time is the fluctuation in the electron bunch arrival time [82]. To account for this jitter, the electron bunch arrival time is recorded by bunch arrvial time monitor (BAM) placed after the accelerating unit, and the delay values are compensated for this measured jitter during the analysis.

Overall, for the current experiments, the following crucial diagnostics are recorded. The pulse duration and pulse energy of both the FEL beam and the optical laser beam, the FEL beam arrival time, and the delay time between the pump and probe pulse.

3.2.2   Molecular source

The fluorene sample is bought from Sigma-Aldrich as a powder that is sublimated into the gas phase *via* heating. In these experiments, the gas jet is prepared in the following manner. The powder sample is inserted into the cartridge of an Even-Lavie pulsed valve [83]. This valve is well suited to perform experiments with PAHs as using this valve the sample can be heated up to higher temperatures (276°C) than a general valve (105°C [84]). In our experiments, fluorene molecules are heated up to 200°C to bring the molecules into the gas phase. The valve's opening time can be varied to attain the temporal overlap between the molecules and the pump and probe pulses, which is set to 30 µs in this case with a 10 Hz repetition rate compatible with the repetition rate of the laser. The supersonic expansion is achieved using helium as a carrier gas at one bar. This molecular beam is then passed through two skimmers to provide a well-collimated molecular beam.

3.2.3   Experimental procedure

So far, all the components required to perform the experiments are explained. The spectroscopic method using these components is described in this subsection. The CAMP instrument offers users to install their own detectors and valves at the free

ports of the instrument. For the described experiments, an Even-Lavie pulse valve is set up at one of the free ports of the CAMP instrument such that the molecular beam is perpendicular to the pump and probe pulses, and also to the detectors that are mounted on other top and bottom free ports forming a double-sided VMI spectrometer. We used this spectrometer to record the ion yields, the ion momenta, and the electron momenta of the fragmentation and ionization products of the fluorene molecules using time-resolved pump-probe spectroscopy. The focus of this thesis is to investigate the ions and hence detailed description related to electron data is absent.

The schematic of the experiment is illustrated in Figure 3.7. The molecular beam enters the interaction region where it is irradiated by the pump pulse aligned perpendicularly to the molecular beam. After the variable delay, the probe pulse crossing the pump pulse at an angle ($\sim 1.5°$) interacts with the molecular system already excited by the pump radiation. In this process, the molecules are ionized and can also dissociate. The electrons and the cations formed are velocity-mapped onto the bottom and top detector assembly, respectively. Near the interaction region, the polarity of the repellor plate voltages is set such that they repel the cations and attract the electrons and vice versa for the extractor plates. After getting extracted, the cations pass through a series of voltage plates, where the voltages are optimized for VMI. The ions are detected by the top detector assembly constituting a microchannel plate (MCP), a phosphor screen P47, and a pixel imaging mass spectrometry (PImMS) camera [85, 86].

When the ions hit the MCP, an electron avalanche begins, and the corresponding total current is measured using a 2-GHz analog to digital converter (ADQ2AC-4G-MTCA, SP devices). This total current versus the recorded arrival time of these ions (TOF) can be plotted, and the TOF is calibrated to the m/z to provide us the TOF mass spectrum. The current obtained through the MCP reaches the phosphor screen and initiates the fluorescence that is captured by the 324 x 324 PImMS camera. The PImMS camera is designed to perform multi-mass imaging and record TOF values and velocity-map images.

During one experimental run, the delay time between the pulse and probe radiation is varied in the range of a few picoseconds with a few femtoseconds step sizes. At each delay value around 300 acquisitions (or 300 shots) are performed at a 10 Hz repetition rate in order to achieve enough statistics, where the electron and ion velocity map images are recorded simultaneously.
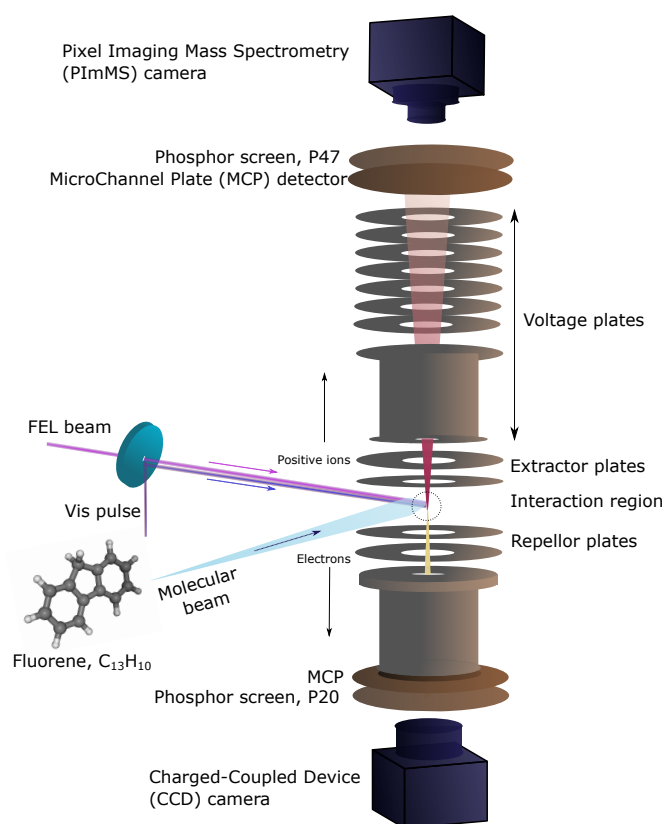
Figure 3.7: The schematic of the double-sided VMI spectrometer is shown. The supersonically expanded molecular beam enters the interaction region where it interacts with the pump and the probe pulse arriving with a variable delay between them. The electrons and the ions are guided to the bottom and the top detector assembly, respectively, with the help of appropriate extraction and repulsion voltages. The top detector assembly consists of a microchannel plate (MCP) detector used to acquire the TOF mass spectrum, a phosphor screen P47, and the pixel imaging mass spectrometry (PImMS) camera to record velocity-map images for all ions formed. The electrons are detected simultaneously using an MCP, a phosphor screen P20, and a charged-coupled device (CCD) camera. The beam paths after the interaction are not shown for clarity.

Chapter 4

Technical details of data analysis

4.1 Fitting of the NEXAFS spectra

The photon absorption spectrum obtained during the experiments provides the resonant peaks of the transition from the carbon $1s$ orbital (initial state) to UMOs (final state). To interpret the spectral information, the experimental spectrum needs to be fitted with a model that describes it the best and reveals the parameters crucial to understand the absorption transitions. Here, these parameters are the peak positions representing the resonant transition energies from the initial to the final molecular orbitals and the peak widths that can reveal the radiative lifetimes along with the uncertainty in the experimental photon energy values. During the experiments, due to the finite radiative lifetime of the final occupied state in a transition, the natural broadening is present that is governed by the Lorentzian lineshape $L(E)$, where E is the incident photon energy. These experimentally recorded photon energies also have a certain uncertainty, generally approximated by a Gaussian distribution $G(E)$. These two lineshapes ($G(E)$ and $L(E)$) are convoluted to yield the Voigt profile ($V(E)$), which is employed in our fitting model.

Analytically, we obtained the fitted parameters, $i.e.$, the respective peak positions and line widths, using a fitting routine implemented via a dedicated home-written script using the commercial software Origin. This routine is described in detail in Ref. [87] and here in brief.

The fitting routine employs the fit function $C(E)$ evaluated as a result of the convolution of Fano line profile $F(E)$ and the Gaussian profile $G(E)$. We use a limiting case of this fit function as our fitting model, which is described as follows. Fano line profiles are known as appropriate line-profile functions for the asymmetric line profiles encountered mostly in photoionization experiments of atoms [70, 88, 89] due to the combination of resonant and non-resonant ionization. The $F(E)$ is given

by

$$F(E) = \left| \frac{A}{q^2 - 1} \right| \frac{2}{\Delta_{\mathrm{L}} \pi} \left[\frac{(\epsilon + q)^2}{\epsilon^2 + 1} - 1 \right]. \tag{4.1}$$

Where A is the normalization constant, q is the asymmetry parameter of the peaks, Δ_{L} is the Lorentzian line width, and ϵ is the reduced energy given by

$$\epsilon = 2 \frac{E - E_{\mathrm{res}}}{\Delta_{\mathrm{L}}}. \tag{4.2}$$

Here, E is the incident photon energy, and E_{res} is the resonant energy of the transition. In the limit $q \to \infty$, the peaks become highly symmetric, and Fano line profile describes the Lorentzian profile $L(E)$ that is given by

$$L(E) = A \frac{2}{\pi} \frac{\Delta_{\mathrm{L}}}{4(E - E_{\mathrm{res}})^2 + \Delta_{\mathrm{L}}^2}. \tag{4.3}$$

The Gaussian distribution is given by Equation 4.4

$$G(E) = \frac{2}{\Delta_{\mathrm{G}}} \sqrt{\frac{\ln 2}{\pi}} \exp\left(-\frac{4 \ln 2 E^2}{\Delta_{\mathrm{G}}^2} \right) \tag{4.4}$$

where Δ_{G} is the Gaussian full-width half maximum (FWHM). The convolution $L(E) \otimes G(E)$ results in a Voigt profile $V(E)$ defined as

$$V(E) = \int_{-\infty}^{\infty} L(E') \otimes G(E' - E) dE'. \tag{4.5}$$

Substituting the Gaussian and Lorentzian functions into Equation 4.5 gives

$$V(E) = A \frac{4}{\pi \Delta_{\mathrm{G}}} \sqrt{\frac{\ln 2}{\pi}} \int_{-\infty}^{\infty} \frac{\Delta_{\mathrm{L}}}{4(E' - E_{\mathrm{res}})^2 + \Delta_{\mathrm{L}}^2} \exp\left(-\frac{4 \ln 2 (E' - E)^2}{\Delta_{\mathrm{G}}^2} \right) dE'. \tag{4.6}$$

To simplify Equation 4.6, the following substitutions can be considered.

$$t = \frac{2\sqrt{\ln 2}(E' - E)}{\Delta_{\mathrm{G}}}, \ x = \frac{2\sqrt{\ln 2}(E_{res} - E)}{\Delta_{\mathrm{G}}}, \text{ and } y = \frac{\Delta_{\mathrm{L}} \sqrt{\ln 2}}{\Delta_{\mathrm{G}}}. \tag{4.7}$$

$V(E)$ in Equation 4.6 now can be rewritten as

$$V(E) = A \frac{2}{\pi \Delta_G} \sqrt{\frac{\ln 2}{\pi}} \int_{-\infty}^{\infty} \frac{y e^{-t^2}}{(t - x)^2 + y^2} dt \tag{4.8}$$

The computation of the integral given in Equation 4.8 can be achieved efficiently by using the well-known Faddeeva function ($W(z)$ a scaled complex error function [90–92]) [93–96]. This function is defined for $\Im z = y > 0$, where $z = x + \mathrm{i}y$, as

$$W(z) = \frac{i}{\pi} \int_{-\infty}^{\infty} \frac{e^{-t^2}}{z - t} dt. \tag{4.9}$$

The integral can be separated into real and imaginary parts given by

$$\Im[W(z)] = \frac{-1}{\pi} \int_{-\infty}^{\infty} \frac{(t-x)e^{-t^2}}{y^2 + (t-x)^2} dt \qquad (4.10)$$

$$\Re[W(z)] = \frac{1}{\pi} \int_{-\infty}^{\infty} \frac{ye^{-t^2}}{y^2 + (t-x)^2} dt. \qquad (4.11)$$

The imaginary and the real parts of the Faddeeva function and the nonlinear square fitting approach using the Levenberg-Marquardt iteration algorithm are used to fit the experimental data with the fit function $C(E)$ given by

$$C(E) = \left| \frac{A}{q^2 - 1} \right| \frac{2\sqrt{\ln 2}}{\Delta_{\mathrm{G}}\sqrt{\pi}} (q^2 - 1)\Re[W(z)] - 2q\Im[W(z)]. \qquad (4.12)$$

This is a result of the convolution of the Fano line profile (Equation 4.1) with the Gaussian profile (Equation 4.4). It is to be noted that in the limiting case of the asymmetric factor 'q' $\to \infty$ (depicting a symmetric line profile), the fit function $C(E) \to V(E)$ since $F(E) \to L(E)$. The absence of the asymmetric feature in the experimental data makes the inclusion of the asymmetric factor redundant. Therefore, we employed the limiting case of Equation 4.12 by setting the asymmetric factor value q to an arbitrarily chosen high value of $q = 2000$ and thus ensuring the usage of the Voigt profile for our fitting model. The experimental results fit using well-tested and used scripts [97–99] are shared in the results section in Chapter 5.

4.2 Analysis routine compilation for femtosecond pump-probe experiments at CAMP@FLASH

The data analysis routine followed in this work consists of three main stages as shown by the schematic depicted in Figure 4.1. The first stage is the data extraction stage, where we access, collect, clean, pre-process, and process the raw data obtained during the pump-probe experiments using CAMP@FLASH. Some part of the extracted data needs a fitting tool to be understood and therefore passed as input to the second stage called the fitting stage. The combined outputs of the analysis routines from the data extraction stage and the fitting stage are finally our experimental results. The open-source libraries and codes used for the analysis are written using Python software [100]. The data extraction methodology and the fitting model are discussed in the next two sections, with information on all the collected data. The final results are shown and discussed in Chapter 6.
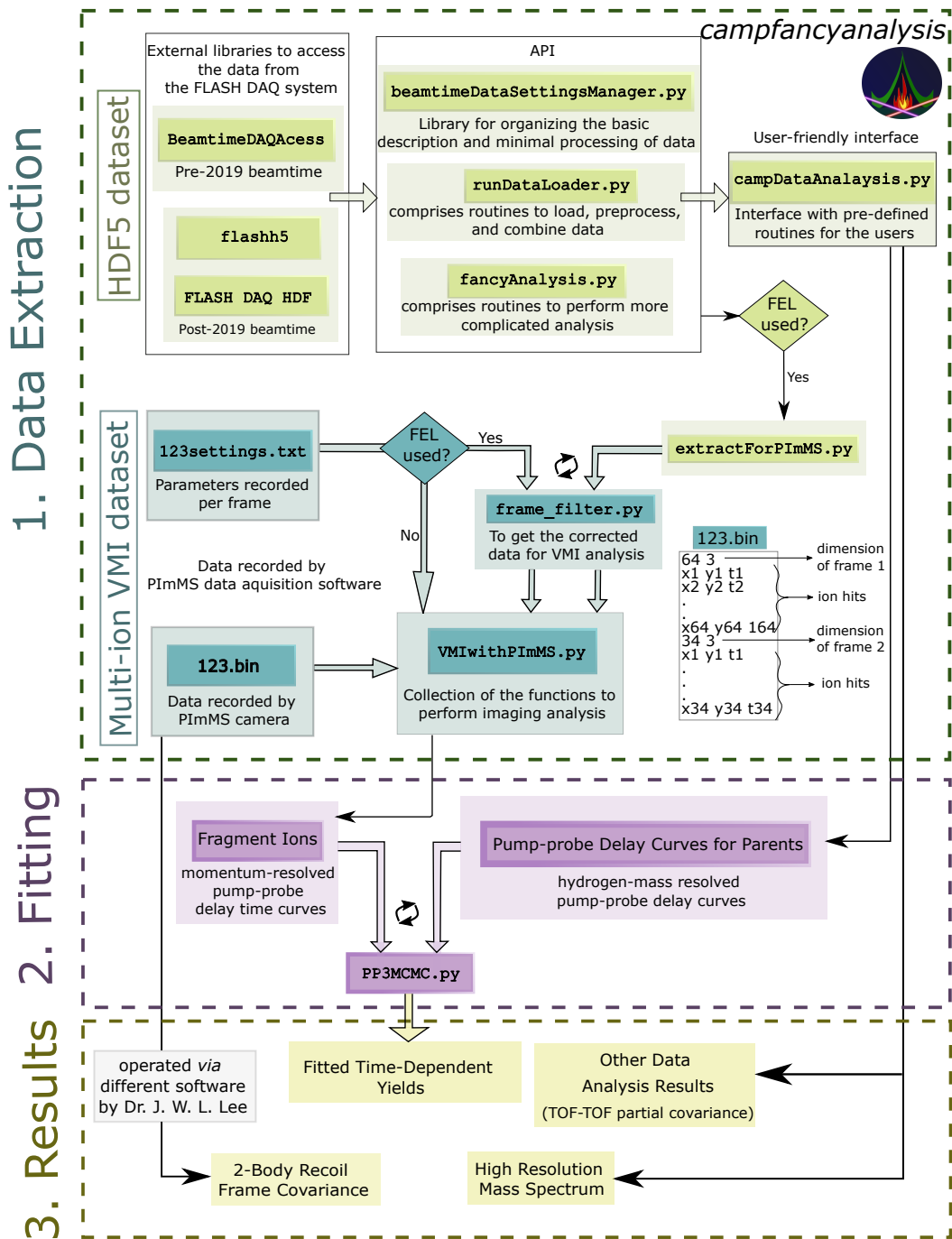
Figure 4.1: The schematic illustrating the three stages of the data analysis routine using the program campfancyanalysis, namely, data extraction, fitting, and results.

4.2.1 Extraction of the experimental data

We use the combination of two methods, namely, time-of-flight mass spectrometry (TOF-MS) and velocity-map imaging (VMI), to obtain observables for our ultrafast femtosecond pump-probe spectroscopy experiments on PAHs. The VMI data is recorded using a pixel imaging mass spectrometry (PImMS) camera [101, 102]. This camera records the images independently of the other datasets. Due to multiple data collection sources, the datasets are broadly classified on the basis of their storage format and are described in the following two subsections. The in-house-developed open-source campfancyanalysis software used to perform the forthcoming analysis is available from the Git repository [103].

4.2.1.1 HDF5 datasets

The devices that are installed in the CAMP endstation at FLASH 1 experimental hall record the data in the FLASH data acquisition (DAQ) system along with the other data stream from FLASH itself, except the data recorded by the user-operated PImMS camera. The DAQ system enables data storage in the hierarchical data format (HDF5). The HDF5 dataset extraction scheme is shown with the block at the top, marked in the yellow-green shade, in Figure 4.1.

Following the scheme, the first step is to access the data from the DAQ system that is done *via* external libraries, namely, `BeamtimeDAQAccess`, `flashh5`, and `FLASH DAQ HDF`. Apart from the `BeamtimeDAQAccess` library, the other two external libraries are required to analyze the experimental data recorded after the year 2019. Since during the course of this thesis, data recorded in beamtimes before 2019 (pre-2019) is analyzed, the `BeamtimeDAQaccess` library is used to access the data. Through these external libraries, the data is accessible *via* application programming interface (API). API has three libraries, where the data is cleaned (`beamtimeDataSettingsManager.py`), pre-processed (`runDataLoader.py`), and prepared to be analyzed (`fancyAnalysis.py`). The user-friendly interface provides a ready-to-run Python script `campDataAnalysis.py` that offers a command-line interface for data visualization operation. The external libraries along with the API are described in detail in Ref. [104]. The features and working steps of `campDataAnalysis.py` are described here.

To run the script successfully, the user needs to provide some information as shown in Figure 4.2, including the experimental run number (R), the location of the HDF5 file (H), the name of the molecule under investigation (M), and the type of experiment (S) with choices pump only/probe only/pump-probe/background/altogether. This information is parsed to the script using the Python module 'argparse'. The command to run the script is, for example,

```
$python campDataAnalysis.py -R 1234 -H apfs3/flash/gpfs/bl1/hdf
```

45

```
-M phenanthrene -S pump-probe
```

In this command, 1234 is the experimental run number, apfs3/flash/gpfs/bl1/hdf is the path where the HDF5 files are stored, phenanthrene is the molecule of interest, and pump-probe is the type of experiment. In addition to this information, an input file called `input.inp` is taken by the script by default. This file is essential to provide necessary information about the experimental observables, for example, the time-of-flight spectrum, the pump-pulse energy, the probe-pulse energy, the fluctuations in the FEL beam arrival time recorded by bunch arrvial time monitor (BAM) called as BAM correction throughout the text, and the FEL shutter value. More observables can be added to this file if required to carry out the analysis. For each of these observables, the following parameters are given in the `input.inp` file.

1. Pathway: The location at which the observable is stored in the HDF5 file.

2. Dimension: The dimension of the dataset is important to handle the data. Possible choices are 0, 1, and 2. '0' is for scalar datasets, e.g. the pulse energies, correction values recorded by BAM, FEL shutter value, etc. '1' and '2' depict vector datasets. For example, '1' is chosen for the mass spectrum, whereas '2' is chosen for 2D datasets such as imaging matrices.

Along these essential parameters, the data can be filtered and pre-processed by the user before the final analysis using the following keywords.
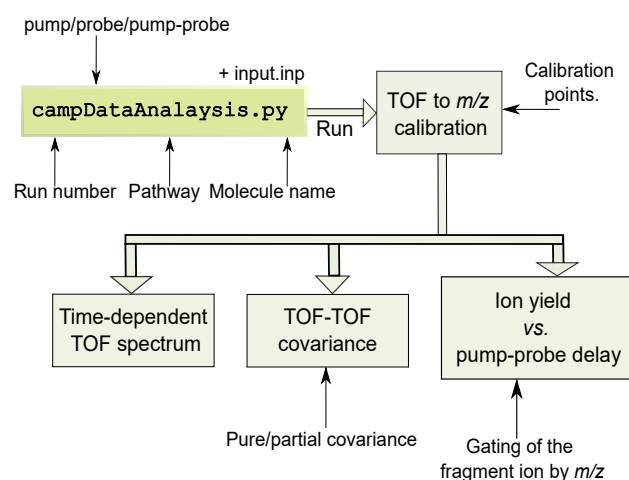
Figure 4.2: Illustration of the `campDataAnalsis.py` script. The black arrows indicate the inputs that are needed to perform the tasks written in the respective boxes.

1. HowToMakeScalar: This is required in the case when scalars are needed but vectors are recorded. Conversion from a vector to a scalar can either be done through averaging, by choosing the "average" keyword, or by choosing the non-negative integer number that corresponds to the certain component of the vector.

2. YesIfOverThreshold: This feature is valid only for scalar datasets, and it is optional. As the name suggests, this is a boolean parameter and accepts the values True/False/Yes/No. The values above a given threshold are filtered depending on this parameter.

3. MarkupThreshold: This is the threshold value for the data to be True. Using this value, an additional array of the boolean data (containing True/False) is created, which performs the logical operations with the datasets for which the threshold is set.

4. MinVal/MaxVal: These are the minimum and the maximum values of the data to be used.

5. VectorCompressionCoeff: Large vectors can be compressed into smaller vectors by averaging the neighboring points, where this coefficient is the number of points that are to be averaged.

Further parameters for pre-processing the data are described in Ref. [104]. The data to be analyzed is thus provided to the `input.inp` along with these parameters. For example,

```
[BAMcorr]
pathway: /Electron Diagnostic/BAM/4DBC3/electron
dimension: 0
HowToMakeScalar: 0
```

Here, the key `[BAMcorr]` depicts the value of the fluctuations in the FEL beam arrival time measured by the BAM. The pathway within the HDF5 file is provided in addition to the dimension. Similarly, other observables can be defined in this file.

After the script is run successfully, it gives out a time-of-flight (TOF) spectrum, and the following tasks can be performed as also shown in the schematic in Figure 4.2.

1. TOF to mass over charge ratio (m/z) calibration: As soon as the script is run, it provides the TOF spectrum, which can then be analyzed. The command-line interface allows the user to input the calibration points that can be saved into a text file. This text file can be used later directly when the script is run again.

Calibration of the TOF spectrum to time-of-flight mass spectrum involves the mapping spectral intensities from TOF domain to m/z domain. Since these two coordinate systems are not linearly dependent, the Jacobian determinant is used while performing the calibration.

2. Time-dependent TOF spectrum: During the experiments, the TOF spectrum is acquired while scanning the time delay between the pump and the probe pulse (Δt). The 3D surface can be plotted using this option where the x-axis is Δt, the y-axis is the TOF axis, and the z-axis depicts the intensity. The Δt values are corrected for BAM correction.

3. Plotting ion yield *vs.* pump-probe delay time (IYvsDelay) curves for different fragment ions: This feature is of particular importance since it provides the user with the IYvsDelay curves of individual fragment and parent ions. The command-line interface allows the user to provide the gating for the desired ion by providing the minimum and maximum value of particular m/z values that can be extracted from the TOF-MS spectrum. The Δt values are corrected for BAM correction. In addition to this, to correct the dependence of the ion yield on the fluctuation of the FEL pulse energy, the user is asked to enter the number of photons absorbed during the process. Generally, entering '1' is a good approximation in XUV photon absorption case as can be estimated from Table 8.3 in Section 8.2.5 of Appendix. Otherwise, the number of photons can be estimated using the method described in Section 8.2.5 of Appendix.

4. TOF-TOF covariance: The TOF-TOF covariance can be performed by directly choosing this option from the menu shown in the command-line interface. The user can control the parameter 's' that varies the analysis between pure covariance and partial covariance. Where $s = 0.0$ is the pure covariance condition and $s \geqslant 1.0$ is the partial covariance as explained in Ref. [104]. The command line also offers more personalized graphical options to choose the optimum color scale or display options.

Future scope of improvement: Implementing a graphical user interface can be seen as another area of improvement.

4.2.1.2 Multi-ion VMI dataset

As mentioned in the experimental chapter, the ions are velocity mapped onto the PImMS camera that records the data separately from the FLASH DAQ system. To keep track of simultaneous measurements of the HDF5 dataset and the VMI dataset, the experimental run numbers recorded by the PImMS camera and the DAQ system are listed against each other during the experiments. Each experimental

run comprises several acquisitions with a repetition rate of 10 Hz (see experimental techniques chapter), and the common and unique tag between the two datasets (recorded by both the PImMS camera and the FLASH DAQ system) is the Bunch ID. These Bunch IDs in each experimental run can be used to synchronize the results from the independent data sources. The data storage format of the PImMS camera is discussed below followed by the data extraction scheme of the imaging dataset.

Data storage: The PImMS camera is designed such as it records the 3D information of the ions, that is, the TOF (t) and the position on the detector (x,y). This 3D information facilitates multi-mass imaging [85]. During experiments, each acquisition consists of multiple ion hits that are captured by the camera, which in turn provides a velocity-mapped image and TOF spectrum. The collection of this 3D information for one acquisition or one Bunch ID is referred to as one 'frame'. The format of the recorded data is shown on the right side in 'stage I Data extraction' of Figure 4.1. The three columns of the dataset are the x-position, y-position, and the arrival time of a single ion hit. Each row in individual frames depicts a single ion hit, and the number of ion hits per frame is different for each frame. The dimension of the dataset along with the dataset itself is stored in a binary format file, named, for example, `123.bin` files. While acquiring the data, other parameters are also needed to be recorded for each frame. For example, the Bunch ID, the signal level, and the Δt value. These parameters are recorded in the ASCII tab-limited files `123settings.txt`. The Bunch IDs recorded by the PImMS can lag with one or two frames as compared to the Bunch IDs recorded in DAQ system. The ASCII files with the corrected Bunch IDs recorded using PImMS along with other parameters are provided by collaborators in the file `123settings-corrected.txt`. The corrected Bunch ID makes synchronization of the DAQ dataset with the PImMS recorded dataset feasible. When the FEL is not used, for example, in the IR-Vis pump-probe experiments, the correction of the Bunch ID is redundant, and in this case, the file `123settings.txt` can be used directly.

These two files (`123.bin` and `123settings.txt`/`123settings-corrected.txt`) are the input for the `VMIwithPImMS.py` scripts. The extraction routine of the data recorded by the PImMS camera is depicted by a schematic shown in teal color in Figure 4.1. In the case when the FEL is involved as one of the pump or probe pulses, it becomes crucial to correct for the fluctuations in the beam arrival time and the FEL pulse energy. The parameters relevant to correct for these fluctuations (the unique Bunch ID (important to synchronize the imaging data and the HDF5 data), the pulse energy of the pump pulse, the pulse energy of the probe pulse, and the jitter-corrected pump-probe delay value) are recorded in the HDF5 files and easily be extracted using the `extractForPImMS.py` script based on the API of the campfancyanalysis software as shown in Figure 4.1. Since the API also cleans the data for zeros or NaNs, the user also gets Bunch IDs of the clean data in

bonus, which can be filtered for in the next step by the script `frame_filter.py` (see Figure 4.1). The objective of this script is to synchronize the HDF5 datasets and the multi-ion VMI dataset. This is done by identifying the common Bunch IDs. If the Bunch ID is common, the information about the relevant parameters is stored (`frame_BID_FELpower_corrdelay_<rn>.txt`), otherwise, the frame number is recorded (`frames_to_remove_<rn>.txt`).

The user is now fully equipped to process and visualize the data using the collection of functions in the `VMIwithPIMmMS.py` script (see Figure 4.1). The working steps of the analysis routine are presented in the schematic in Figure 4.3. The user needs to provide some values for initializing the procedure, namely, the PImMS run number/s, the TOF range (initially the whole range is used), a name to indicate which TOF range has been selected, a flag whether FEL is involved, and the number of photons involved (by default set as '1'). Later as the analysis is carried out, further parameters are needed to be provided by the user.

The flow of the analysis routine is as follows:

1. Load Data: The function `getTOF_VMI()` reads the '`.bin`' file to get the TOF spectrum and the recorded VMI, mentioned as '1. Plot TOF' in Figure 4.3. The user can analyze the data for a single fragment ion by gating peaks in the TOF spectrum ('2. Gating single ion'). The VMI and time delay between the pump and the probe pulse (Δt) values are extracted for all the frames for the gated ion ('3. VMI and ppdelay'). The frames are the acquisitions, and for each Δt value, multiple acquisitions are acquired. The VMI is summed over all the frames to get a 'single' ion image.

2. Static Analysis: It consists of three stages:

   (a) Image Centering: Due to experimental conditions, the ions are not at the exact center of the camera. The centers of the ion images are found by using the function `getcenteredVMI_static()`.

   (b) Abel Inversion & Radial Distribution: After the center is identified, the VMI 2D image depicting the projection of the 3D velocity vector distribution is reconstructed to a 3D distribution, and a center slice of this 3D reconstructed distribution is extracted using the Abel inverse transformation. This transformation is implemented in the PyAbel package [100, 105] of the Python software using several methods. For the results of this thesis the 'onion peeling' method is employed. The Abel-inverted image is then angularly integrated which provides the radial distribution of the image, which is also performed using the PyAbel package. The corresponding function for these tasks is `abel_invert()`.

50
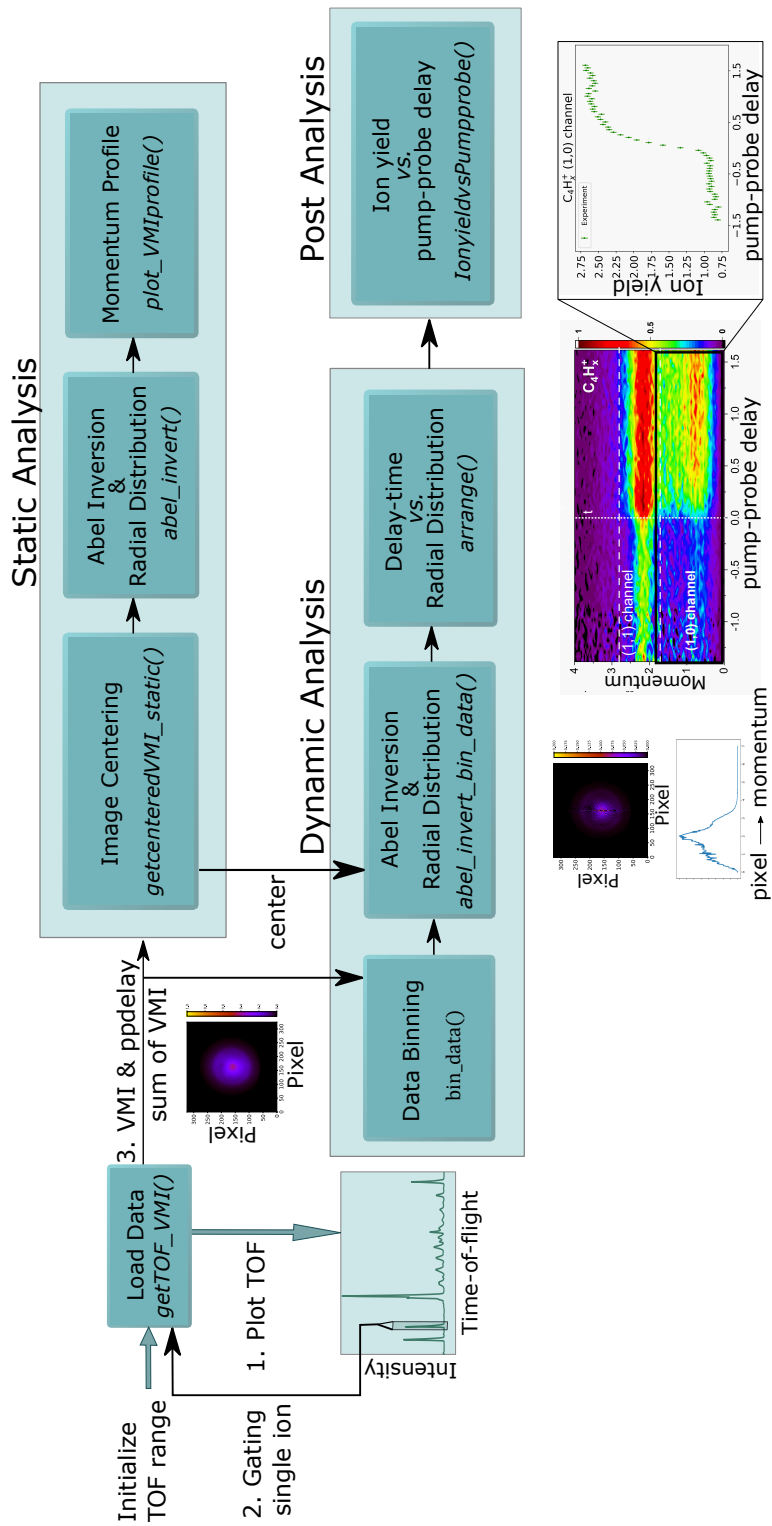
Figure 4.3: Elements of the VMIwithPImMS script. First, the data is loaded, followed by the static analysis, dynamic analysis, and the final datasets are extracted from the post-analysis stage.

(c) Momentum profile: The radial distribution obtained using the function `abel_invert()`, can be calibrated from pixel units to momentum units. The calibration factor is calculated using the software SIMION using a procedure provided by collaborators. Given the calibration points, the momentum *vs.* intensity curves are obtained using the `plot_VMIprofile()` function, which is useful to interpret different momentum regimes of the results.

3. Dynamic Analysis: It also consists of three stages:

   (a) Data Binning: The raw data obtained from the `getTOF_VMI()` is grouped by Δt values. For example, the VMI images corresponding to a certain range of Δt values are averaged together into a single bin, and the bin value is governed by the Δt value at the center of the range.

   (b) Abel Inversion & Radial Distribution: Abel inversion of the 2D image is performed around the center of the ion image. This center is already known from the static analysis. Using these image centers, the Abel inverted images and their radial distributions are obtained for binned Δt values using the function `abel_invert_bin_data()`.

   (c) Δt versus Radial Distribution: To visualize the Δt dependent radial distribution, the data is saved in a 2D array such that the first, second, and third columns are binned Δt, pixels/momentum, and intensity, respectively. The `arrange()` function is employed for this task. The data is plotted using Origin, and a so-called "heatmap" is obtained.

4. Post Analysis: The momentum profile (static analysis) together with the Δt versus radial-distribution (Dynamic Analysis) plots provide information about different momentum regions. These momentum regions are integrated over momentum to obtain the IYvsDelay curves for different fragment ions.

Future scope of improvement: This script can be further developed into a user-friendly package by implementing either the command-line interface or the graphical user interface.

4.2.2 Fitting the ion yield versus pump-probe delay time curves

4.2.2.1 Preparing the datasets for fitting

The data extraction stage of the analysis routine provides the ion yield *vs.* pump-probe delay time (IYvsDelay) experimental curves, as shown in the schematic of the

analysis routine in Figure 4.1. The IYvsDelay curves for the parent ions are acquired from the TOF values recorded at the MCP detector. At each time delay the ion yield is calculated by integrating over the time-of-flight region of the respective parent ion. Determination of the ion yield by integrating the time-of-flight values at each pump-probe time delay is more accurate than integrating the intensity of the ion images at each time delay because the parent ions always arrive at the center of the detector and therefore the images are subjected to saturation. Whereas, the fragment ions have a finite velocity spread and are relatively less susceptible to saturation than the parent ions. Therefore, the IYvsDelay curves for the fragment ions can be determined by integrating the intensity of the ion images recorded using the PImMS camera.

Using the ion images for the fragment ions is beneficial to get momentum resolved IYvsDelay curves, which are extracted using the `VMIwithPImMS.py` script. The script provides four IYvsDelay curves for each fragment ion. Out of these four curves, three curves are extracted by integrating the intensity of the ion image in three different momentum regions. The fourth one is the integration of the whole ion image, which should be similar to the result that we get from integrating the time-of-flight region of the fragment ion at each pump-probe delay.

To verify the results obtained using the `VMIwithPImMS.py` script, the IYvsDelay curve gathered by integrating the whole ion image (purple curve) is plotted with the IYvsDelay curve acquired by integrating the time-of-flight region (green curve) for an exemplary fragment ion in Figure 4.4. After scaling and applying an appropriate offset to the purple curve, a good match is observed between the two curves. The final data files for fitting are prepared using the script `column_scale.py`. This script performs two functions. First, the intensities of the IYvsDelay curves for three different momentum regions are separated in three data files and are adjusted for the scaling factor and the offset, which are determined using the method described before. Second, the error in intensity is estimated by calculating the standard deviation of the region of the IYvsDelay curve that is observed to be constant in intensity. For example, in Figure 4.4, the region before -0.5 ps illustrates constant intensity.

4.2.2.2 Fitting model

The fitting routine to fit IYvsDelay curves is implemented in the open-source in-house developed scripts written using the Python software called "PPMC3Fitting" [106]. The fitting functions are described in detail in Refs. [104, 107] and briefly here. The objective of fitting the IYvsDelay curves is to understand the dynamical processes involved in these observed experimental curves. In the pump-probe experiments, after interaction with the pump pulse, the molecules are excited to their vibronically excited states. These excited states have certain relaxation lifetimes denoted by τ_{r}. Depending upon how fast or slow the molecule relaxes from the vibronically excited

states to lower-lying states, three cases can be considered, as shown in Figure 4.5.
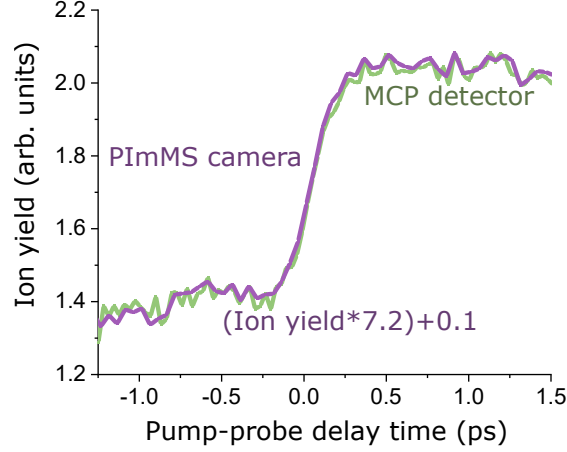
Figure 4.4: The ion yield *vs.* pump-probe delay time (IYvsDelay) experimental curves illustrate two methods by which they are extracted. The ion yields depicted by the green curve are determined by integrating time-of-flight values, which are recorded by the MCP detector, and the ion yields shown by the purple curve are obtained by integrating the intensity of the whole ion image recorded using PImMS camera. The purple curve overlaps with the green curve after scaling by a factor of 7.2 and applying an offset of 0.1.

The probe pulse would thus reveal three kinds of molecular responses depending upon these three cases. In the fitting model, these three molecular responses are convoluted to the experimental pulse shape. The signals thus obtained with the mathematical expressions of the processes involved are described as follows.

Since both the pump and the probe pulse are involved, the convolution of the two will be responsible for the evolution of the molecular system. The convolution of two functions (g and h) is generally defined by Equation 4.13.

$$\mathrm{f}(t) = g \otimes h = \int g(t)h(t - t')dt' \tag{4.13}$$

Further, if there are fluctuations in the arrival time of the pulses (τ_{jitter}), they should also be included in the convolution. Due to finite pulse width, the general expression of the pulse shape can be considered to have a Gaussian lineshape that is given in Equation 4.14 and depicted in Figure 4.5,

$$\text{Pulse shape}(t') = \exp\left(-\frac{t'^2}{\tau_{cc}^2}\right) \tag{4.14}$$

where t' is the distribution in the pump-probe delay time, τ_{cc} is the cross-correlation time of the two pump and probe pulses given by Equation 4.15

$$\tau_{cc}^2 = \frac{\tau_{pump}^2}{n_{pump}} + \frac{\tau_{probe}^2}{n_{probe}} + \tau_{jitter}^2 \tag{4.15}$$

Cases	Response	Pulse	Signal
(i) $\tau_r \to \infty$			$f_1(t)$
(ii) $\tau_r \sim \tau_r$			$f_2(t)$
(iii) $\tau_r \to 0$			$f_3(t)$
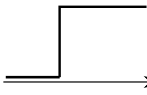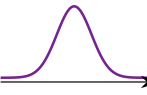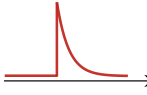
Figure 4.5: Three cases of the relaxation lifetimes of the transient states (τ_r) are depicted. For each case, the molecular response curve is shown, which is convoluted with the pump-probe pulse shape. The convoluted curve shows the functional dependence ($f_1(t)$, $f_2(t)$, and $f_3(t)$) of the observed signal for each case.

The functional dependence of the signal for three cases of τ_r are as follows:

(i) $\tau_r \to \infty$: The pump pulse excites the molecular system to the excited states that live for a much longer time than τ_{pp} and are seen in the experiments. If the relaxation lifetimes are infinitely long, the probe pulse would retrieve a constant molecular response, which will have a step-function-like dependence on the pump-probe delay time as shown in Figure 4.5. The obtained signal $f_1(t)$ would then be the convolution of the pulse shape with the Heaviside $\theta(t)$ function giving out an error function. The equation can be written as:

$$f_1(t) = \theta(t) \otimes \exp(-t^2/\tau_{cc}) \propto \left[1 + \mathrm{erf}\left(\frac{(t - t_0)}{\tau_{cc}}\right)\right] \tag{4.16}$$

where the function $\theta(t)$ is defined by,

$$\theta(t) = \begin{cases} 0, & \text{if } t < 0 \\ 1, & \text{if } t \geqslant 0. \end{cases} \tag{4.17}$$

Here, t_0 is the time when the pump and probe pulse overlap with each other.

(ii) $\tau_r \sim \tau_r$: If the relaxation lifetime τ_r has a comparable value to the experimental resolution given by the cross-correlation τ_{cc}, the probe pulse would observe an exponential decay of the excited states. The response of the molecular system is thus itself a product of the step function and the exponential decay.

$$f_2(t) = \left(\theta(t) \times \exp(-\frac{t}{\tau_r})\right) \otimes \exp(-t^2/\tau_{cc}) \tag{4.18}$$

The signal $f_2(t)$ that is then observed in the experiments will possess the transient functional dependence given by,

$$f_2(t) \propto \exp\left(-\frac{(t-t_0)}{\tau_r}\right) \times \left[1 + \mathrm{erf}\left(\frac{(t-t_0)}{\tau_{cc}} - \frac{\tau_{cc}}{2\tau_r}\right)\right] \times \exp\left(\frac{\tau_{cc}^2}{4\tau_r^2}\right) \tag{4.19}$$

(iii) $\tau_r \rightarrow 0$: In this case, the infinitely short spike in intensity can be thought of as a delta-shaped function. It will be observed by the probe pulse. The pump-probe time-dependent yield will portray a Gaussian function $f_3(t)$ given by,

$$f_3(t) = \delta(t) \otimes \exp(-t^2/\tau_{cc}) \propto \exp\left(-\frac{(t-t_0)^2}{\tau_{cc}^2}\right) \tag{4.20}$$

The final yield observed in the experiments $y(t)$ can be represented as a linear combination of all types of processes that can be observed. The experimentally observed ion yield versus pump-probe delay time curves can be fitted using these equations to retrieve the relaxation lifetimes of the vibronically excited states.

4.2.2.3 Fitting routine features

The IYvsDelay curves that are acquired from the experiments are used to retrieve the dynamical processes. These processes ($f_1(t)$, $f_2(t)$, and $f_3(t)$) are characterized by certain variables that are fitted using the Pump-Probe Multiple Channels Markov Chain Monte-Carlo Fitting (PPMC3Fitting) [106] script. The working routine of the script is explained in Refs. [28, 72, 104]. Here, the essential steps of the scripts are highlighted in brief. In this work, the non-linear variables are the overlap time of the pulses (t_0), the cross-correlation time of the two pulses (τ_{cc}), and the transient relaxation lifetimes of the excited state (τ_r) in the cases when transient and Gaussian features are retrieved from the experimental data. The possible distributions of these variables are sampled using the Monte-Carlo sampling procedure and then are solved using the Metropolis algorithm.

The block diagram to run the scripts is shown in Figure 4.6. Since the combination of multiple channels can be observed for a single IYvsDelay curve, the fitting model comprising of different combinations of channels is provided by the user in the
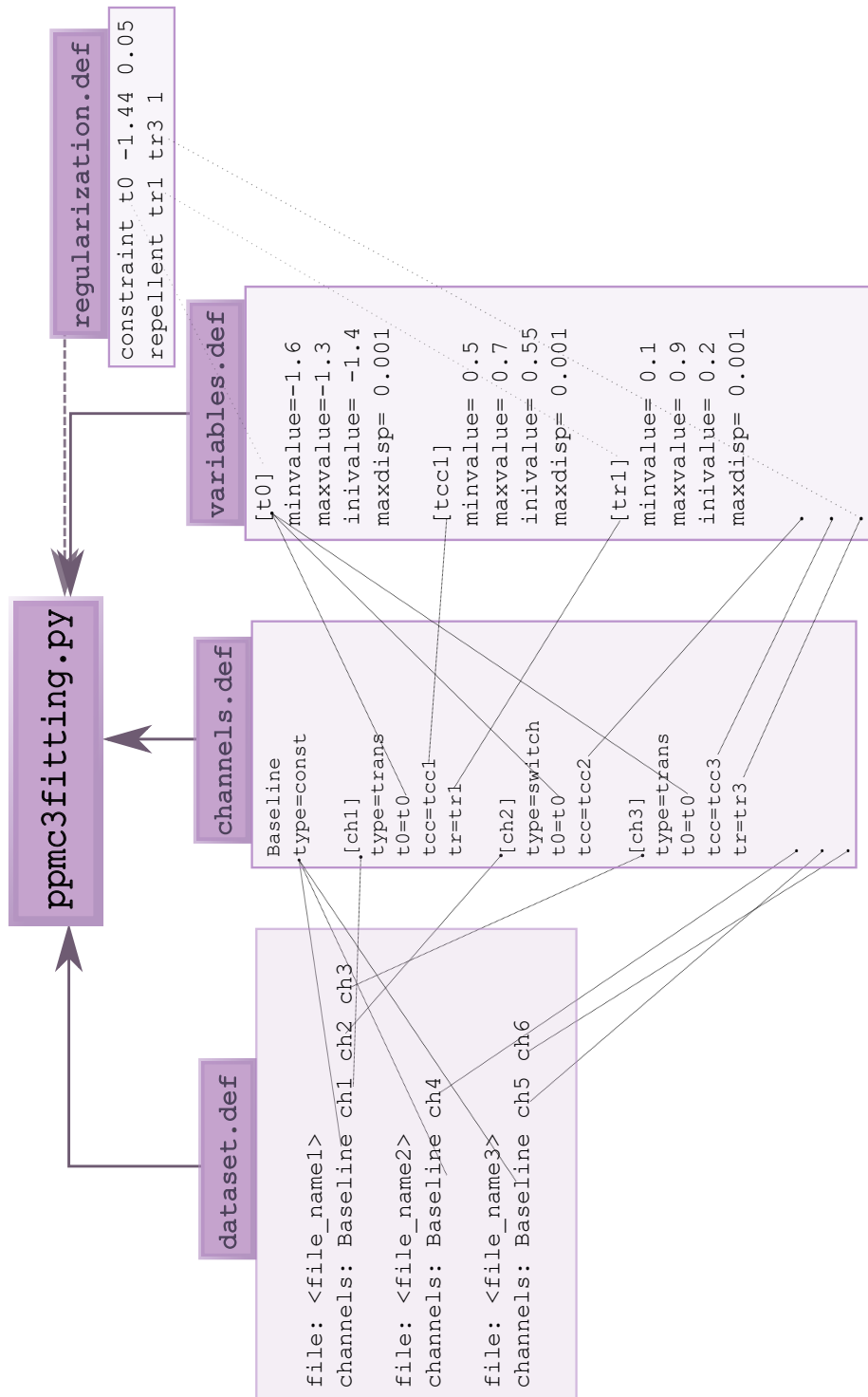
Figure 4.6: Block diagram showing the essential information needed as input for the PPMC3Fitting.py script.

`dataset.def` file along with the name of the file that contains the data to be fitted. Here, the word 'channels' is used extensively to represent different functions to which the data is fitted. For example, the channel can be of the form $f_1(t)/f_2(t)/f_3(t)$ that are dependent on the different variables as depicted in Figure 4.6. The variables that are required for each channel are named in the `channel.def` file, that is, the channel definition file. The variables are extensively defined by providing the initial value, minimum value, maximum value, and step size in the `variables.def` file. These three files are essential to run the fitting script as depicted in Figure 4.6. The parameters can also be restrained and these a priori assumptions can be provided in the `regularization.def` file, which is optional to run the script. Since one IYvsDelay curve may consist of several channels, the parameters of two channels can show linearly dependent behavior that needs to be avoided. The difference in the values (repellent value) of such parameters can be chosen such that these variables are not linearly independent. These parameters with the repellent value are defined in the `regularization.def` file. The `dataset.def` can contain multiple files to be fitted with shared variables, thus allowing fitting the multiple IYvsDelay curves simultaneously.

To summarize, Table 4.1 provides the name of the scripts used for the analysis along with their function.

Scripts	Function
`campDataAnalysis.py`	analysis of HDF5 dataset
`VMIwithPImMS.py`	analysis of VMI dataset
`PP3MCMC.py`	Fitting of the experimental data

Table 4.1: The name and function of the scripts that are used to carry out the analysis of the data collected during the experiments carried out at CAMP@FLASH.

4.2.3 Results collected from the analysis routine

In the final stage ('3. Results') shown in Figure 4.1, the major results obtained from the analysis so far are depicted in yellow color. This includes the high-resolution mass spectra obtained from the MCP readouts recorded in HDF5 datasets, along with other analysis outputs, for example, the TOF-TOF partial covariance results [72, 108]. The ion-yield *vs.* pump-probe delay time fitted curves are obtained for the parent ions and the fragment ions (integrated into different momentum regions). The two-body recoil-frame covariance analysis is also performed on the VMI dataset to discern the correlated ions. This analysis is done using a different software run by Dr.

J. W. Lee. The covariance mapping technique is described in detail in Ref. [109–112]. Briefly, in two-body (two-ion) recoil-frame covariance, the velocity distribution of one ion (i.e., the ion of interest) in reference to the velocity distribution of another ion (i.e., the reference ion) is calculated statistically as presented in Ref. [28]. All these results attained from the experiments that are part of this thesis are discussed in Chapter 6.

Chapter 5

Investigating the structural changes after single dehydrogenation and ionization of phenanthrene

5.1   Introduction

We employed the NEXAFS technique to investigate the electronic structure of the PAH phenanthrene in its single ionization and dehydrogenation state using the PIPE setup at P04 beamline at the PETRA III. The experimental setup and technique used are given in Section 3.1, while results are presented and discussed here in the following.

5.2   Photoreaction channels under investigation

In this section, the mass spectrum of the ion beam before the interaction with the photon beam (primary ion mass spectra), and after the interaction with the photon beam (product ion spectra) are illustrated. The primary ions and consequent product ions are m/z-selected, enabling us to probe specific photoreaction channels, which are mentioned in the following.

The primary ion beam is prepared as follows. During the experiments, the phenanthrene sample is heated up to 120°C to increase the vapor pressure. The vapor is passed through the permanent magnet 10 GHz ECRIS to produce the primary ions that are extracted using a 6 kV extraction voltage (see Section 3.1.1.2). The composition of the ion beam is characterized by scanning the magnetic flux of the

61

analyzer dipole magnet (AM), which is placed after the ECRIS. The energy provided by the ECRIS is enough to observe carbon backbone fragmentation and ionization of phenanthrene as is evident by the mass spectrum shown in Figure 5.1.

This primary ion mass spectrum is obtained by recording the ion current using the Faraday cup as a function of the magnetic field of AM. The magnetic field is calibrated to the mass over charge ratio (m/z). The primary ions are m/z-selected individually before they are guided to the 1.7-meter-long merged-beam interaction region.
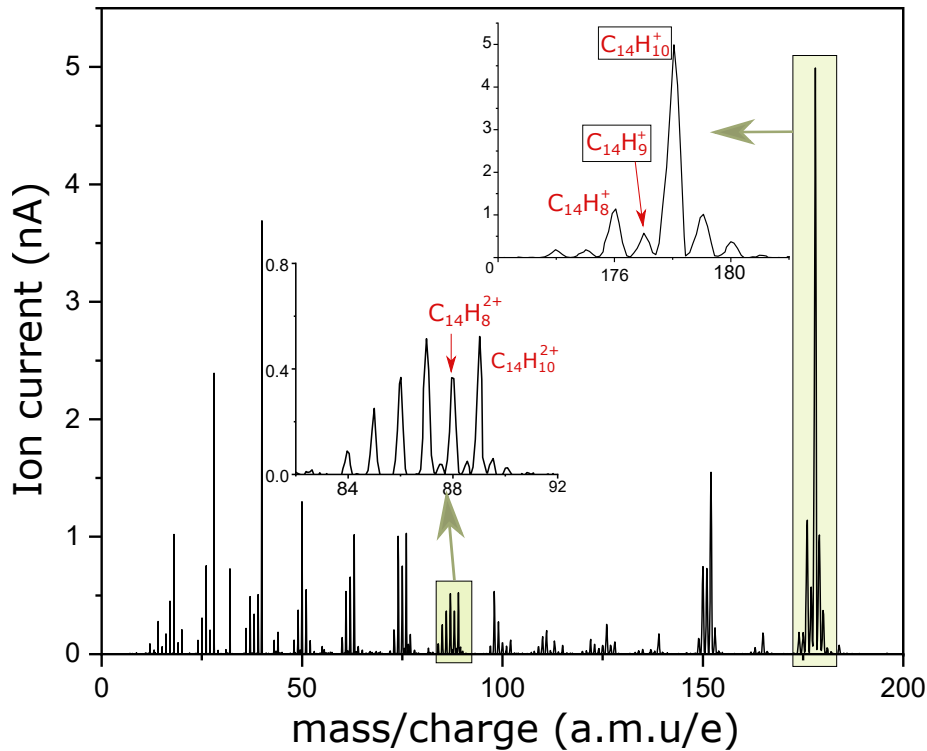
Figure 5.1: The primary ion mass spectrum depicting the ions that are investigated during the experiments. The zoom-in at the left shows the doubly ionized states of differently dehydrogenated phenanthrene, and the zoom-in at the right depicts the dehydrogenation states of the parent monocation. The primary ions marked with the box are discussed throughout this section, whereas others are discussed in Ref. [72].

In the interaction region, this primary ion beam absorbs the photons from the counter-propagating soft X-ray photon beam. The photon beam is obtained from the synchrotron radiation that is passed through a grating (400 lines/mm) and a slit before it enters the interaction region. During these experiments, the slits are

opened to one mm. The beam spot size thus obtained is 0.5×1 mm^2. The overlap of the photon beam with the primary ion beam is ensured during the experiments. While the knowledge of the beam overlap factor would allow obtaining the absolute absorption cross sections, this factor is not recorded due to time constraints but the qualitative comparisons of different processes are still valid. Therefore, only relative absorption cross sections are reported for these experiments.
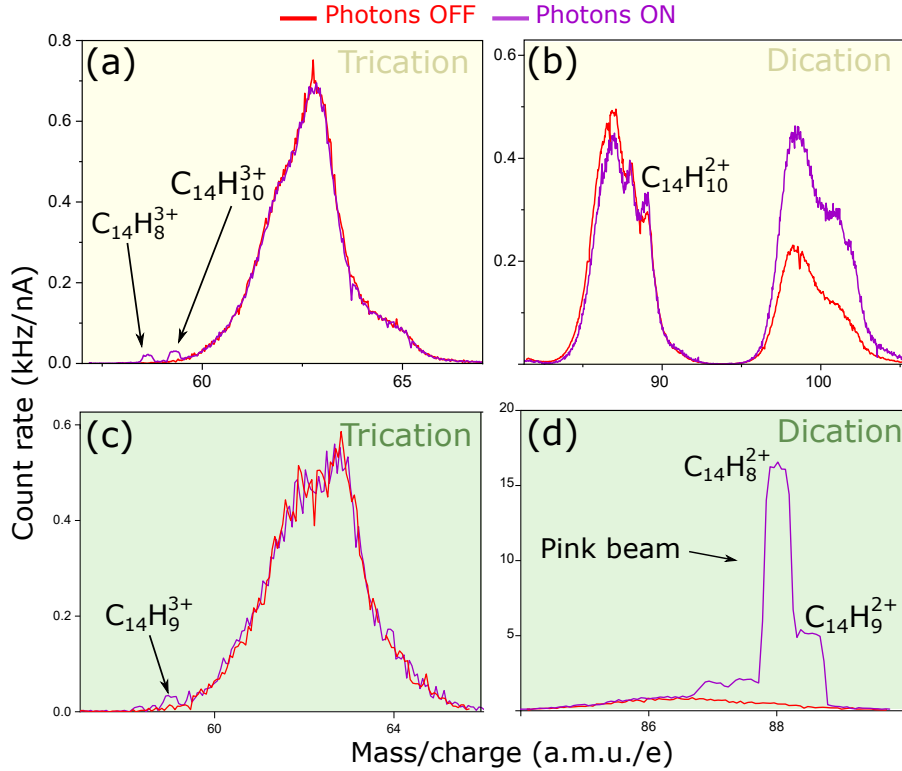
Figure 5.2: The upper and lower graphs show the product ions obtained for the primary ions $C_{14}H_{10}^+$ and $C_{14}H_9^+$ in yellow-shaded and the green-shaded region, respectively. The product ion mass spectrum is obtained with photons-off (red) and photons-on (violet) conditions. (a) and (c) depict the m/z regions where the trications are observed and (b) and (d) illustrates the m/z regions for the dication.

After the interaction of the two beams, the product ion signal is measured at the single particle detector. This signal is recorded in photons-off and photons-on conditions. The increase in the product ion signal in the photons-on condition shows the signatures of photon absorption. The two primary ions $C_{14}H_{10}^+$ and $C_{14}H_9^+$ are selected individually, and the effects of photon absorption are observed (shown in Figure 5.2). While performing the experiments in the photons-on conditions, the

beam was switched to the pink beam (polychromatic beam) mode, which consists of more photon flux (by a factor of 10) than in the monochromatic mode. As a consequence, the effect of the photon absorption becomes prominent as can be seen from Figure 5.2d.

The product ions for the primary ion $C_{14}H_{10}^+$ are represented by the yellow-shaded region in Figure 5.2a and 5.2b. As highlighted in the figure, the product ions investigated are $C_{14}H_8^{3+}$, $C_{14}H_{10}^{3+}$, and $C_{14}H_{10}^{2+}$. In addition, for the primary ion $C_{14}H_9^+$, the product ions $C_{14}H_{10}^+$, $C_{14}H_{10}^+$, and $C_{14}H_{10}^+$ are investigated. Therefore, the relative absorption cross sections are obtained for the following processes:

$$C_{14}H_{10}^+ + h\nu \rightarrow C_{14}H_{10}^{2+} + e^- \tag{5.1}$$

$$C_{14}H_{10}^+ + h\nu \rightarrow C_{14}H_{10}^{3+} + 2e^- \tag{5.2}$$

$$C_{14}H_{10}^+ + h\nu \rightarrow C_{14}H_8^{3+} + 2H + 2e^- \tag{5.3}$$

$$C_{14}H_9^+ + h\nu \rightarrow C_{14}H_9^{2+} + e^- \tag{5.4}$$

$$C_{14}H_9^+ + h\nu \rightarrow C_{14}H_8^{2+} + H + e^- \tag{5.5}$$

$$C_{14}H_9^+ + h\nu \rightarrow C_{14}H_9^{3+} + 2e^- \tag{5.6}$$
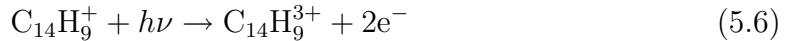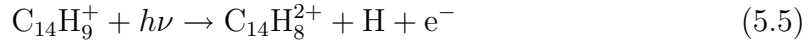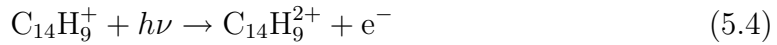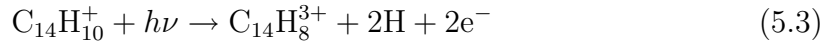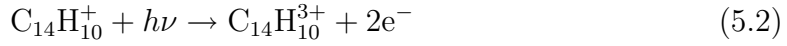
5.3 Electronic structure of cationic phenanthrene and its dehydrogenated state

The processes mentioned above are broadly classified as single (SI) and double ionization (DI) processes. In the SI processes, the single ionized state of the primary ion is m/z-selected as the product ion. In this process, one electron is ejected that can be thought of as an Auger-Meitner electron (Equations 5.1, 5.4, and 5.5). Whereas in the DI processes, the double ionized state of the primary ion is observed, where both the Auger-Meitner electron and the core electron are ejected (Equations 5.2, 5.3, and 5.6).
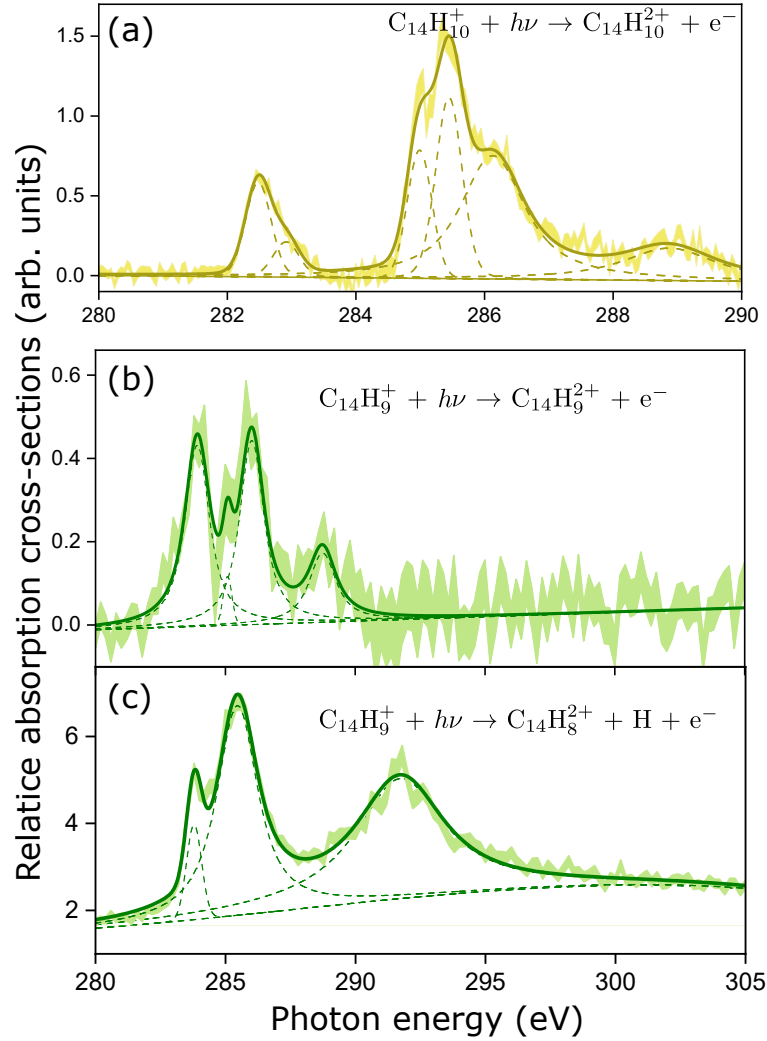
Figure 5.3: The relative absorption cross sections *vs.* the incident photon energies for the primary ions $C_{14}H_{10}^+$ and $C_{14}H_9^+$ are shown for the respective SI processes that are written within each panel. (a) The photochemical process for the $C_{14}H_{10}^+$ primary ion. The yellow-shaded curve is the experimentally obtained curve (the width of the curve indicates the error in the absorption cross section measurements). The yellow solid line represents the fitted curve, where the components of the fitted curve indicating different transitions are plotted with the dash-type yellow lines. (b) and (c) Similarly, the experimental curve for $C_{14}H_9^+$ ion is shown by the green-shaded region, and the fitted curve is shown by the green-colored curve, and the dash-type lines represent the fitting components. Two product ions are investigated, namely the $C_{14}H_9^{2+}$ (in (b)) and $C_{14}H_8^{2+}$ (in (c)).

In the SI processes, transitions from the carbon K-edge to an unoccupied molecular orbital (UMO) are observed. Figure 5.3 shows the experimentally obtained NEXAFS spectra for the primary ions $C_{14}H_{10}^+$ (Equation 5.1) and $C_{14}H_9^+$ (Equations 5.4 and 5.5). These experimental curves are corrected for the Doppler shift, monochromator energy shift, and the background signal (present due to residual gas or collisions inside the interaction region) as explained in Section 3.1. The experimental curve of the $C_{14}H_{10}^+$ ion is depicted with the yellow-shaded curve where the width of the curve represents the error in the experimental absorption cross section measurements. Similarly, the experimental curves obtained for the $C_{14}H_9^+$ ion are represented by the green-shaded region with the width representing the errors.

The experimental spectrum for the ion $C_{14}H_{10}^+$ (Equation 5.1) is fit with six Voigt peaks using the fitting procedure [87] explained in Section 4.1. The yellow solid line in Figure 5.3a represents the sum of all these six peaks, which is the final fitted curve, and the dash-type lines depict the individual Voigt peaks. For the primary ion $C_{14}H_9^+$, two channels 5.4 and 5.5 are investigated, one involving the pure single ionization process (process 5.4) and the other involving single ionization with dehydrogenation (process 5.5). The process without the hydrogen loss is fitted with four Voigt peaks (see Figure 5.3b), whereas the process with the hydrogen loss is fitted with three Voigt peaks (see Figure 5.3c). The corresponding values of the fitted peak positions are tabulated in the first column of Table 5.1, and the uncertainty in the photon energy is obtained to be in the range from 50 to 200 meV.

$C_{14}H_{10}^{2+}$	$C_{14}H_{10}^{3+}$	$C_{14}H_{8}^{3+}$
282.48 ± 0.01	282.53 ± 0.05	282.62 ± 0.06
282.91 ± 0.04	-	-
284.99 ± 0.03	-	-
285.45 ± 0.02	285.54 ± 0.07	285.33 ± 0.04
286.13 ± 0.04	-	286.18 ± 0.07
288.87 ± 0.08	-	-
-	295.18 ± 0.03	295.22 ± 0.02

Table 5.1: The peak energy values obtained *via* fitting the three channels of the primary ion $C_{14}H_{10}^+$, namely Equations 5.1, 5.3, and 5.2. The first six peaks depict the transition from the carbon $1s$ orbital to the UMOs, whereas the last row depicts the transition to continuum and is fit using the $\tanh(E)$ function.
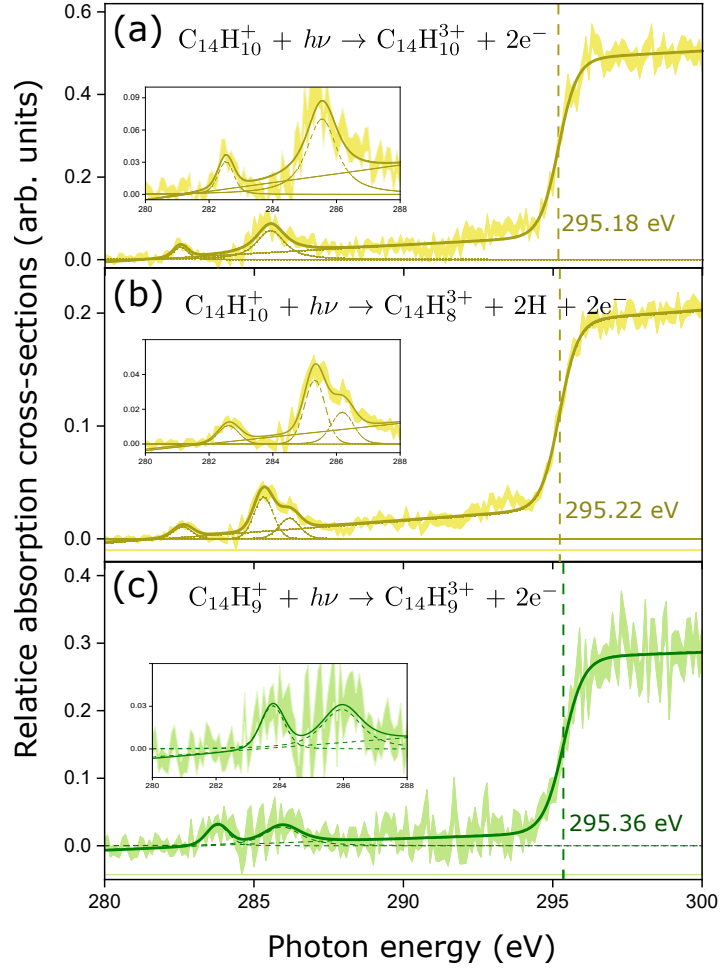
Figure 5.4: The relative absorption cross sections *vs.* the incident photon energy values for the primary ions $C_{14}H_{10}^+$ and $C_{14}H_9^+$ are shown for the DI processes. (a) and (b) The graph depicts the photoreaction processes for the $C_{14}H_{10}^+$ primary ion. The yellow-shaded curve is the experimentally obtained curve (the width of the curve indicates the error in the absorption cross section measurements). The yellow solid line represents the fitted curve, where the components of the fitted curve indicating different transitions are plotted with the dash-type yellow lines.(c) Similarly, the experimental curve for $C_{14}H_9^+$ ion is shown by the green-shaded region, and the final fitted curve is shown by the green-colored curve, and the dash-type lines represent the individual peaks obtained through the Voigt fitting.

For the DI processes, in addition to the transitions to the UMOs, the transition to continuum is also observed as can be seen in Figure 5.4 by the step-up feature. These

67

features are fitted with the Voigt and $\tanh(E)$ functions, where E is the photon energy. The transition to continuum can be readily assigned for the processes given in Equations 5.2, 5.3, and 5.6. The corresponding values of the fitted peak position are tabulated in the second and third column of Table 5.1 for the primary ion $C_{14}H_{10}^{+}$, and in the third column of Table 5.2 for the primary ion $C_{14}H_9^{+}$. The shift in the ionization value of the primary ions can be seen as a result of dehydrogenation from 295.18 eV (for $C_{14}H_{10}^{+}$) to 295.36 eV (for $C_{14}H_9^{+}$). This leads to a shift of 180 meV, which is within the uncertainty of the photon energy value.

From Tables 5.1 and 5.2, it can be observed that the fitted peak positions for the DI processes are overlapping with the SI processes before continuum (last row of Table 5.1). To assign and understand the transitions that are observed in the experimental curves, the quantum-chemical calculations are performed using the time-dependent density functional theory by employing the B3LYP/def2-TZVPP method. As mentioned in Section 2.1, the final theoretical spectra are calculated by vibrational averaging the X-ray absorption spectra of displaced structures that represent a thermal ensemble. While performing the vibrational averaging, the temperature is approximated to 800 K for calculations.

$C_{14}H_9^{2+}$	$C_{14}H_9^{2+}$	$C_{14}H_9^{3+}$
283.87 ± 0.001	283.79 ± 0.02	283.78 ± 0.10
285.10 ± 0.11	285.45 ± 0.02	285.95 ± 0.19
286 ± 0.03	-	-
288.75 ± 0.07	-	-
-	291.66 ± 0.06	-
-	-	295.36 ± 0.05

Table 5.2: The peak energy values obtained *via* fitting the three channels of the primary ion $C_{14}H_9^{+}$, namely Equations 5.4, 5.5, and 5.6. The first five rows depict the transitions from the carbon $1s$ orbital to the UMOs, whereas the last row depicts the transition to continuum and is fit using the $\tanh(E)$ function.

The theoretically obtained spectra are shown in Figure 5.5 and 5.7 for the primary ions $C_{14}H_{10}^{+}$ and $C_{14}H_9^{+}$, respectively. All these spectra are shifted by $+11.9$ eV on the energy axis, due to approximations and assumptions used in the quantum-chemical calculations. The peaks observed in the spectra show the absorption cross section of a transition from the C $1s$ orbital to the UMOs. The theoretical spectra provide details about the transition to the specific orbitals. Depending upon the final occupied state, the theoretically obtained spectra could be disentangled for

individual transitions as illustrated in Figures 5.5 and 5.7. The theoretical spectrum is independent of the product ions because these are not known from the calculations. The electronic transitions are assigned for the individual primary ions with the help of the experimental and theoretical results as described as follows.
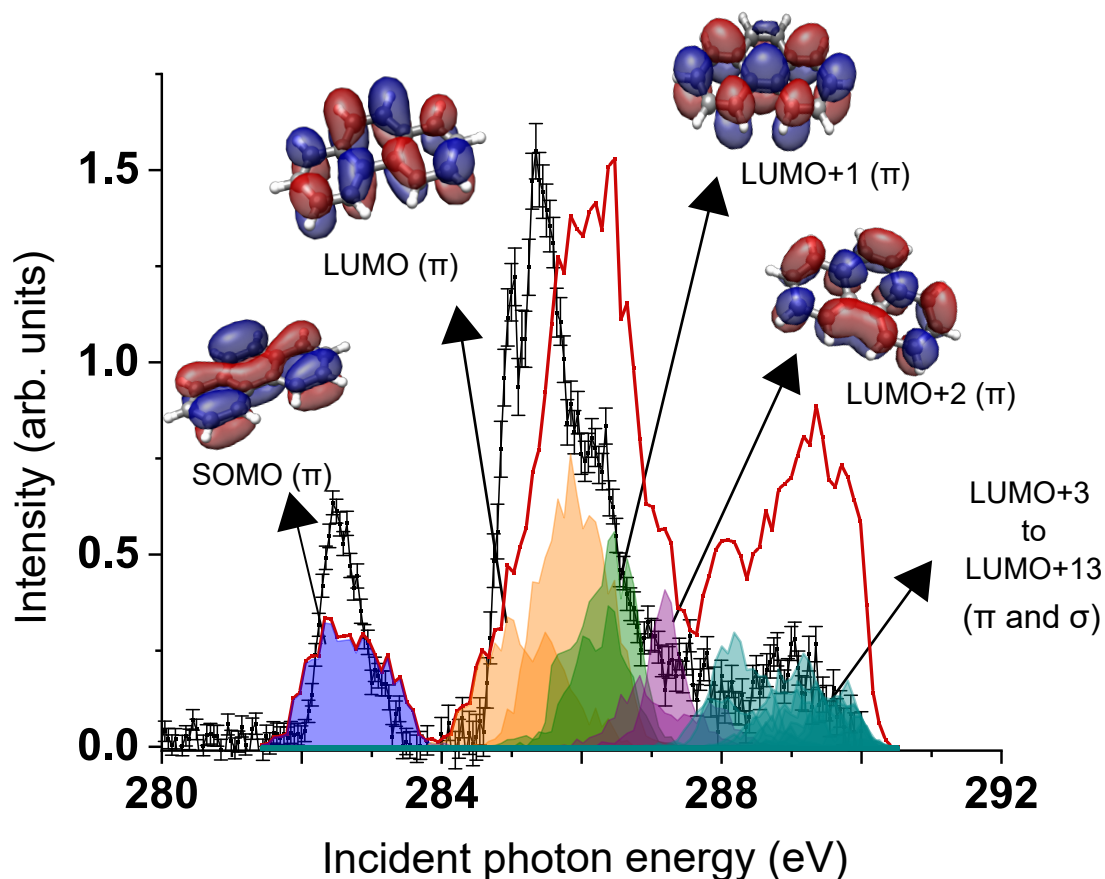
Figure 5.5: The black curve shows the experimental curve for the doublet electronic state of the phenanthrene monocation $C_{14}H_{10}^+$. These peaks represent the transition from the carbon $1s$ orbital to the UMOs. The theoretical spectrum is given by the red solid line. The contribution of the individual MOs to the final theoretical spectrum is depicted *via* differently colored shaded peaks, and the corresponding MOs are plotted. The overlapping of the final states increases with increasing orbital energy, which makes the spectrum difficult to disentangle with respect to different orbital contributions for the incident photon energies above 287.5 eV.

For the primary ion $C_{14}H_{10}^+$, the experimentally obtained spectrum is shown with the black curve in Figure 5.5. The theoretical final averaged spectrum (as explained

in Section 2.1.3) is shown with the red solid line. The transitions from the $1s$ orbital to the SOMO could be unraveled, as illustrated by the blue shaded region and can be attributed to the first peak of the experimental NEXAFS spectrum. The SOMO consists of conjugated π orbitals. Similarly, other final MOs are provided in Figure 5.5 together with the peaks to which they are attributed with their character written within parentheses. The second peak has contributions from transitions to the lowest unoccupied molecular orbital (LUMO) (π-bonding orbital) and LUMO+1 (π-bonding orbital). The further assignment of the spectrum gets more involved as the final states are closer to each other and thus portray overlapping regions before the continuum.

For the primary ion $C_{14}H_9^+$, two product ions, $C_{14}H_9^{2+}$ (process 5.4) and $C_{14}H_8^{2+}$ (process 5.5), in the SI processes are investigated. The experimentally obtained NEXAFS spectra are given in Figure 5.7 with black and green curves for $C_{14}H_9^{2+}$ and $C_{14}H_8^{2+}$, respectively. The vibrationally averaged spectrum is given as a red solid line. The peaks correspond to the contribution from both the singlet and triplet electronic states of five structural isomers of the $C_{14}H_9^+$ ion (see Figure 5.6).
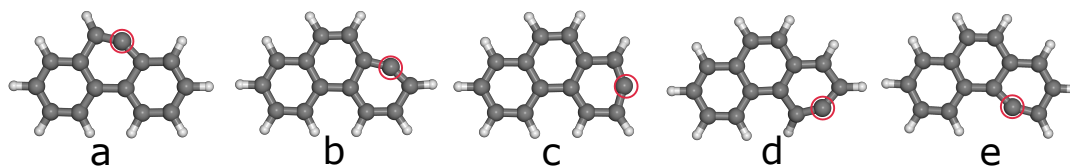
Figure 5.6: Structural isomers of the $C_{14}H_9^+$ ion, which are formed by removing hydrogen from five unique positions of $C_{14}H_{10}^+$ ion, represented with a, b, c, d, and e.

The shaded regions are the contributions of transitions to various MOs. The first peak is attributed to the mixed transition from C $1s$ to the LUMO (σ) of the singlet electronic state and the SOMO (π) of the triplet electronic state. The second peak is the contribution of the transition of the core electron to LUMO+1 and LUMO+2 from the C $1s$ orbital. The third peak can be attributed to the transitions to LUMO+4 to LUMO+13. The MOs illustrate the combination of π and σ character. The contributions from transitions to LUMO+14 to LUMO+44 are overlapping with each other, which provides a diffuse broad spectrum. The contribution by further MOs become lesser than LUMO+44, and thus was not calculated further.

5.4 Discussions

The peaks observed in the DI processes 5.2 and 5.3 can also be assigned with the help of the known transitions from the SI processes. In addition to transitions to the

UMOs, the transition to continuum is observed. All the transitions for $C_{14}H_{10}^+$ and $C_{14}H_9^+$ are summarized in the left and right panel of Figure 5.8, respectively.
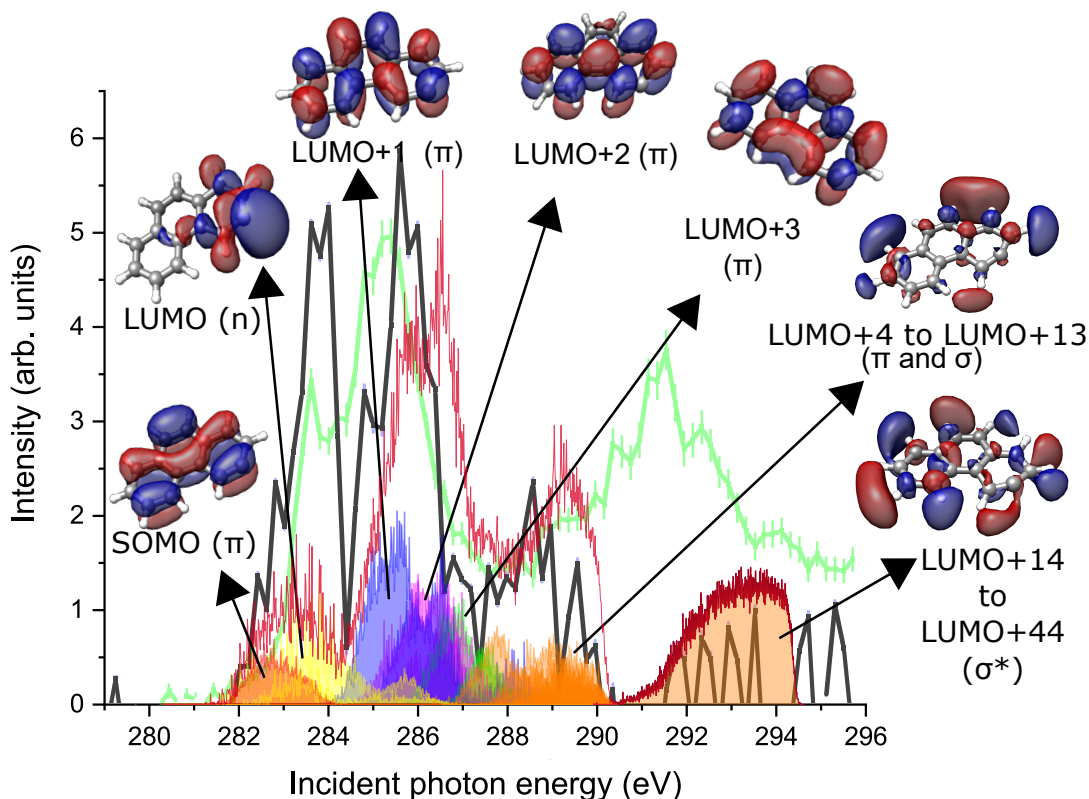
Figure 5.7: The black curve shows the experimental curve for the primary ion $C_{14}H_9^+$, which leads to the formation of the product ion $C_{14}H_9^{2+}$. The intensity is scaled by a factor of 12 for a clear comparison with the green curve that demonstrates the formation of the product ion $C_{14}H_8^{2+}$, that is, depicting a hydrogen loss channel. The theoretical spectrum is given as a red solid line. The contribution of individual MOs to the final theoretical spectrum is depicted *via* differently colored shaded peaks. The third peak attributed to the combined contribution from LUMO+4 to LUMO+13 is represented by LUMO+10 plot, illustrating both π and σ characters. Likewise, for the fifth peak, the MO characterized by σ^* CH bond is illustrated using LUMO+17. The corresponding MOs are provided for only one randomly chosen 'd' isomer of the primary ion $C_{14}H_9^+$ for clarity purposes. The orbitals are characterized by their main (anti-) bonding type, namely π, π^*, σ, or σ^*.

Collectively, the SOMO-LUMO gap can be approximated to ~ 2.5 eV for the phenanthrene monocation, which is estimated by averaging the respective two peak

71

positions of the transitions to the SOMO and LUMO. The SOMO-LUMO gap in the phenanthrene monocation can be approximately compared to the first peak of the fluorescence spectrum of phenanthrene that leaves a hole in the HOMO *via* a transition to the LUMO. This energy gap from HOMO to LUMO is similar to the SOMO-LUMO gap of the phenanthrene monocation, where the monocation is formed *via* removing the electron from the HOMO, making it a SOMO, and then X-ray photons excite the C1s electrons to the SOMO and the LUMO providing information on the SOMO-LUMO gap. The fluorescence spectrum of phenanthrene is obtained in Ref. [113], where the first peak corresponds to an energy value of 25500 cm^{-1}, that is, ~ 3.1 eV. This is in agreement with the estimated value obtained from this NEXAFS spectrum.
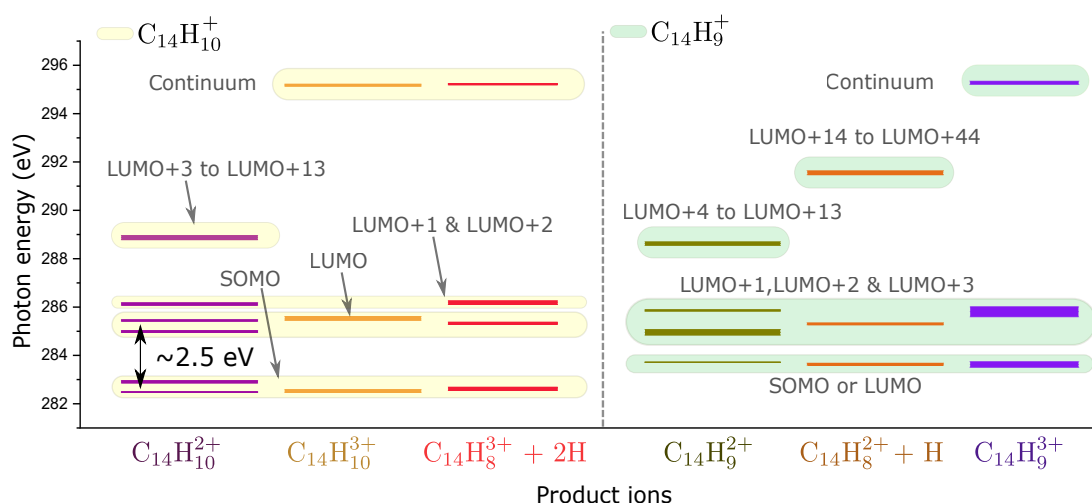
Figure 5.8: The peak positions of the observed transitions observed in the experimental curves are depicted by the horizontal bars. These are assigned with the help of theoretical calculations, as illustrated in Figure 5.5 and 5.7 and the final states of the transitions are labeled here for all the product ions observed for the primary ions $C_{14}H_{10}^{+}$ (shaded in yellow) and $C_{14}H_{9}^{+}$.

For the primary ion $C_{14}H_{9}^{+}$, the peak at 288.7 eV corresponding to pure single ionization channel (Equation 5.4) could be attributed to the transition to LUMO+4 to LUMO+13 of π character. The peak at 291.6 eV in the process involving hydrogen loss (Equation 5.5) is attributed to the transition from C 1s to LUMO+14 to LUMO+44. All the MOs ranging from LUMO+14 to LUMO+44 have σ^{*} CH character as can be seen in Figure 5.7 (plotted for LUMO+17), which is indicative of the breakage of the C-H bond. Thus the last peak position in the green experimental curves is assigned to the energy needed for C-H bond breaking.

5.5   Summary and future outlook

The NEXAFS spectra are obtained for the two primary ions, $C_{14}H_{10}^+$ and $C_{14}H_9^+$. Due to the presence of active vibrational modes, there is a spread in the peaks. Therefore, the transitions from the carbon $1s$ orbitals to the UMOs could not be resolved for individual transitions to UMO specifically at higher energy values.

However, the grouped contributions from various molecular orbitals of a certain bonding character (π, σ, σ^*) can be evaluated, and the results are summarized in Figure 5.8. The figure represents the electronic structure of $C_{14}H_{10}^+$ for various investigated product ions ($C_{14}H_{10}^{2+}$, $C_{14}H_{10}^{3+}$, $C_{14}H_8^{3+}$), which are formed as a result of X-ray photon interaction. The yellow shaded horizontal regions represent similar transitions, e.g, the purple, mustard, and red lines in the yellow shaded region at $\sim$283 eV depict the transition from C $1s$ to SOMO for the corresponding product ions.

For $C_{14}H_{10}^+$, the SOMO-LUMO gap can be observed to be $\sim$2.5 eV. Due to single hydrogen loss from $C_{14}H_{10}^+$, the SOMO-LUMO gap is observed to be reduced, as can be seen from green shaded region representing $C_{14}H_9^+$ ion. The lowest horizontal bars are observed to be at $\sim$284 eV, which were noticed to be at 283 eV for $C_{14}H_{10}^+$. Thus, a $\sim$1 eV reduction in the SOMO-LUMO gap as a result of dehydrogenation can be qualitatively reported.

Since ECRIS is employed as the primary ion beam source, the molecules cannot be considered in their ground vibronic states only, and we see contributions from their vibrational motions as well. This also leads to the fact that the isomerization of the ions cannot be neglected even if the ions cool down while travelling down to the interaction region. For this reason, the NEXAFS spectra of the anthracene monocation, a structural isomer of phenanthrene, are obtained *via* TD-DFT calculations. A comparison of the theoretical spectra of the anthracene and phenanthrene monocation with the experimentally recorded spectra is shown in Figure 5.9. The calculated spectra for the phenanthrene and the anthracene monocation are different enough to exclude the possibility of isomerization of cationic phenanthrene into cationic anthracene.

Besides this demerit of this technique to not completely distinguish between structural isomers, it offers the great benefit of m/z selecting the primary ions and the product ions, which enabled us to investigate the photon energy at which the dissociation of the C-H bond could be happening, that is the peak at 291.6 eV in Equation 5.5. The HOMO-LUMO gap of phenanthrene could also be estimated to be around $\sim$ 2.5 eV, which is observed to be reduced as a result of dehydrogenation.
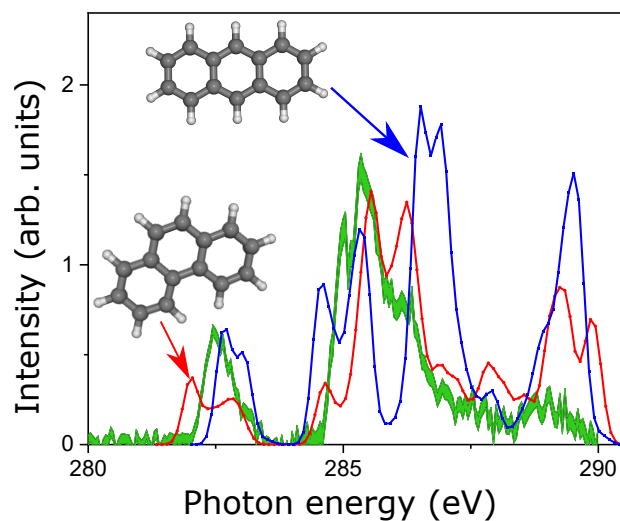
Figure 5.9: The green curve represents the experimentally obtained NEXAFS spectra of m/z equivalent to the phenanthrene monocation. The red curve shows the spectrum calculated for the doublet electronic state of the phenanthrene monocation using TD-DFT with B3LYP/def2-TZVPP method. Similarly, the XAS spectrum is also calculated for a structural isomer of phenanthrene monocation, that is, anthracene monocation.

To support future experiments, the folding of cationic phenanthrene as a result of dehydrogenation was observed. To investigate the folding of the planar molecule, dihedral angles of the different isomers of the $C_{14}H_9^+$ are observed such that the position of the hydrogen loss is included. If it would still be a planar molecule then the dihedral angle should be 0°or 180°. The upper estimate of this dihedral angle for all the isomers considered in this work is found to be 22°. Thus, it can be inferred that the molecules are not planar but this does not seem to be a strong clue for the presence of a curving feature. However, a higher degree of dehydrogenation of a large PAH could be expected to lead to prominent curving that can be a precursor to the formation of buckminsterfullerene that is observed in the interstellar medium as proposed in Ref. [21].

Chapter 6

Fragmentation dynamics of fluorene explored using time-resolved pump-probe spectroscopy

6.1 Introduction

Polycyclic aromatic hydrocarbons (PAHs) play an active role in the rich photophysics and photochemistry of interstellar medium (ISM). The harsh radiation present in ISM can initiate processes such as ionization, fragmentation, and isomerization of PAHs. We investigate the interaction of the prototypical PAH, fluorene with XUV radiation and intense near-IR radiation. The fluorene molecule, even though highly stable with the extended π electron system, is subjected to fragmentation and ionization to multiply charged states. Post-interaction species are in their highly excited vibronic states, and beyond Born-Oppenheimer condition prevail (see Ref. [27, 28]). Elucidating the non-radiative processes add to the fundamental insight into the femtochemistry of fluorene molecules.

The time-resolved femtosecond pump-probe spectroscopy along with the time-of-flight mass spectrometry (TOF-MS) and velocity-map imaging (VMI) methods as observational methods are employed during the experiments. The double-sided VMI spectrometer set up at the CFEL-ASG Multi-Purpose instrument (CAMP) endstation at the Free-electron LASer in Hamburg (FLASH) is used (described in Section 3.2). Two sets of pump-probe experiments are performed where we used two different femtosecond excitation pulses, namely, extreme ultraviolet (XUV) pulse (40.9 eV photon energy) and an infrared (IR) pulse (1.53 eV photon energy) from the FEL and optical Ti-Sa table-top laser, respectively. The visible (Vis) pulse (3.06

eV photon energy) is used to probe the processes begun by pump pulses. The probe pulse is chosen to be weak enough to only induce single ionization. Using two different types of excitation pulses can be thought to excite different ensemble and initiate different dynamics that are explored with a thorough analytical procedure. In the first section, results from the time-resolved XUV-Vis pump-probe spectroscopy are illustrated. In the second section, the stability of the fluorene under intense IR radiation is addressed using Vis probe pulses.

6.2 XUV-Vis pump-probe spectroscopy *

6.2.1 Introduction

The interaction of the astrochemically-relevant PAH fluorene with the harsh radiation in ISM is explored. We report on the use of XUV (XUV, 30.3 nm) radiation from the FLASH, corresponding to He II emission line and visible (Vis, 405 nm) photons from an optical laser to investigate the relaxation and fragmentation dynamics of fluorene ions. The ultrashort laser pulses allow to resolve the molecular processes occurring on femtosecond timescales. Our experiments track the ionization and dissociative ionization products of fluorene through time-of-flight mass spectrometry and velocity-map imaging. Multiple processes involved in the formation of each of the fragment ions are disentangled through analysis of the ion images. The relaxation lifetimes of the excited fluorene monocation and dication obtained through the fragment formation channels are reported to be in the range of a few tens of femtoseconds to a few picoseconds.

6.2.2 Experimental Conditions

The experiments were performed using the CFEL-ASG Multi Purpose (CAMP) endstation [74] at the beamline BL1 at the FLASH I branch with a double-sided velocity-map-imaging (VMI) spectrometer installed at the CAMP endstation. The experimental method is described in Section 3.2. For this experiment, we used two pulsed excitation beams (XUV and Vis), operated at a repetition rate of 10 Hz. The XUV pulses ($\lambda = 30.3$ nm, pulse duration 80 to 90 fs (FWHM), which is estimated from the pulse length of electrons [114] using the "LOLA instrument" [77]) were provided by FLASH1 with an average pulse energy of 14.5 μJ, which was then reduced

---

*This chapter is adapted from Ref. [29]. During the preparation of this manuscript, holes in the ion image were observed as shown in Figure 5A of the article, which were attributed to a defect in the detector. However, later in the course of preparing this thesis chapter, it was found that two of these holes were because of artifacts in the analysis scripts. These artifacts were minor and do not change any major result. This section shares an updated version of the quantitative information.

to 1.4 μJ by two aluminium filters of thickness 100.9 nm (55% transmission) and 423.4 nm (28% transmission), and the five beamline mirrors (resultant transmission 62%). The second harmonic generation output of a Ti:Sa optical laser, obtained using one beta-barium borate (BBO) crystal, was used as the Vis laser pulse ($\lambda = 405$ nm, pulse duration less than $\sim$150 fs, which is estimated from the fundamental beam (810 nm) pulse duration) with a pulse energy up to $\sim$390 μJ [80].

6.2.3 Analysis

The general analysis procedure is introduced in Section 4.2. Here, some detailed information is given. The 2D ion velocity-map images captured from the PImMS camera were fully symmetrized (top/bottom/left/right) and then Abel-inverted to obtain the central slices of the 3D product ion velocity distributions, using the onion peeling method implemented in the PyAbel package available in Python [100, 105]. Angular integration of these Abel-inverted velocity-map ion images generated the radial distribution (in pixels), which was converted to ion momentum using a calibration factor determined through SIMION ion trajectory simulations [115]. The momentum distributions were analyzed as a function of delay time, and the resulting pump-probe delay-time dependent ion yields were fitted using in-house developed open source libraries and scripts [103, 106, 116]. The fitting procedure is explained in detail in references [104, 107]. The analysis routine is described in Section 4.2.

The temporal overlap of the two laser pulses (t_0) was extracted after simultaneously fitting 17 different pump-probe delay time-dependent ion yield curves, recorded in the same experimental event, having the same parameter t_0. The resulting t_0 with an error of 1 fs was then used as a constraint parameter to fit time-dependent ion yields of other fragments, which were fitted with multiple transient features as discussed below for the fragment $C_4H_x^+$. Subscript 'x' depicts the number of hydrogen atoms attached to the fragments (ranges from 1 to 10). The time delay between the pump and the probe pulse (Δt) was corrected for the temporal overlap offset between the two pulses and for jitter in the XUV pulse arrival time that was measured by the bunch arrvial time monitor (BAM) [81, 82]. The ion yield intensity was also corrected for shot-to-shot FEL pulse energy fluctuations that are described briefly in Section 8.2.5 of the Appendix. Covariance analysis [117] was performed on both TOF and VMI results. The TOF measurements enabled us to calculate TOF-TOF partial covariance. The method is explained in detail in reference [108], and the results are shared in Section 8.2.3 of the Appendix. The two-body recoil-frame covariance could be calculated from the VMI data, which are discussed in the results section. The results are classified as time-independent and time-resolved results.

6.2.4 Time-independent results

6.2.4.1 Ionization and fragmentation of fluorene

Mass spectra obtained after the interaction of fluorene (FLU) with XUV (mass spectrum in red) and Vis (mass spectrum in blue) radiation are shown in Figure 6.1(a). In the following section, we first discuss the effect of Vis and XUV photons on FLU separately before we evaluate their combined effects.
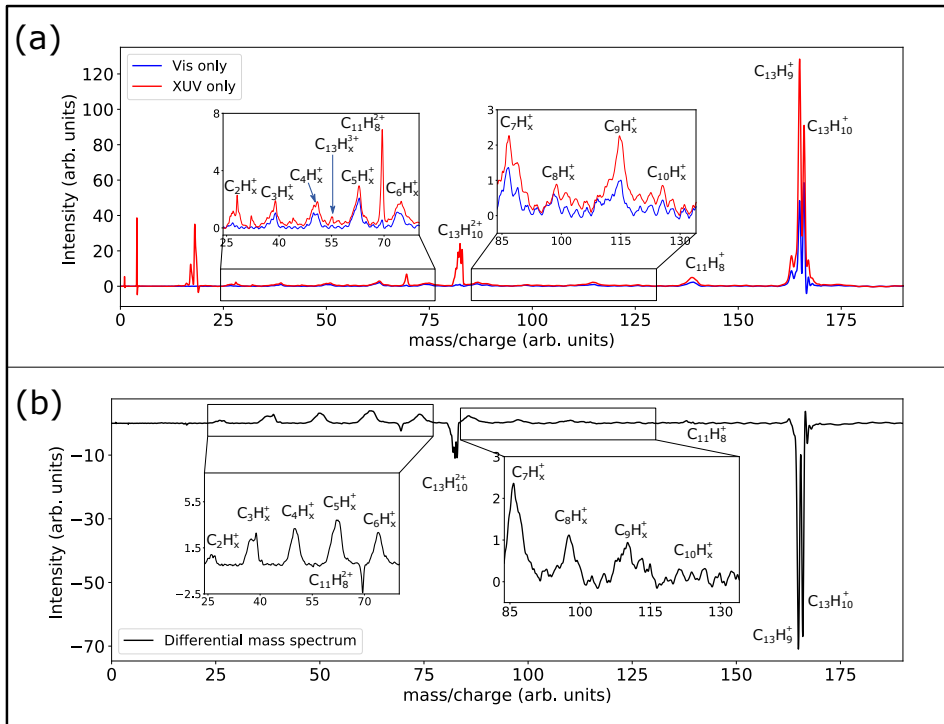
Figure 6.1: a) Mass spectra for two different conditions: XUV only (red) and Vis only (blue), which were measured using the MCP detector. The insets are the zoomed views of less intense fragments. b) Differential mass spectrum calculated by subtracting the individual XUV only and Vis only spectra from the pump-probe delay-time averaged XUV-Vis mass spectrum in order to visualize the effect of the XUV and Vis pulses.

When FLU absorbs Vis photons, mostly single ionization (ionization potential of FLU: 7.88 ± 0.05 eV [118]) with loss of up to three hydrogen atoms (hydrogen dissociation energy of FLU: ~ 4 eV [28, 119]) and one acetylene unit (forming $C_{11}H_x^+$) is observed. The single hydrogen atom loss from FLU^+ is found to be the second most

intense peak, FLU^+ being the most intense one. As the energy required for ionization and dissociative ionization is more than the single Vis photon energy (3.1 eV), multi-photon processes must be involved [28]. Consequently, several fragmentation channels are also accessible.

The absorption of XUV photons by FLU leads to single, double, and triple ionization. The singly and doubly charged FLU ions show loss of up to three and four hydrogen atoms, respectively. In the mass spectrum, the intensity of the fluorenyl cation $C_{13}H_9^+$ is observed to be higher than the intensity of $C_{13}H_{10}^+$. The major contribution of $C_{13}H_9^+$ to the mass spectrum can be attributed to the conversion of an sp^3 hybridized carbon to an sp^2 hybridized carbon after the loss of one of the two aliphatic hydrogen atoms, which makes the molecule a fully conjugated system. Since a single XUV photon has enough energy to cause ionization and/or hydrogen dissociation, the production of the fluorenyl cation is observed to be more intense during XUV interaction than in the case of Vis pulse interaction that needs multiple photons to produce the fluorenyl cation. A lower abundance of the fluorenyl cation intensity than the monocationic fluorene is consistent to the observation in other studies with rather low $\sim$4.1 eV photon energy [120] and proton impact studies [121]. Acetylene loss from the parent monocation forming $C_{11}H_x^+$ and from the parent dication forming $C_{11}H_x^{2+}$ is also observed. The relative abundance of $C_{11}H_x^{2+}$ w.r.t $C_{13}H_x^{2+}$ is higher than that of $C_{11}H_x^+$ w.r.t $C_{13}H_x^+$, which points towards a facilitated acetylene loss from the parent dication than from the parent monocation. The possible dissociation pathways leading to the formation of $C_{11}H_x^+$ and $C_{11}H_x^{2+}$ and the energies involved in dissociation of the parent mono- and dication are summarized in Section 8.2.4 of the Appendix.

A more prominent $C_2H_x^+$ peak is observed in the XUV-only case compared to the Vis-only condition. During interaction with XUV photons, both the parent monocation and the dication can dissociate to produce $C_2H_x^+$. For the parent monocation, both the formation of the charged acetylene unit, $C_2H_x^+$ (together with the neutral partners, e.g. $C_{11}H_y$, where the subscript 'y' depicts the number of hydrogen atoms in this partner fragment) and formation of neutral C_2H_x (together with charged partners, e.g. $C_{11}H_x^+$) are feasible. The parent monocation dissociation will be reflected in the low momentum region, i.e., region I in Figure 6.2, since during the dissociation of the parent monocation, the charged fragments are recoiling from neutral fragments, whereas the parent dication produces $C_2H_x^+$ partnered by charged $C_{11}H_y^+$ resulting in higher momentum and appear in region II in Figure 6.2. The co-production of these two fragment ions is indicated by the similar momentum profiles in region II, which is confirmed by recoil-frame covariance (shown in Figure 6.3). Only a low amount of $C_2H_x^+$ is formed from FLU^+, while significant amounts are formed from the FLU^{2+}.

The differential mass spectrum is calculated by subtracting the individual ion yields observed in the XUV only and the Vis only condition from the XUV-Vis

pump-probe delay-time averaged mass spectrum (shown in black in Figure 6.1(b)). The positive and negative intensity show the increase and decrease in the ion yield, respectively. The decrease in the ion yield of the large fragments or the parent ion species (for example for $C_{13}H_{10}^+$, $C_{13}H_{10}^{2+}$, and $C_{11}H_8^{2+}$) together with the substantial increase in the fragment intensity allude the dissociation of the large species into the smaller fragment ions as a result of the molecular beam interacting with both the XUV and Vis pulses.
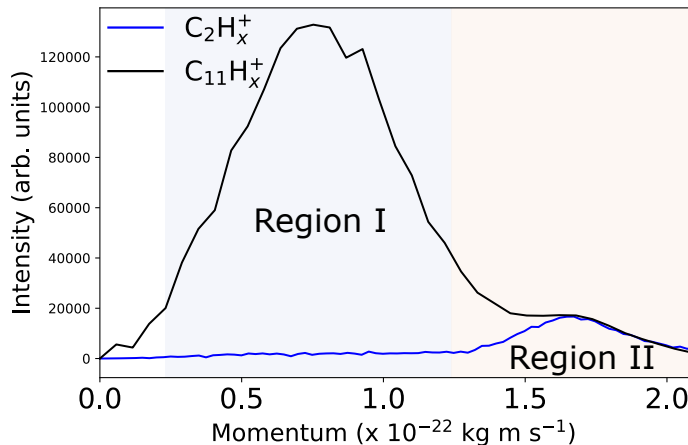
Figure 6.2: The momentum profiles of $C_2H_x^+$ (blue curve) and $C_{11}H_x^+$ (black curve) fragments are shown for the XUV-only condition and were acquired from the velocity-mapped ion images. Regions I and II mark ions with low and high momentum, respectively. The momentum matches for the two ions, indicating their co-production, which is confirmed by recoil-frame covariance.

6.2.4.2 Ion momenta and covariance of product fragment ions

Recoil-frame covariance analysis was performed on the multi-mass VMI data set to discern the correlated ions. The details of covariance mapping can be found in references [109–112]. Briefly, recoil-frame covariance shows the velocity distribution of one ion (ion of interest) with respect to the recoil velocity vector of another ion (reference ion). Figure 6.3 shows the covariances between all possible monocation pairs resulting from dissociation of FLU^{2+}. Generally, the intense spot directing opposite to the reference ion direction indicates that the two ions (the ion of interest and the reference ion) are created from the same parent molecule, in a simple two-body decay. Since recoil-frame covariance demonstrates the correlated motion of the two species, the blurred spots indicate that they are produced *via* a more complex mechanism along with other (neutral or charged) partners. It can be observed that $C_{11}H_x^+$ (green

square) is only produced together with an acetylene ion, but that the acetylene ion can be produced with other monocations (blue rectangle). The TOF-TOF partial covariance map provides information on only three of the fragmentation channels involving dissociation of FLU^{2+} into $C_2H_x^+$ (with $C_{11}H_y^+$), $C_3H_x^+$ (with $C_{10}H_y^+$), and $C_4H_x^+$ (with $C_9H_x^+$), shown in Section 8.2.3 of the Appendix.
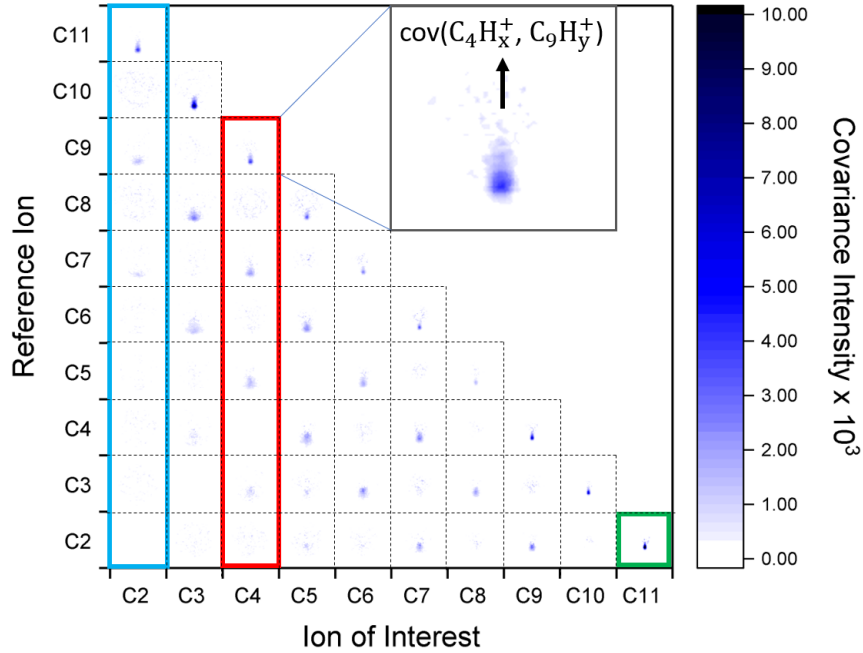
Figure 6.3: The two-body recoil frame covariance when a dication leads to fragmentation upon irradiation. Each square in the dotted grid represents a two-body recoil frame covariance map of the ion of interest with respect to the reference ion, for all the fragment ions, where the direction of the reference ion is vertically upward as also shown in the inset by the black arrow. Self-covariance of an ion with itself is omitted for clarity. Since FLU has thirteen carbon atoms, the sum of carbon atoms of the dissociation products cannot exceed thirteen, and therefore no covariance is expected in the upper half. As an example, the zoomed covariance signal of $C_4H_x^+$ with the reference ion $C_9H_y^+$ is displayed in the inset. The additional subscript 'y' depicts the number of hydrogen atoms attached to the fragment, which is the momentum partner of another fragment with the number of hydrogen atoms depicted with subscript 'x'. The blue rectangle depicts multiple possible ions with which $C_2H_x^+$ could be produced, similarly the red rectangle and green square highlight the possible partners of $C_4H_x^+$ and $C_{11}H_x^+$, respectively.

To summarize, the mass spectrum and the covariance analysis help us to identify a number of major fragmentation pathways of FLU molecules when subjected to Vis and XUV radiation. The time-dependent results are shown in the next section to understand the time evolution of the XUV-initiated dynamics in FLU molecules, probed using Vis photons.

6.2.5 Time-resolved results

6.2.5.1 Fragmentation channels and their relative intensities

We probed the dynamics and fragmentation pathways of fluorene initiated by the XUV photons at different delay times Δt using Vis photons. In the following, negative time delays ($\Delta t < 0$) denote Vis light irradiating the FLU molecules before the XUV pulse, and positive delays ($\Delta t > 0$) denote XUV pulses arriving earlier than Vis pulses, where the time at which the pulses coincide corresponds to $\Delta t = 0$. In the notation (i,j), 'i' indicates the charge state of the ion of interest, and 'j' depicts the charge state of the partner produced along with the ion of interest. The (1,0) channel would thus correspond to a monocation (ion of interest) recoiling against a neutral partner. Such products will have lower momentum than in the case of the (1,1) channel, where the monocation is recoiling against another monocation and experiences Coulomb repulsion, which is absent when recoiling against a neutral partner. We specify $C_2H_x^+$, $C_3H_x^+$, $C_4H_x^+$ as small fragments, $C_{10}H_x^+$ and $C_{11}H_x^+$ as large fragments, and the others are considered as medium fragments.

Figure 6.4(a) shows the delay-time averaged velocity-map ion images for two fragments $C_4H_x^+$ and $C_9H_y^+$. These images were processed to obtain the momentum distribution as a function of delay time shown in Figure 6.4(b), which can be divided into three channels: (1,0), (1,1), and (1,2) to depict low, medium, and high momentum regions, respectively. The signal intensity is then integrated over the momentum coordinate to generate pump-probe delay time-dependent ion yields in these distinct channels (green points in Figure 6.5(c) and 6.5D).

FLU undergoes single and double ionization upon interaction with XUV photons, the resulting parent monocation and the dication interact with the Vis probe pulse and dissociate into the (1,0) and (1,1) channels of the fragment ions, respectively. This dissociation is evident by a sudden decrease in signal for the parent ions accompanied by an increase in the intensity of fragment ions after $\Delta t = 0$. For small fragments, the (1,1) channel is observed to be the most dominant amongst the (1,0), (1,1) and (1,2) channels as shown in Figure 6.4(b) for $C_4H_x^+$. On the contrary, the medium-sized fragments are observed to be mostly produced through the (1,0) channel, shown in Figure 6.4(b) for $C_9H_y^+$. The preference of the (1,0) channel and (1,1) channel by medium and small-sized ions, respectively, is explained as follows.

82

(a) Velocity-mapped ion images (b) Momentum distribution versus pump-probe delay
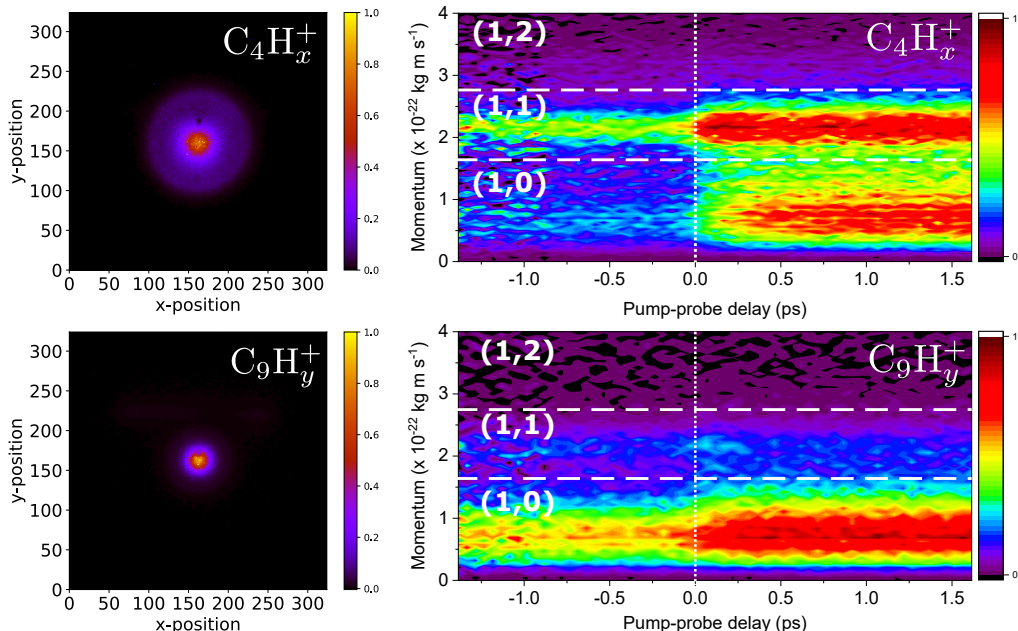
Figure 6.4: Results for two of the fragments, $C_4H_x^+$ and $C_9H_y^+$: a) 2D raw velocity-mapped ion images for the two fragments. The x and y axes denote the pixels of the PImMS camera (324×324). The black spots in the ion images are due to an artifact in the MCP detector. These images are later fully symmetrized and then Abel-inverted to obtain the central slice of the 3D velocity distribution. This central slice is angularly integrated, and the resultant momentum distribution is plotted as a function of delay time shown in (b). b) Momentum distribution as a function of pump-probe delay for two fragment ions showing momentum matching in the (1,1) channel, indicating their co-production in the same fragmentation reaction, which is verified by the two-body recoil frame covariance. The white vertical dotted line indicates the overlap of the two pulses at t_0.

During the dissociation of the parent monocation, the charge is mostly carried by the larger fragment than the smaller fragment due to the higher ionization potential energy of the smaller fragment. As a result, the medium-sized fragments carry away the charges and are produced with neutrals in the (1,0) channel. The dissociation of the parent dication into the (1,1) channel is energetically favorable, which results in the production of small fragment ions in the (1,1) channel. Therefore, small charged ions are preferably produced with other medium-sized ions in the (1,1) channel than

being produced in the (1,0) channel. Although the medium-sized ions are being produced through both channels (1,0) and (1,1), the (1,0) channel is observed to be more pronounced because of the larger production of the parent monocations as shown in Figure 6.4(b). A similar trend in the preference of the channels is shown for other small and medium-sized fragments in Section 8.2.1 of the Appendix.

6.2.5.2   Internal relaxation lifetimes

The experimental delay-time dependent ion yields are displayed with green points in Figure 6.5(c) and 6.5(d). The black curve shows the final fit result, which has two major components, namely the step function (magenta curve) and transient peaks (blue, orange, and brown curves). The step function corresponds to the transition from the Vis-pump/XUV-probe (negative Δt) regime to the XUV-pump/Vis-probe (positive Δt) regime. The pronounced increase/decrease in the ion yields are depicted by transient peaks, which are observed in the positive Δt regions, i.e., we observed transient features when the FLU molecules are first pumped by the XUV photons to the singly and doubly ionized states, and the resulting parent monocations and dications dissociate through a number of fragmentation pathways after interaction with the Vis pulses. The various fragmentation channels arise from different ensembles of electronic states, giving rise to different relaxation lifetimes for each channel. In the following, we address the average electronic relaxation lifetimes of FLU monocation and dication obtained from the data on dissociation into $C_4H_x^+$ through the (1,0) and (1,1) channel. The $C_4H_x^+$ ion is highlighted as an example, which shows all the features observed across the other fragment ions.

FLU^{+*}: After absorbing an XUV photon, the FLU monocation may be formed in electronically excited states (FLU^{+*}), which relaxes over time to low-lying electronic states depicted as FLU^+. The relaxation process is probed using Vis pulse, as shown schematically in Figure 6.5(a). Near t_0, FLU^{+*} may undergo two processes, denoted by pathways (1) and (2). The Vis pulse may induce dissociative ionization, promoting FLU^{+*} to FLU^{2+*} that dissociates into $C_4H_x^+$ and $C_9H_y^+$ (the (1,1) channel of $C_4H_x^+$), demonstrated by pathway (1) following the blue arrows. As a side note, $C_4H_x^+$ could also be produced with other monocations in a (1,1,0) channel with neutral co-fragments. Another possibility is that FLU^{+*} can spontaneously dissociate through the (1,0) channel of $C_4H_x^+$ before the arrival of the probe pulse. The Vis pulse can ionize the neutral fragments produced in the (1,0) channel of $C_4H_x^+$ and convert the (1,0) channel to a (1,1) channel as indicated by pathway (2) following the green arrows. During this conversion, the two charged fragments in the resulting (1,1) channel are still close enough to face a strong Coulombic repulsion and must appear in the (1,1) channel region of the momentum distribution. Upon arrival of the Vis pulse during the evolution of the system along pathway (2), the (1,0) channel can in principle also lead to a (2,0) channel, if the Vis pulse ionizes the charged fragment

($C_4H_x^+$) rather than the neutral C_9H_y, thus there may also be a conversion from the (1,0) to the (2,0) channel.
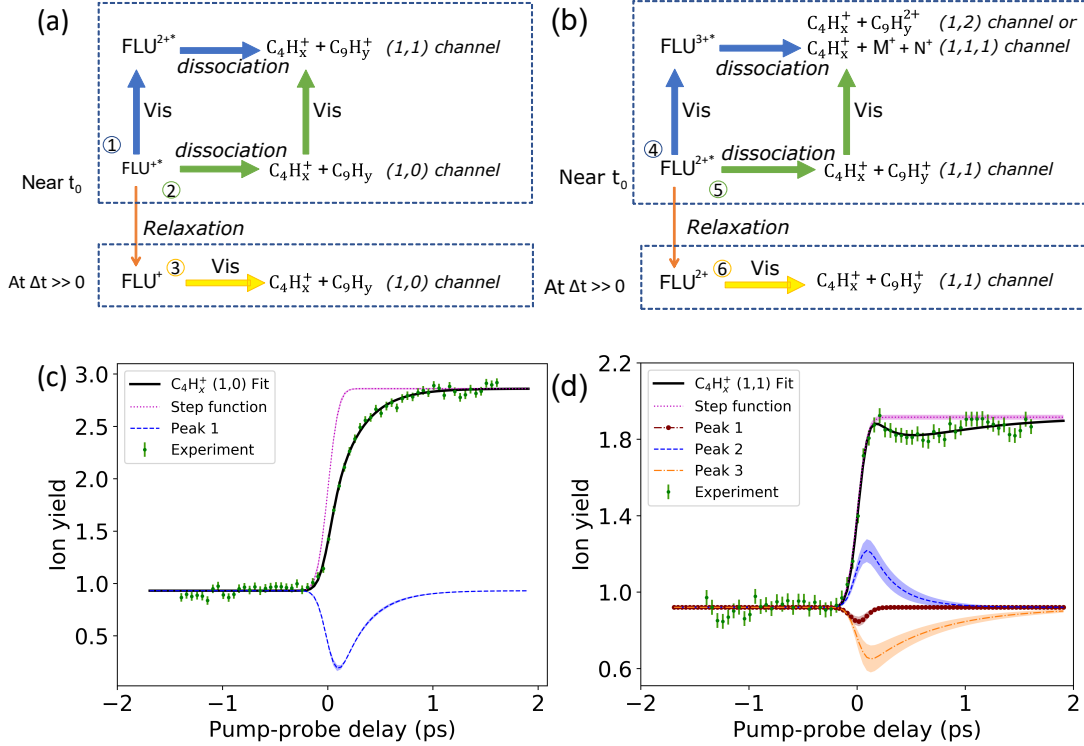
Figure 6.5: Schematics of the XUV-pump, Vis-probe regime for the monocation and dication, (a) and (b), respectively. The orange arrow depicts the relaxation of electronically excited ions over time. The letters M and N depict other possible fragments, which may be produced with the fragment $C_4H_x^+$. Ion yield dependences (in (b)) on the pump-probe delay time for the fragment ion $C_4H_x^+$ are shown for both (1,0) (c) and (1,1) channel (d). The green curves with the error bars are the experimentally obtained results. These green curves are fit, yielding the black curve that is the final fitted curve, which is the result of transient peaks (blue, brown, and orange) and the step function (magenta curve). In all the curves the shaded area depicts the error. c) The downward transient peak in the (1,0) channel depicts the transient depletion in the ion yield. d) The (1,1) channel is fitted with three transient features, which comprises two peaks showing a transient decrease in the ion yields (peak 1 and peak 3) and one peak indicating transient increase (peak 2).

Since double ionization of the small fragment has a comparable low probability and we do not observe this conversion, this process is not discussed here and is not

included in the schematic. At longer delay, the FLU^{+*} electronically relaxes (orange arrow in Figure 6.5(a)), and the Vis pulses can only lead to dissociation of relaxed FLU^+ through the (1,0) channel (pathway (3)).

Overall, these three pathways contribute to the transient increase in the (1,1) channel of $C_4H_x^+$ (blue peak 2 in Figure 6.5(d)), which matches the transient decrease in the (1,0) channel of the $C_4H_x^+$ yield (blue peak 1 in Figure 6.5(c)) near time Δt = 0. The timescales of the transient peaks correspond to the relaxation lifetime of the FLU^{+*} electronic states, which lead to the formation of $C_4H_x^+$ in the channels described above. These lifetimes are found to be 259 ± 14 fs and 238 ± 59 fs, for the depletion of the (1,0) (pathway (3)) and increase in the (1,1) channel (pathways (1) and (2) in Figure 6.5(a), respectively). In addition to relaxation *via* carbon loss fragmentation channels, the H-loss channel also shows a transient increase, with a relaxation lifetime of 136 ± 5 fs. All other fragments have similar transient increase and decrease features in their (1,1) and (1,0) channels, respectively, except $C_2H_x^+$, where the data had a significant N_2^+ contamination. These are shown in Section 8.2.2 of the Appendix.

FLU^{2+*}: XUV photon absorption also forms FLU in an electronically excited dication state, FLU^{2+*}. Similar to the processes described above, near t_0 we probe a number of dissociative pathways. Pathway (4) demonstrates dissociative ionization of FLU^{2+*} after interaction with Vis photons forming FLU^{3+*}, which dissociates through either (1,2) or (1,1,1) channels (monocation recoiling against two other monocations), shown in Figure 6.5(b) following the blue arrows. The other pathway (5) depicts spontaneous dissociation of the FLU^{2+*} ions into the (1,1) channel, before the arrival of the Vis pulse. The Vis pulse may lead to the formation of the (1,2) or (1,1,1) channel of $C_4H_x^+$. If alternatively there is a sufficiently long delay time, the FLU^{2+*} molecules relax to FLU^{2+}, and promotion to the next ionization state by the Vis pulse is less favored. The relaxed FLU^{2+} can then dissociate through the (1,1) channel upon arrival of the Vis pulse.

We observed two peaks depicting transient depletion in the ion yields in the (1,1) channel of $C_4H_x^+$, indicated as peak 1 (brown) and peak 3 (orange) in Figure 6.5(d). The less intense peak 1 corresponds to a short lifetime of 13 ± 12 fs showing the depletion in the ion yield near t_0. This depletion is attributed to the corresponding transient increase in the (1,2) channel of $C_4H_x^+$. In our experiments, the signal for the (1,2) channel is very low, which could be due to the less intense probe pulse, and the corresponding increase in the (1,2) channel is not observed clearly. But the presence of the (1,2) channel for the fragment ion $C_3H_x^+$ was visible in a previous study with a different probe (810 nm), and a similar short lifetime of 17 ± 5 fs was reported [28]. Therefore, the peak 1 can be attributed to the shifting of population from the (1,1) channel to the (1,2) channel of $C_4H_x^+$ near t_0.

Peak 3 with a long lifetime of 661 ± 108 fs can be attributed to the formation of

the (1,1,1) channel. The Vis pulse initiated formation of the (1,1,1) channel, which involves production of three fragment ions, which can be produced at any time after the Vis pulse interaction. This leads to their production in a longer time span resulting in longer lifetime. The corresponding increase in the (1,1,1) channel cannot be shown since this channel will have a large momentum distribution that could not be disentangled through the momentum maps. To summarize, the relaxation lifetime of FLU^{2+*} is determined *via* three pathways (4), (5), and (6), which result in transient depletion in the (1,1) channel resolvable for conversion into two dissociation channels, namely the (1,2) channel with a lifetime of 13 ± 12 fs and the (1,1,1) channel with a lifetime of 661 ± 108 fs.

In addition to the FLU^{2+*} lifetimes obtained through the carbon skeleton fragmentation channels, we also obtained the relaxation lifetime of the FLU dication dissociating through the H-loss channel, which was found to be 112 ± 7 fs. The H-loss relaxation lifetimes of FLU^{2+*} and FLU^{+*} are similar and indicate that hydrogen loss from the parent ion, which involves σ-bond fission, is unaffected by the difference in the charge states that are mostly localized in the conjugated π-system. The lifetimes extracted from other fragments are tabulated in section 8.2.2 of the Appendix.

The fragment ions with higher masses than $C_6H_x^+$ were fitted with a single transient increase peak. The absence of multiple peaks in the (1,1) channels for these heavier mass fragments is attributed to the following two reasons. Firstly, the conversion from the (1,1) channel to the (1,2) channel for the higher masses might be inaccessible since the small partner ions of these large fragments are difficult to doubly ionize by the Vis pulse, due to the higher ionization potential compared to the larger fragments and even higher double ionization potential. Secondly, the (1,1,1) channel is formed by the dissociation of the FLU trication into smaller fragments, and hence this channel is likely to have a significantly smaller branching ratio due to the fact that one of the fragments is already large.

Relaxation lifetimes for near-ionization-threshold electronic states of FLU^{2+*} could also be extracted from the transient increase in the FLU trication signal. As depicted in process (4) in the schematic of Figure 6.5(b), the Vis pulse absorption by FLU^{2+*} results in the formation of the FLU trication, observed as a transient increase in the FLU^{3+} ion yield. This transient peak corresponds to a relaxation lifetime of 180 ± 36 fs, which was measured using 405 nm Vis photons as the probe pulse ($\sim 390~\mu J$ pulse energy). The relaxation lifetime was also determined before using XUV-IR (30.3 nm and 810 nm) [28] pump-probe studies to be 126 ± 16 fs, which is somewhat lower compared to the XUV-Vis studies reported here.

6.2.6 Discussion

The effect of fragment size on the observed relaxation lifetimes can be explained as follows. The relaxation of the electronically excited FLU monocation and dication is probed *via* Vis pulses by inducing dissociation and/or dissociative ionization. Various fragment ions thus produced would show different relaxation lifetimes (τ_r) of FLU$^+$ and FLU^{2+}. The effect of the fragment ion's size on the τ_r can be observed in Figure 6.6(a) and 6.6(b), where we plot the identified relaxation lifetimes as a function of the number of carbon atoms in the fragment ion. The respective τ_r of FLU^{+*} determined through the (1,0) channel and the (1,1) channel are depicted by the blue curves in Figure 6.6(a) and 6.6(b). The small fragments with two to eight carbons atoms have similar lifetimes (τ_r) as compared to the large fragments $C_9H_x^+$ and $C_{10}H_x^+$.
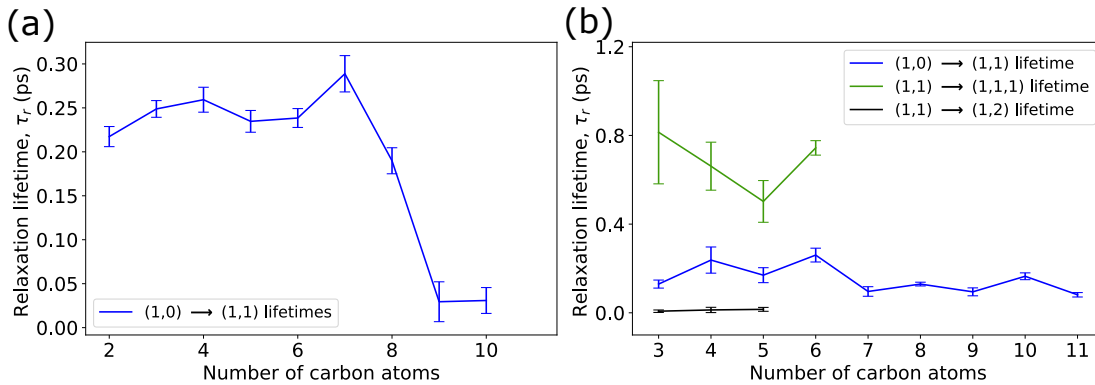
Figure 6.6: Observed trends as a function of fragment size. a) Relaxation lifetime of FLU^{+*} plotted as a function of the number of carbon atoms of the fragment, with which the relaxation lifetime is associated. This demonstrates the depletion of the (1,0) channel and the formation of the (1,1) channel. b) Relaxation lifetime of FLU monocation and dication plotted as a function of the number of carbon atoms of the fragment obtained from the (1,1) channel, depicting three processes. First, conversion of the (1,0) channel to the (1,1) channel, which corresponds to the electronic relaxation lifetimes of the FLU monocation (blue curve). Second, conversion of the (1,1) channel to the (1,2) channel, which corresponds to the electronic relaxation lifetimes of the FLU dication (black curve). Third, conversion of the (1,1) channel to the (1,1,1) channel, which also corresponds to the electronic relaxation lifetimes of the FLU dication (green curve). The fragment ion $C_2H_x^+$ with a lifetime of 2.985 ± 0.008 ps, which would be on the blue curve, has been omitted for better visibility of the other fragments with much shorter lifetimes. The fragment ion $C_{11}H_x^+$ was fitted without a transient feature, and no relaxation lifetime could be extracted through this fragment ion.

The longer and shorter relaxation lifetimes for the small and large fragments, respectively, can be explained as follows: as can be inferred from the covariance maps (Figure 6.3), the smaller fragments have more possible dissociation partners, and hence more fragmentation pathways are associated with them. The relaxation of FLU^{+*} into these multiple pathways, involving the formation of a small fragment with various other partners, is not completely resolvable. The resultant transient peaks thus have contributions from all possible formation pathways, and hence longer lifetimes are observed compared to the large fragments having a relatively small number of formation pathways resulting in shorter lifetimes.

The $C_{11}H_x^+$ fragment ion is an exception to the lifetimes extracted from other large fragment ions. This exception is attributed to the fact that the formation pathway of $C_{11}H_x^+$ involves acetylene loss from the parent species. This pathway is thought to progress *via* a mechanism involving rearrangement of the rings to allow C_2H_2 loss described in reference [122], which is not the case for the C_3H_x loss or C_4H_x loss leading to the formation of other large fragments.

The relaxation lifetimes of the FLU^{2+*} were obtained from the shift of population from the (1,1) channel to the (1,2) and (1,1,1) channels of small fragment ions. The absence of these features in the large fragments was explained in the previous section. The observation of similar lifetimes for small fragments is consistent here as depicted by the green and black curve in Figure 6.6(b).

The effect of probe pulse on the observed relaxation lifetimes is observed as follows. As reported in the results section, the relaxation lifetimes of FLU^{2+*} are found to be different when probed with IR and Vis pulses. This difference in the recorded lifetime with the Vis pulse is attributed to its higher probe energy, which is able to excite lower-lying states of FLU^{2+*} to FLU^{3+*}, resulting in an increase in the observed relaxation lifetimes.

6.2.7 Summary

We studied the interaction of FLU molecules with XUV radiation, which is present in the interstellar medium as the He II emission line. FLU was observed to undergo numerous processes, involving single and double ionization, dominant single dehydrogenation post single ionization, and fragmentation into various carbon loss channels with acetylene loss being a major process. The fragments observed in the mass spectrum can be thought of as potential ions that would be present in the ISM as a result of UV-induced photodissociation.

The recoil-frame covariance technique exhibited the primary, secondary, and tertiary fragmentation of the parent dication that has occurred from a high amount of residual energy given by the high-energy photons. The ultrafast pump-probe measurements with the 405 nm probe enabled us to investigate the ultrafast decay

89

of electronically excited and highly energetic parent ions that are promoted to the next charge state dissociation and/or non-dissociation channels.

Interaction with high-energy photons opened the possibility for parent ion dissociation through a large number of fragmentation pathways. The momentum resolution provided by the velocity map imaging made it possible to distinguish between several channels for the fragments, which we label as (1,0), (1,1), and (1,2) channels. Detailed analysis of the fragments showed the transient depletion and enhancement of the ion yields, as a result of FLU^{+*} and FLU^{2+*} ions' temporal relaxation into different energy levels. It is interesting to observe the time-resolved shift of the population from one channel to another one of the observed fragments, revealing the lifetimes of the species they are formed from. The results enabled us to determine the dependence of the relaxation lifetimes on the fragment size. These relaxation lifetimes were reported to be in the range of 10 fs to a few ps. The range of the lifetimes is similar to the lifetimes that were reported to be in the range of 10 to 100 fs using XUV-IR pump-probe spectroscopy [27, 28, 47].

In this work, we used and discussed different experimental and analytical tools to investigate the fundamental photophysics and chemical processes engaged after the interaction of fluorene with XUV radiation. Through these processes, the relaxation lifetimes of fluorene parent ions were extracted, which are beneficial to gain a complete view of the timescales of relaxation of small vibronically excited PAHs present in the ISM. All dissociation products from fluorene were found to have reaction pathways decaying on the sub-picosecond timescale, indicating non-adiabatic relaxation mediated by a high number of conical intersections. As PAHs typically have a high density of states, similar to fluorene, ultrafast relaxation across all charge states investigated might be expected amongst PAH molecules in general. Overall, exploring the possible reaction pathways of the fluorene cations in their non-radiative regime is advantageous for the fundamental femtochemistry and astrochemistry fields.

6.3 IR-Vis pump-probe spectroscopy

6.3.1 Introduction

The fundamental properties of astrochemically-relevant PAHs are important to address for gaining a complete understanding of the rich interstellar chemistry. There are laboratory experiments designed specifically to investigate such molecules, and thus to explore interstellar chemistry [27, 28, 45, 64, 121, 123]. The radiation emitted from various sources, e.g. synchrotrons, free-electron lasers, optical lasers, electron beam, ion beam, etc, are used in such experiments to mimic the radiations present in the ISM, and to cover various regions differing in the energy that can be absorbed by PAHs. Besides using radiation of various wavelength, experiments with varying

pulse intensities are also required to provide a detailed insight into the interaction of the molecules with radiation. Generally, when the field strength of the radiation is different, one phenomenon can be observed to occur more predominantly than another, leading to different fragmentation patterns.

In this work, the stability of fluorene molecules when interacting with an intense infrared (IR) pulse (1.53 eV photon energy) is investigated by employing the relatively less intense Vis pulse (3.06 eV photon energy) as a probe. Both pulses are produced from the femtosecond (fs) table-top Ti:Sa laser placed near the CAMP endstation at the FLASH I. As a consequence of the interaction, ionization and dissociation processes occur. The mechanisms of ionization processes that are initiated by the interaction of the intense ultrashort pump pulse with the molecules can be governed by the Keldysh parameter (γ) [124]. The strong-field studies indicate that in the region when $\gamma \ll 1$, field ionization or tunnel ionization (TI) mechanism is dominant, whereas when $\gamma \gg 1$, multiphoton ionization (MPI) is a major mechanism. This Keldysh parameter γ is given by

$$\gamma = \sqrt{\frac{I_{\mathrm{P}}}{18.67476 \times 10^{10} \times I \times \lambda^2}} \tag{6.1}$$

where I_{P} is the first ionization potential of the molecule, I is the laser field intensity in W·cm^{-2}, and λ is the wavelength of the laser in nm. For the IR laser field used in this experiment, the pulse intensity of the order 10^{13} W·cm^{-2} is used having a few 50 fs of pulse duration. γ is calculated to be 2.1, which falls in the intermediate regime, where the contribution from both kinds of ionization processes (MPI and TI) can be expected. For this study, the investigation of ultrafast changes in the molecules in this mixed regime remains the area of interest. The results are presented and discussed in detail as follows.

6.3.2   Dissociation pathways of multiply ionized fluorene

After absorption of the IR radiation at an intensity of 1.4×10^{13} W·cm^{-2}, plenty of fragmentation and ionization channels of fluorene are observed to be accessible *via* the time-of-flight (TOF) mass spectrum (see Figure 6.7). The abundance of the single dehydrogenated fluorene monocation (i.e., the fluorenyl cation) is larger than the parent monocation, which is also observed in the experiments using the XUV as the pump pulse [see section 6.2]. Extensive carbon backbone fragmentation is observed as well. Since the resolution of the mass spectrum is limited to resolving the carbon backbone fragmentation, the hydrogen atoms in the fragment ions are depicted by the variables 'x' and 'y', where x and y vary from 1 to 10. The presence of fragment ions could be attributed to MPI that leads to the fragmentation of the fluorene monocation into several dissociation channels. However, the formation of

91

these fragments from a doubly and triply ionized fluorene is also observed which hints at the presence of the TI mechanism, as discussed in the following.

The presence of the highly ionized fluorene and their dissociation products can be explored using the velocity map images. These images are beneficial to disentangle various momentum regions of the fragment ions. In a fragmentation process, the momentum imparted to the product ions depends on their partner ions. The formation of two monocations would result in more Coulombic repulsion and hence more momentum than the formation of one monocation with one neutral product. The various possibilities of the fragmentation processes are depicted in the dissociative states in Figure 6.8. The Jablonski diagram represents a schematic of the accessed ionized and dissociative states. For the mentioned reasons, the product ions of the (2,2) channel would have the highest momentum and the product ions of the (1,0) channel would have the least momentum as depicted in Figure 6.8.
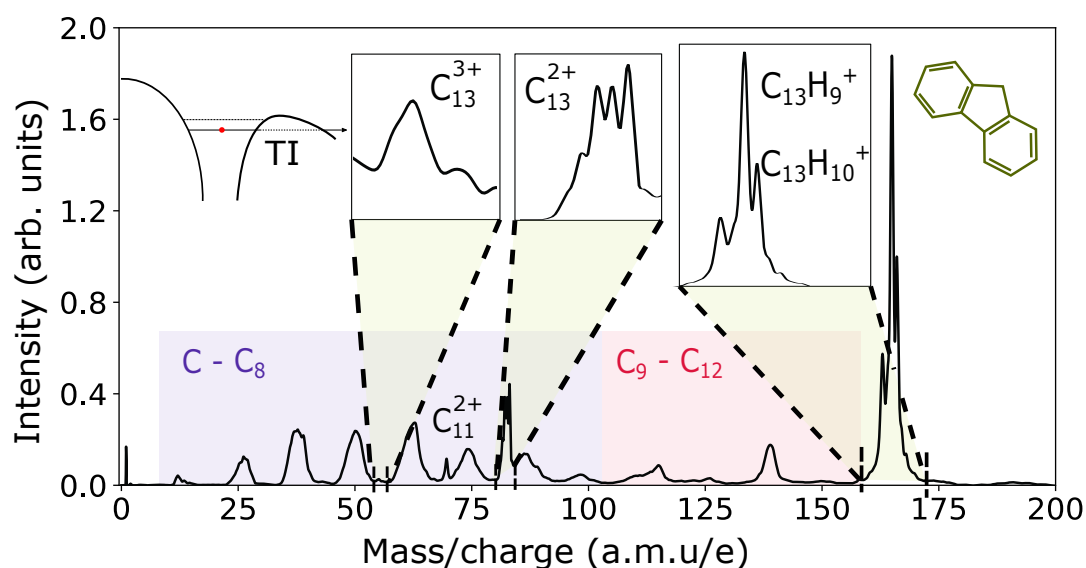
Figure 6.7: The time-of-flight mass spectrum obtained after interaction of the molecules with the infrared (IR) pulses. The insets indicate the presence of the parent trication, the dication, and a dominant dehydrogenated fluorene monocation. The presence of tunnel ionization (TI) processes upon irradiation of fluorene with intense IR radiation can be explained through the features observed in the mass spectrum.

92
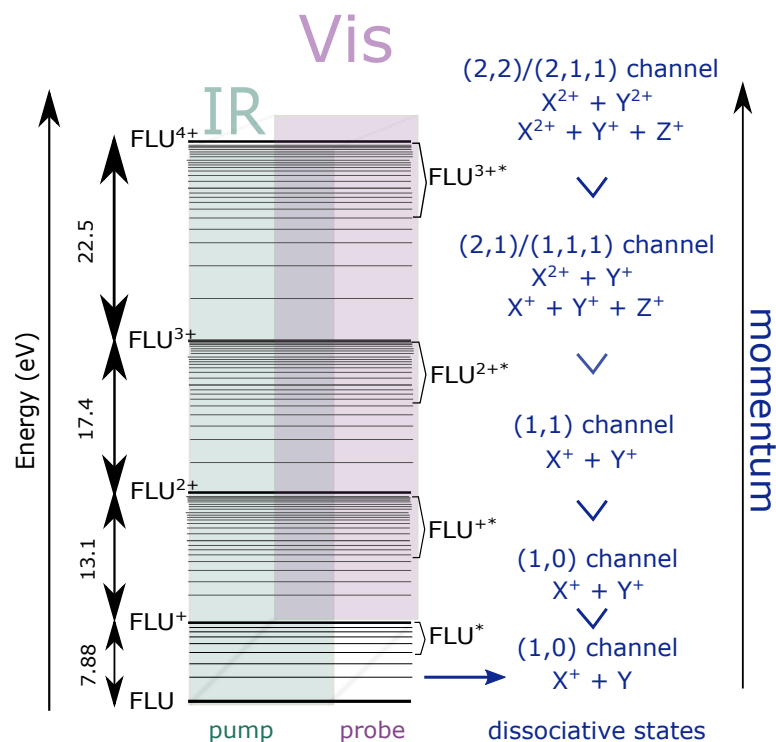
Figure 6.8: Jablonski diagram of fluorene and its ionic states. The first and second ionization potentials (I.P.) of FLU are taken from the experimental measurements provided in Ref. [125] and [126], respectively. The third and the fourth I.P. are computed using the ωB97/def2-TZVPP level of theory. The green-shaded region shows the states accessible by the infrared (IR) pulse. The pink-shaded region depicts the states accessed by the visible pulse as a probe. The dominant dissociative states are also given. Due to Coulombic repulsion, the momentum of a tetracation breaking apart into two dications (the (2,2) channel) imparts larger momentum than the trication leading to the formation of one dication and one monocation (the (1,2) and (2,1) channel). Thus, the dissociation of the parent monocation *via* (1,0) channel leads to the lowest momentum channel, and the formation of the two dications, the (2,2) channel, would have the highest momentum channel.

The resolved momentum regions obtained through velocity-map imaging (VMI) enable the assignment of these mentioned channels, which is shown by the momentum profiles in Figure 6.9. These momentum profiles for each fragment ion can be plotted by angular integration of the velocity-mapped image shown as an inset in Figure 6.9. The details of this process are described in Section 4.2.1.2. The presence of the signal in the (2,2) channel of the ion $C_{11}H_x^{2+}$ indicates the presence of the fluorene

tetracation, which is leading to dissociation *via* the (2,2) channel.
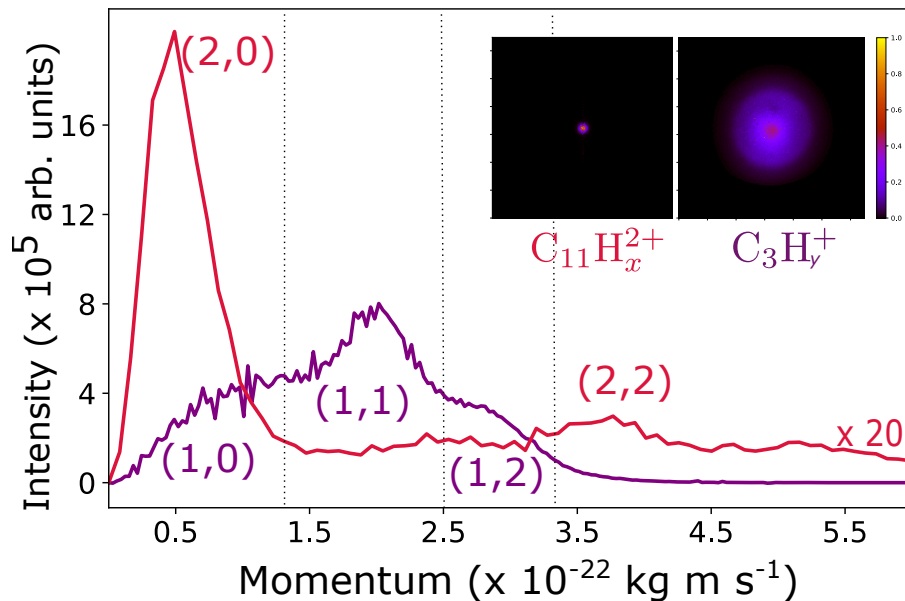
Figure 6.9: Momentum profiles of two exemplary fragment ions $C_3H_y^+$ and $C_{11}H_x^{2+}$. The x and y are the number of hydrogen atoms in the fragment ions, where x and y varies from 1 to 10.

Therefore, double, triple, and quadruple ionization processes followed by dissociation are observed, popularly known as ladder-climbing processes [124]. The MPI mechanism would need a minimum of 25 photons to triply ionize the fluorene molecules, and thus the TI mechanism is indicative. Since the laser intensity falls in the intermediate regime, where the TI and MPI mechanisms both contribute, the occurence of the TI mechanism would be expected [124, 127–129].

Above threshold ionization (ATI) features are also visible in the photoelectron spectra (see Figure 6.10), which are known to be observed in the MPI processes. The ATI features are characterized by a similar energy gap amongst the adjacent peaks in the photoelectron spectrum equivalent to the incident photon energy. The photoelectron spectrum shown in Figure 6.10 potrays five peaks that are spaced with an energy of ~1.3 - 1.8 eV, which is approximately equivalent to the IR photon energy of 1.53 eV. From these observations, we can state that as a result of combined effects, all the vibronically excited states of the fluorene mono-, di-, and trication along with the dissociative states can be assumed to be accessed by the IR pulse as shown by the green-shaded part in Figure 6.8. The Vis pulse shifts the accessibility to the metastable tetracation as is evident from Figure 6.9, which shows a signal in

the high momentum (2,2) channel in the momentum profile of the $C_{11}H_x^{2+}$ ion. The presence of the high momentum channel with the dication as an observable indicates dissociation of the parent tetracation into the two dications. Since the signal-to-noise ratio in the metastable fluorene tetracation dissociation channel is low, the formation of the metastable tetracation is considered to be the upper limit in the aspect of accessibility by the probe pulse.
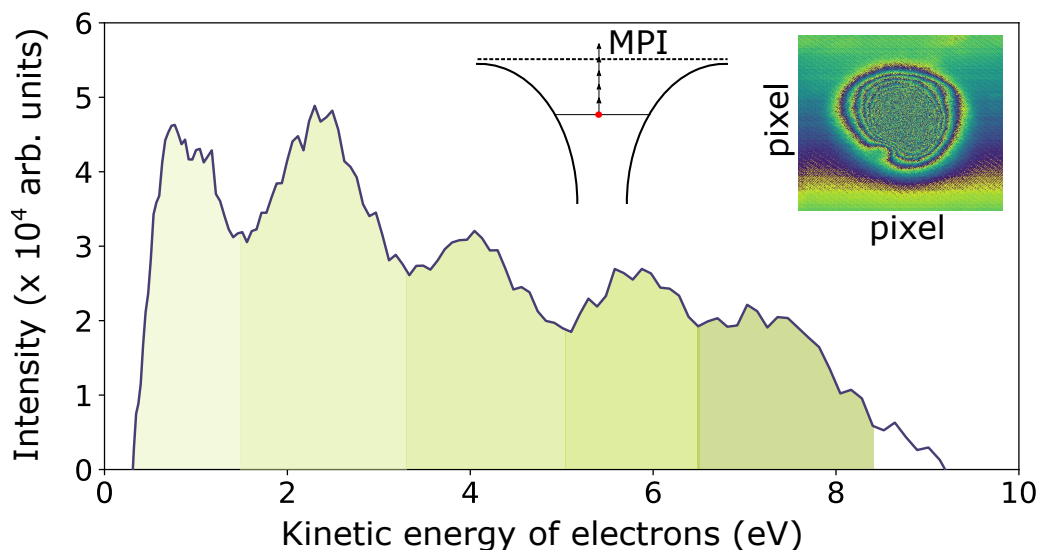
Figure 6.10: The photoelectron spectrum acquired by angular integration of the electron image (shown in the image) shows the above threshold ionization, which is a feature indicating multiphoton ionization (MPI).

The qualitative analysis of the TOF mass spectrum in Figure 6.7 also shows that the relative abundance of the larger fragment ions (fragments ions with a number of carbon atoms between 9 and 12) is lower than for the smaller fragment ions (fragments ions with a number of carbon atoms between one and 8). A proposed reason for this observation is the relaxation of the larger fragment ions *via* dissociation into smaller fragment ions. The recoil frame covariance analysis (RFCA) performed on the velocity-mapped images shown in Figure 6.11 by Dr. J.W.L. Lee gives information on the co-production of the two ions and is represented as cov(A,B), which reads as the covariance of ion A in reference to ion B. Further details are in the references [28, 117]. RFCA shows a lower signal for the larger fragment ions than for the smaller ions. This means that the cov(large,small), i.e., the formation of the large fragment ions in reference to the smaller partner ion is lower than the cov(small,small), which corresponds to the formation of the small fragment ions in reference to the other

fragment ions. The brighter signal in the cov(small, small) indicates the process involving the dissociation of a larger fragment ion into smaller ions. The stronger clue to confirm this fragmentation pattern can be achieved from the pump-probe delay time (t_{pp}) *vs.* ion yield curves.
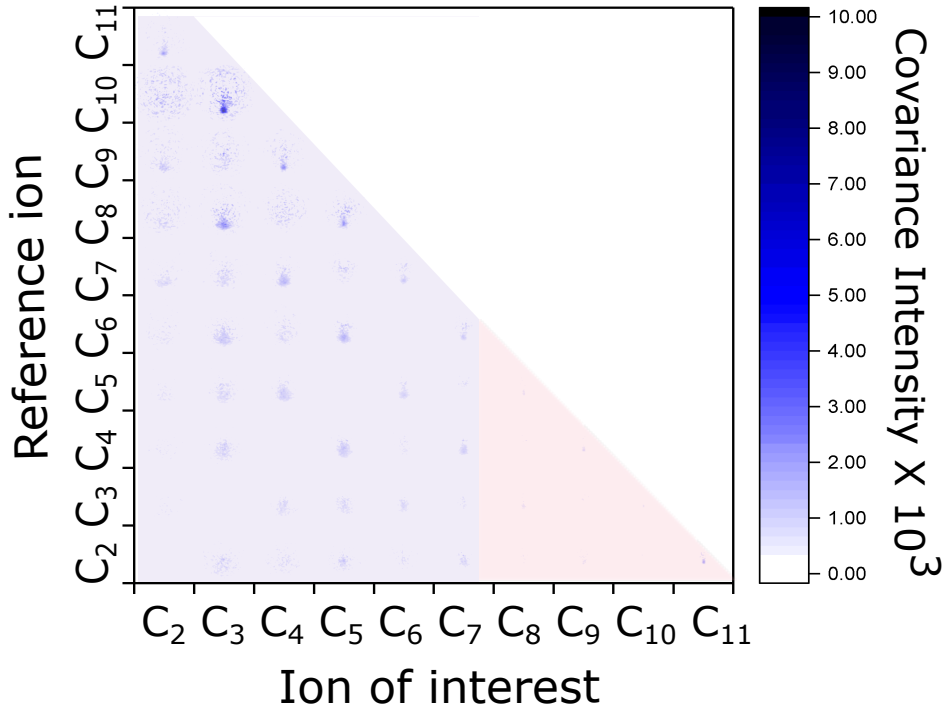
Figure 6.11: Two-body recoil frame covariance, which is grouped into larger fragment ions (pink) and smaller fragment ions (purple).

The pump-probe delay time (t_{pp}) *vs.* ion yield curves are obtained by integrating over the momentum axis of different channels and are fitted using the Pump-Probe Multiple Channels Markov Chain Monte-Carlo Fitting routine, which is introduced in Section 4.2.2.2 and in detail in Ref. [104]. The in-house developed software used for fitting can be accessed through Ref. [106]. The software allowed us to fit 40 datasets together, which gave a fair estimate of the overlapping timing of the pump and probe pulses, that is, the time at which $t_{\mathrm{pp}} = 0$, called t_0. All the pump-probe delay time (t_{pp}) *vs.* ion yield curves shown here are shifted by this t_0 value. Time delays of $t_{\mathrm{pp}} < 0$ indicate the Vis pulse acting as the pump and the IR pulse acting as a probe, and $t_{\mathrm{pp}} > 0$ is the region when the IR pulse is the pump and the Vis pulse is the probe.

96
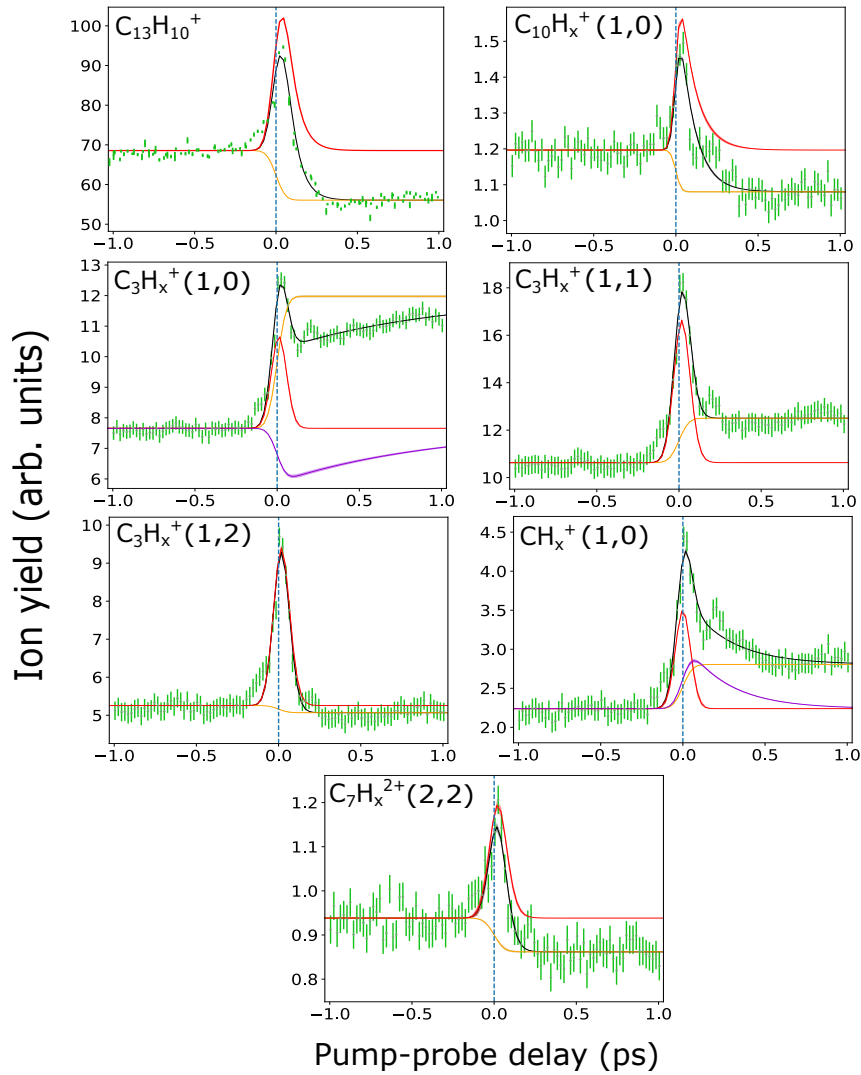
Figure 6.12: The pump-probe delay time *vs.* ion yield curves for several ions. The green curve shows the experimentally obtained results. The black solid line represents the final fit curve, whose components are shown using yellow, red, and purple curves. The yellow curve depicts the step function, and the red and purple curves illustrates the transient features.

Referring to Figure 6.12, at later pump-probe delays ($t_{pp} \gg 0$), the parent ion ($C_{13}H_{10}^+$) yield shows a decrease (yellow curve), which is also observed for the large fragment ions (shown for $C_{10}H_x^+$ (1,0) channel as an example). This is accompanied by an increase in the ion yield of small fragment ions shown as the step-up curve for the fragment ion $C_3H_x^+$ in its (1,0) channel as an example. This observation of the

step-down and step-up features for large ions and small ions respectively is consistent for the (1,0) channel (see pump-probe delay curves in Section 8.3.1 of Appendix).

6.3.3 Vibronic relaxation lifetimes

Besides the fragmentation pattern, the relaxation lifetimes of the highly-excited vibronic states are obtained. The basic model to explain this is shown in Figure 6.13. The neutral molecules A interact with the pump and reach the vibronically excited state B*. In our experiments, this B* state can be any of the states amongst those depicted shaded in green in the Jablonski diagram in Figure 6.8. B* relaxes with time into lower-lying states with rate constant τ_r. If the probe pulse arrives before the species B* relaxed, that is, $t_{pp} < \tau_r$, it quenches the relaxation by further ionization or dissociation, to prepare an observable C.
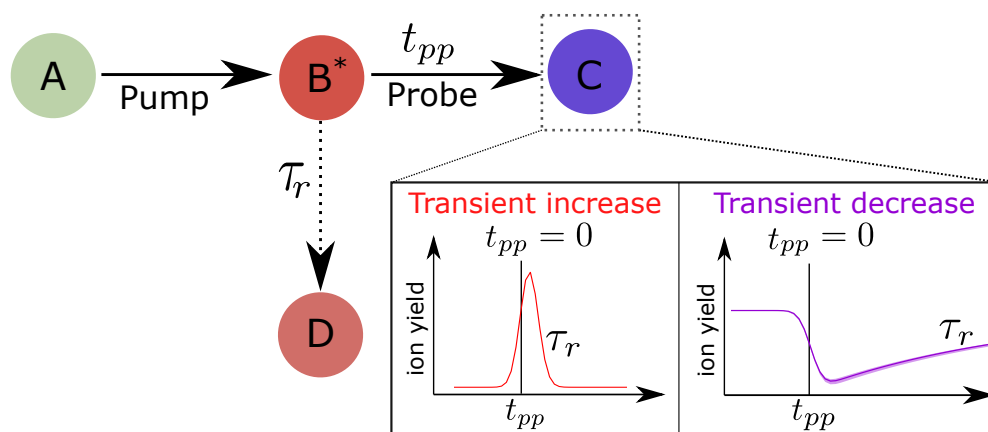
Figure 6.13: A is typically an intact fluorene molecule in our case, which after interacting with the pump pulse can create any state as depicted in the green-shaded region in Figure 6.8. These are excited states subjected to relaxation to state 'D' with the rate constant τ_r. The probe pulse arrives after a delay of t_{pp} and creates the observable 'C'.

The curve of the observable C would show a transient increase or decrease depending on the involved process and observable under investigation. If the processes are dissociative, then a transient decay will be observed in the ion yield of the entity that is subjected to dissociation. Whereas if the ionized states or dissociation products are observable, transient increase will be observed. Based on this model, we could obtain the relaxation lifetimes of the parent ions and the small fragment ions that are explained in detail in the following. Some of the transient features could not

be completely resolved due to either too short or too long lifetimes and will be mentioned as they come across. To ease the readability fluorene is written as FLU, and the '*' symbol depicts the hot vibronic state.

1. Relaxation lifetime of FLU*

   (a) From parent monocations

   To understand the processes, let us assume the replacements of the entities shown in Figure 6.13. A is FLU, B* is FLU* and C is FLU$^+$. When the probe pulse arrives before FLU* relaxes, which is near $t_{pp} \sim 0$, it could induce ionization, and a transient increase is observed in the ion yield of FLU$^+$. Therefore, the lifetime of the transient feature shown by the red curve in Figure 6.12, labeled by $C_{13}H_{10}^+$, reveals the vibronic relaxation lifetime of FLU* species. These lifetimes are extracted to be 61.7 $\pm$ 0.9 fs from FLU^{+*} as observable.

   (b) From various dissociation channels

   In this case, consider the following replacements, A is FLU, B* is FLU* and C is the (1,0) channel of the fragment ions. The probe pulse, when interacting with the vibronically excited FLU, can lead to the formation of the parent monocation (as stated in the previous point) which is subjected to dissociation in the (1,0) channel of any monocation. For example, the transient increase near $t_{pp} = 0$ shown by the red curve for the ion $C_3H_x^+$ depicts its transient formation. The relaxation lifetime of the fluorene in a vibronically excited state can thus be obtained. Including all the fragment ions in (1,0) channel (with the lifetimes provided in Section 8.3.2 in Appendix), the range of the lifetimes from these fragmentation channels is obtained to be 10 to 92 fs.

2. Relaxation lifetime of FLU^{+*}, FLU^{2+*}, and FLU^{3+*}

   In a similar way, the relaxation lifetimes of the parent monocation FLU^{+*} can be obtained by observing the transient increase in the ion yield of FLU^{2+*}, the fragment monocations in the (1,1) channel, and the fragment dications in the (2,0) channel. The transient increase in the ion yield of the fragment ion $C_3H_x^+$ in the (1,1) channel is depicted in Figure 6.12, while the others are plotted in Section 8.3.1 of the Appendix. The lifetime of FLU^{+*} is thus found out to be in the range from 19.5 to 83.9 fs. The vibronic lifetimes from individual channels are plotted in Section 8.3.2 in the Appendix as a function of the number of carbon atoms in the fragment.

   The relaxation lifetime of FLU^{2+*} is determined from the transient increase in the ion yield of FLU^{3+*}, the fragment monocations in the (1,2) channel, and

the fragment dications in the (2,1) channel. The delay time *vs.* ion yield curve is plotted for the (1,2) channel of the fragment ion $C_3H_x^+$ as an example. The extracted relaxation lifetimes are reported to be in the range of 19.6 to 135.7 fs. The individual vibronic relaxation lifetimes extracted through all the (1,2) channels for all the fragments and the parent trication are plotted in Section 8.3.2 in Appendix.

The formation of stable FLU^{4+*} is not observed in the mass spectrum (see Figure 6.7), and the lifetime of FLU^{3+*} can only be obtained through the transient increase in the ion yield of two fragment dications, $C_7H_x^{2+}$ and $C_{11}H_x^{2+}$ in the (2,2) channel, which corresponds to relaxation lifetimes of 27 fs and 51.7 fs respectively. The delay time *vs.* ion yield curve is plotted for the C_7^{2+} ion in Figure 6.12.

3. Relaxation lifetimes of the small fragment ions

The ladder-climbing process can be ultrafast, and the dissociation of the parent monocations can happen before the probe pulse arrives. In this case, A is FLU, B^* is a small fragment in the (1,0) channel, and C is a transient decrease in the ion yield of the small fragment ion in the (1,0) channel itself or increase in the yield of the species it is dissociating to, which is, in this case, the carbon monocation (1,0) channel. The purple peak in the delay-time *vs.* ion yield curve of the (1,0) channel of $C_3H_x^+$ ion in Figure 6.12 shows the transient decay of the ion yield. As soon as the probe pulse arrived, it imparts energy, which is spent in further dissociation leading to the transient depletion in the signal. The corresponding increase in the dissociative states of the product species would be expected. This increase in the ion yield is observed in the (1,0) channel of carbon monocation depicted by the purple color in Figure 6.12.

The lifetimes of these small fragment ions are found to be longer than the lifetimes of the parent species. The lifetimes of the large fragment ions could not be extracted because the transient decay feature was not resolved due to overlap with the overall step-down curve (see pump-probe delay time *vs.* ion yield curve of the large fragment ion $C_{10}H_x^+$ in Figure 6.12). The lifetimes of the small fragment ions $C_2H_x^+$ to $C_8H_x^+$ could be resolved to be in the range of 128 to 966 fs. The individual lifetimes extracted through all the small fragments are plotted in Section 8.3.2 in the Appendix.

6.3.4 Summary

The intermediate Keldysh parameter regime portrays both the MPI and the TI processes. It is shown that ionization followed by dissociation is observed, which is known as the ladder-climbing process explained in Ref. [124]. This ladder-climbing

process can be supported by the delay-time *vs.* ion yield curves (shown in Section 8.3.1 of Appendix) of the different electron bands shown in Figure 6.10. The relaxation lifetimes of the electrons match the lifetime of the parent monocation, which indicates that the electrons are ejected predominantly with the parent species rather than from the fragments.

The TI and MPI processes together expand the accessibility of the states to the triple ionization *via* intense IR pulse. This enabled us to explore a plethora of excited states and provide a detailed insight into the dynamic processes of fluorene molecules. To conclude, there are three main points,

1. The fragmentation pattern after the fluorene molecules interact with the IR pulse indicates the breakdown of the larger fragment into the smaller ions. This observation can be compared with the interaction of fluorene with XUV radiation, where single-photon processes are dominant. In the differential mass spectrum illustrated in Figure 6.1b, if the large fragment ions would be dissociating into small fragment ions, then the ion yield of the large ions would show depletion in the ion yield. In the mass spectrum, no such depletion is observed for the large fragment ions (ions with 8 to 11 carbon atoms). The intense depletion is observed only for the parent species ($C_{13}H_{10}^+$ and $C_{13}H_9^+$). Therefore, all the fragment ions can be estimated to be formed from the parent species only in the case of XUV interaction.

2. The relaxation lifetimes of the parent neutral, mono-, di-, and trications through various dissociative and ionized states are obtained to be in the range of a few 10 fs to a few 100 fs. These lifetimes are relatively fast with respect to the dynamic processes happening in the interstellar medium. Therefore, these species can be approximated to be in their ground states while forming theoretical models.

3. The relaxation lifetimes of the small fragment ions formed as the result of the interaction of the intense radiation with fluorene could also be probed. These relaxation lifetimes span a duration of a few 100 fs to 900 fs, which are found to be longer than the parent ions. The extended range of the relaxation lifetimes of these fragments indicates the need to explore more PAHs having aromatic rings of different arrangement, number, and size to generalize the hypothesis of PAHs being in their ground state in the ISM without limiting it to small PAHs.

Chapter 7

Summary and future outlook

The photophysical and photochemical properties of astrochemically-relevant poly-cyclic aromatic hydrocarbons (PAH) were addressed by means of two spectroscopic techniques, namely Near Edge X-ray Absorption Fine Structure (NEXAFS) and time-resolved femtosecond pump-probe spectroscopy. These techniques could be realized using the large-scale facilities, PETRA III and FLASH, available at the Deutsches Elektronen-Synchrotron DESY research facility. The significance of using these two spectroscopic approaches is highlighted in the Introduction (Chapter 1). Later on in the thesis, each chapter has two sections addressing these two techniques.

The electronic structure was obtained for cationic phenanthrene $C_{14}H_{10}^+$ and its dehydrogenation state $C_{14}H_9^+$, using NEXAFS spectroscopy. While synchrotron radiation from PETRA III enabled performing the X-ray absorption spectroscopy, the Photon-Ion spectrometer at PETRA III (PIPE) setup was demonstrated to be a versatile tool to investigate the electronic structure of PAH cations at the carbon K-edge in the gas phase [64]. The experimental method was described in detail in Section 3.1 of Chapter 3.

The theoretical results were observed to match well with the experimental results when the vibrational averaging was performed to include the effects of thermal motion of the ions, which was achieved by calculating the lineshape of the theoretical spectrum (Section 2.1 of Chapter 2). The assignment of the peaks in the experimentally obtained absorption spectra using the detailed theoretical results highlighted the most prominent transitions between the carbon $1s$ and the unoccupied molecular orbitals (UMOs). In addition to the electronic structure, the SOMO-LUMO gap could be extracted for the $C_{14}H_{10}^+$ ion. Lowering of this gap was observed qualitatively as a dehydrogenation effect for the $C_{14}H_9^+$ ion, mentioned in Chapter 5.

NEXAFS spectroscopy performed at the PIPE endstation was shown to be a supporting tool to investigate the structural changes after dehydrogenation of the phenanthrene monocation. This can be exploited further, and structural changes of the carbon skeleton of the PAH cations can be investigated after the step-wise

removal of the hydrogens. Nitrogen-substituted PAH (PANH) cations can also be investigated and the effect of substitution on the electronic structure can be explored at nitrogen K-edge. Investigation of the PANH cations using both the nitrogen K-edge and carbon K-edge will provide a complete understanding of the molecular orbital structure from two different perspectives.

In addition to the NEXAFS performed at the PIPE endstation, we used femtosecond pump-probe spectroscopy to explore the fragmentation pattern and relaxation dynamics of the PAH fluorene when interacting with intense radiation. From 1930-1940s and 1990s, experimental methods like time-of-flight mass spectrometery and velocity map imaging were exploited to gain a detailed insight into molecular dynamics. The combination of the two methods made it possible to achieve good resolution in time-of-flight and momentum space. The experimental methods used in thesis are described in Section 3.2. Two types of radiation fields were used as pump radiation, namely, femtosecond extreme ultraviolet radiation from the free-electron laser (40.9 eV photon energy) and femtosecond near-infrared radiation from a table-top Ti:Sa laser (1.53 eV photon energy). In both cases, a visible pulse (3.06 eV photon energy) was used as a probe.

When interacting with the XUV radiation, single photon absorption processes were involved to ionize, dissociate, and excite the fluorene molecules in vibronic states. The time-of-flight spectrum along with the velocity map imaging of the parent and fragment ions made it possible to disentangle various formation pathways of fragment ions. Knowing these formation pathways led to revealing the vibronic relaxation lifetimes of fluorene monocation and dication. These lifetimes were reported to be in the range of a few tens of femtoseconds to a few picoseconds. These complicated yet accessible processes were described using a detailed schematic in Section 6.2.

When interacting with the intense IR pulses, the combination of multiphoton ionization and tunnel ionization processes took place making a surplus amount of vibronically excited states accessible for the probe pulse. The thorough analysis of all the formation channels of fragment ions aided in the extraction of relaxation lifetimes of excited fluorene molecules, excited fluorene ions in their mono-, di-, and tricationic states, and also excited fragment ions of small size (fragment ions with two to eight carbon atoms), that is, fragments having one to eight carbon atoms. These relaxation lifetimes were reported in the range of a few femtoseconds to a few hundred femtoseconds. The detailed analysis supported by the velocity map images of the electrons (carried out by Dr. Denis S. Tikhonov) indicates the dominance of ionization followed by dissociation processes. The detailed insight is provided in Section 6.3.

The sophisticated experimental procedures employed for the pump-probe spectroscopy at the CAMP endstation were well supported by an in-house developed analysis routine that was explained in detail in Section 4.2. The simultaneous mea-

surements of the electron VMI and the ion VMI together with the TOF spectrum facilitate multiple analytical tools such as TOF-TOF partial covariance, two-body recoil frame covariance, and photoelectron photoion covariance to gain information on the dynamics of the molecular processes. Further, this rich combination of experimental and analytical processes can be used to investigate the dynamics of PAHs of different numbers and arrangements of aromatic rings. The variation of the vibronic relaxation lifetimes with these different types of PAHs will be helpful for the astronomical society to gain detailed photophysical and photochemical properties of the molecules in the interstellar medium. So far, we probed a relaxation lifetime of a few 10 fs to a few ps for small PAHs and their cations. Therefore, the small PAHs (three to four rings) can be estimated to be present in their ground states in the interstellar medium.

To conclude, by using XUV and intense-IR excitation pulses, we explored ensembles excited by different ionization processes, namely single-photon ionization, multiphoton ionization, and tunnel ionization. The resulting fragmentation patterns illustrate prominent single dehydrogenation of fluorene molecules. The interaction with intense radiation indicates the presence of quadruply charged fluorene ions. The vibronic relaxation lifetimes are extracted to be in the range of a few 10 fs to a few ps combing all the observations from XUV-Vis and IR-Vis studies. Since the processes of astronomical interest are slower than these ultrafast relaxation timescales of small PAH fluorene, small-size PAHs can be considered in their ground state, especially while forming the theoretical models relevant for ISM. To generalize this hypothesis of small-size PAHs being in the ground state to all the PAHs, a similar detailed investigation covering various possible sizes and types of PAHs would be beneficial. The intense radiation from large-scale facilities such as PETRA III and FLASH can be used to mimic the interstellar harsh radiation to an extent. Exploring the femtochemistry and electron structures of the molecules in the laboratory contributes to knowing the physics and chemistry of PAH molecules even better.

Chapter 8

Appendix

8.1 Analysis details for the experiments at PE-TRA III

8.1.1 Theoretical X-ray absorption spectrum (XAS) calculation using various functionals.

In Figure 8.1, the XAS calculated using different functionals and their comparison with the experimental result are shown for the parent monocation $C_{14}H_{10}^{+}$. The hybrid functional B3LYP was used since it shows a satisfactory agreement with the experimental observations after the theoretical spectrum is shifted by 11.5 eV.

8.1.2 The effect of temperature on the XAS spectrum

The molecular ions produced from the ECR ion source will be in vibrationally, electronically, and rotationally excited states. Due to this reason, we considered the structures having relative energies below 10,000 K, which is an estimated high threshold value to include the energetic isomers produced *via* ECRIS. For $C_{14}H_9^{+}$, we considered ten structures in total. We used the Maxwell-Boltzmann distribution to estimate the contribution of these isomers in the final spectrum. The effect of temperature on the averaged spectrum is shown in Figure 8.2. The temperature is varied from 100 K to 5000 K. As can be observed, the temperature does not really affect the averaged spectrum. For the final calculations, we used a temperature of 800 K.
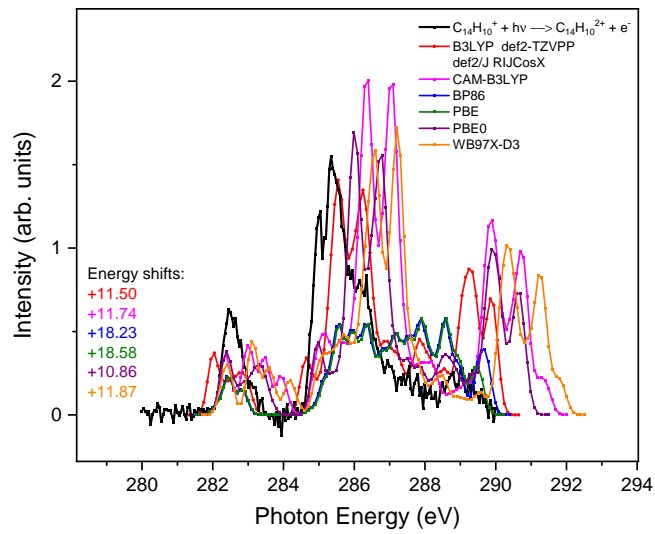
Figure 8.1: The theoretical XAS spectra calculated using various functionals and def2-TZVPP basis sets are shown. The shifts on the photon energy axis are applied to match with the experimental dataset (in black), and the shift values corresponding to each functional are provided at the left bottom consistent with the color scheme used to illustrate the different functionals.
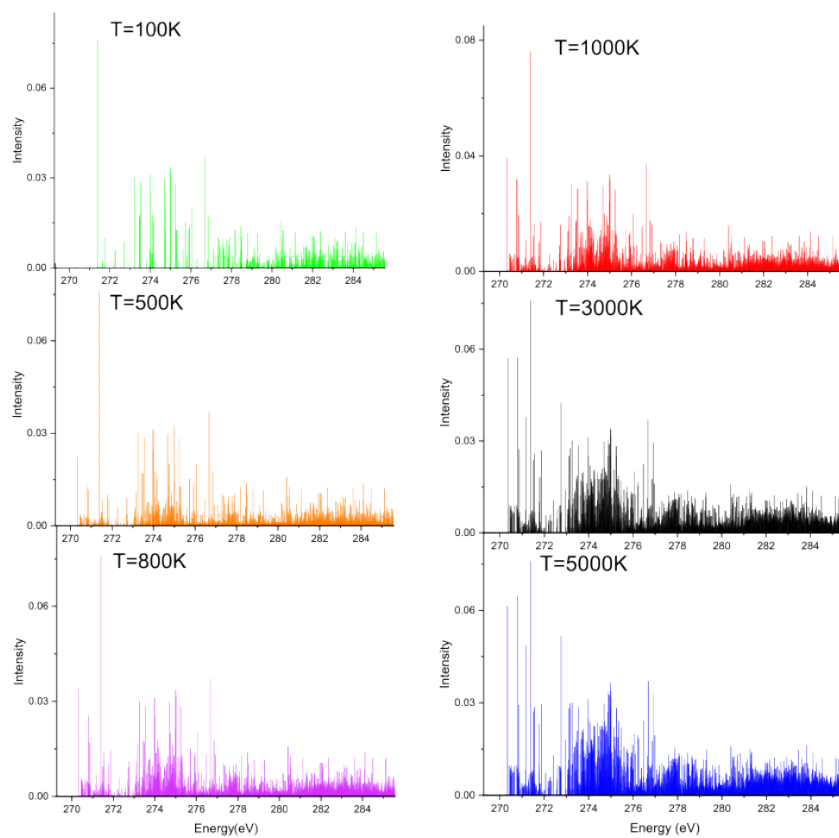
Figure 8.2: The XAS spectra calculated for different isomers, including the singlet and the triplet spin states of the primary ion $C_{14}H_9^+$ are shown at different temperatures. Different isomers are averaged according to the Maxwell-Boltzmann distribution at the respective temperature.

8.2 Analysis details for the XUV-Vis pump-probe experiments *

8.2.1 Time-resolved momentum distribution of all the fragment ions.

The momentum distribution as a function of pump-probe delay time is shown for all the fragments. It can be observed that the small-sized fragments (figure 8.3) $C_2H_x^+$, $C_3H_x^+$, and $C_4H_x^+$ are mostly produced through the (1,1) channel, whereas the medium-sized fragments (figure 8.4) $C_5H_x^+$, $C_6H_x^+$, $C_7H_x^+$, $C_8H_x^+$, and $C_9H_x^+$ are mostly produced via (1,0) channel. The large fragment, $C_{11}H_x^+$ also shows (1,0) as a dominant channel unlike another large fragment $C_{10}H_x^+$, which does not show any clear preference over the channels. (figure 8.5).
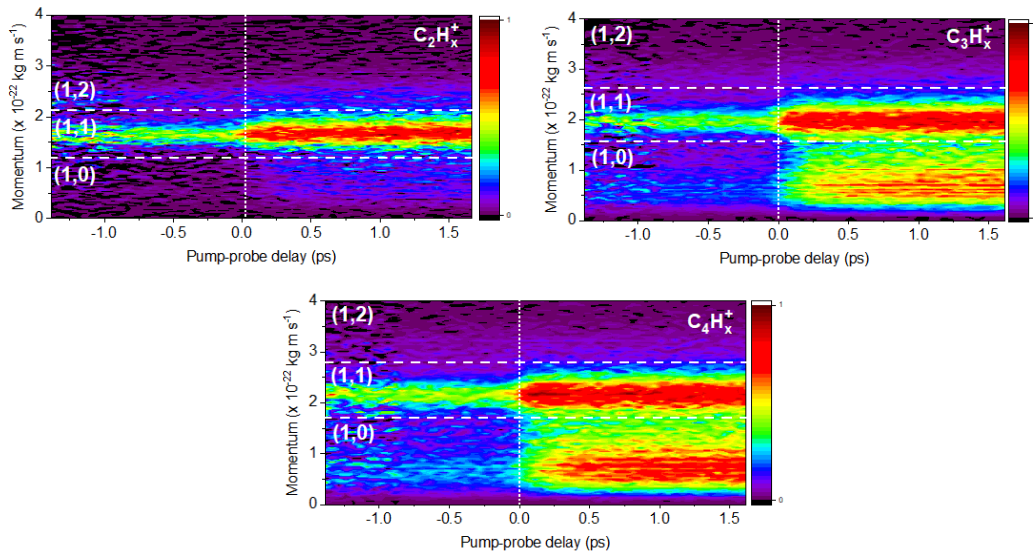
Figure 8.3: Momentum distribution as a function of pump-probe time delay for small-sized fragments showing the most intense signal in the (1,1) channel.

---

*This chapter is adapted from Ref. [29]. During the preparation of this manuscript, holes in the ion image were observed as shown in Figure 5A of the article, which was attributed to the defect in the detector. However, later, it was found that two of these holes were because of artifacts in the analysis scripts. These artifacts were minor, and do not change any major result. This section shares an updated version of all the quantitative data analysis updated information.
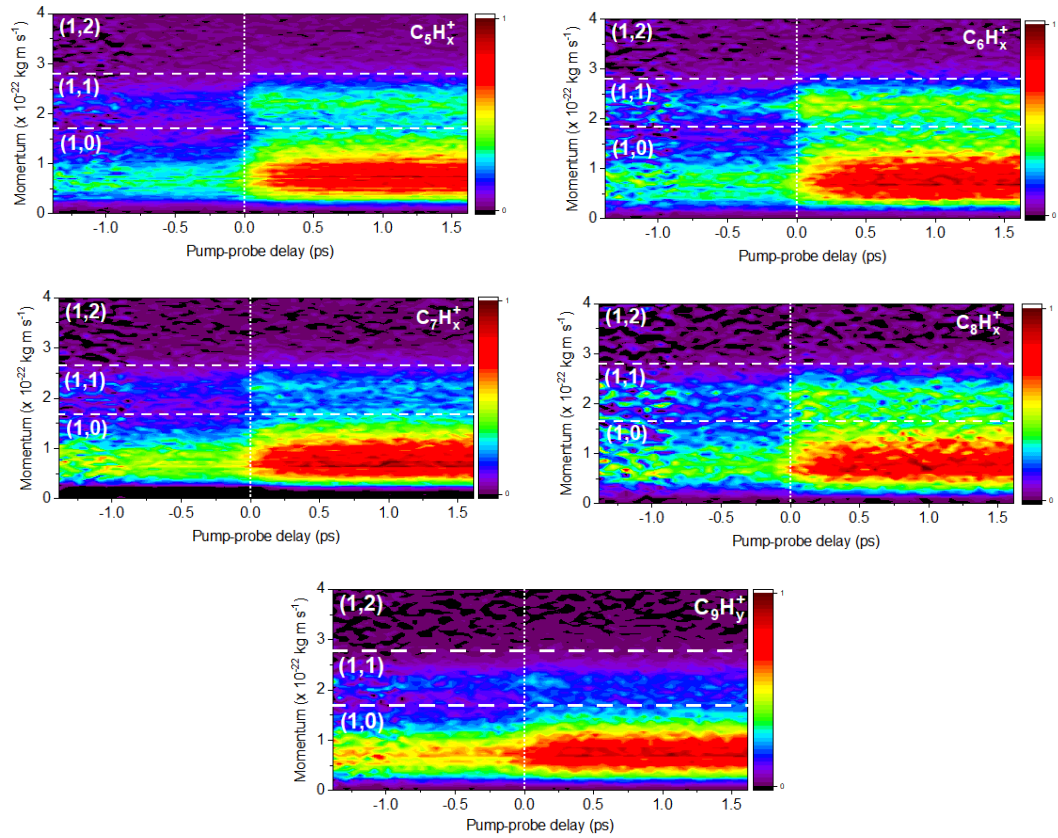
Figure 8.4: Momentum distribution as a function of pump-probe time delay for medium-sized fragments showing the most intense signal in the (1,0) channel.
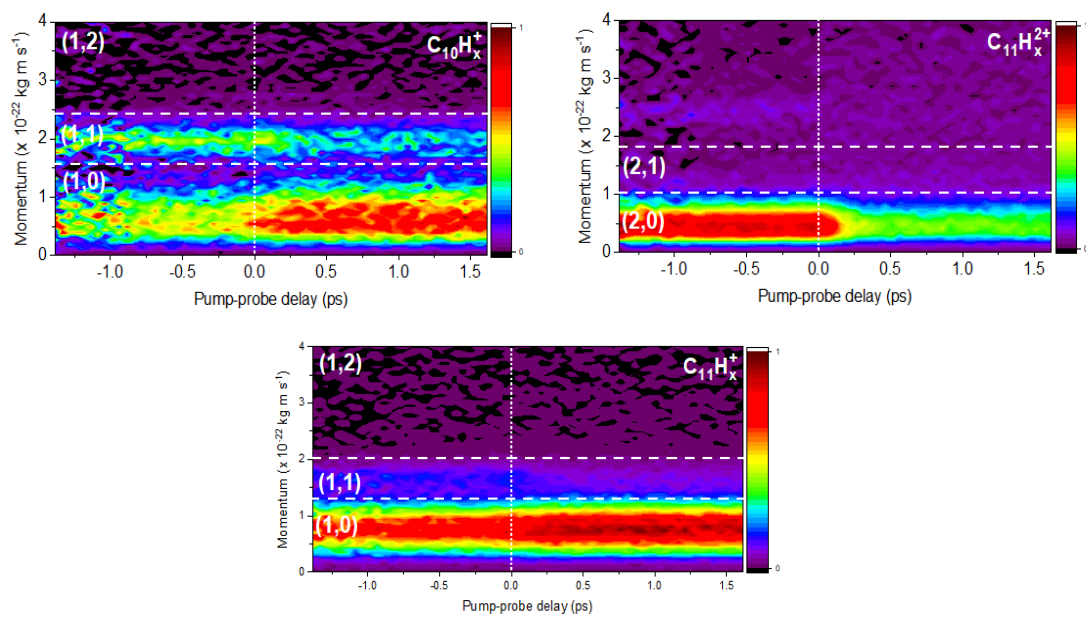
Figure 8.5: Momentum distribution as a function of pump-probe time delay for large-sized fragments.

8.2.2 Pump-probe dependent ion yield: Plots and the timescales.

The delay-time dependent ion yields were fit using Pump-Probe Multiple Channels Markov Chain Monte-Carlo Fitting (PPMC3). This fitting was done using an in-house build open-source Python library and script [106]. The details of the fitting procedure are described in the references [28, 104]. The parameters fitted were the cross-correlation time of the two pulses, the overlap time of the two pulses(t_0), and the transient lifetimes.

We performed Monte Carlo sampling with 10^5 points, implementing the global optimization. The t_0 was found with simultaneously fitting eighteen fits including the (1,0) channel of all the ten fragments ($C_2H_x^+$, $C_3H_x^+$, $C_4H_x^+$, $C_5H_x^+$, $C_6H_x^+$, $C_7H_x^+$, and $C_8H_x^+$ $C_9H_x^+$, $C_{10}H_x^+$, and $C_{11}H_x^+$), the (1,1) channel of the fragments: $C_2H_x^+$, $C_7H_x^+$, $C_8H_x^+$, $C_9H_x^+$, $C_{10}H_x^+$, and $C_{11}H_x^+$, the parent monocation and the parent dication. This t_0 value (9.558 ± 0.001 ps) was used as a constraint for the fits for the (1,1) channel of $C_3H_x^+$, $C_4H_x^+$, $C_5H_x^+$, $C_6H_x^+$, which exhibit multiple features. The parent trication and a fragment dication $C_{11}H_x^{2+}$, were also fit separately keeping the t_0 constraint. All the fitted plots are provided in figure 8.6, 8.7, and 8.8 The transient lifetimes are finally extracted from all the pump-probe dependent yields that are shown in the table 8.1. The values highlighted with pink depict the average relaxation lifetime of electronically excited parent monocation, and the values that are highlighted in blue show the relaxation lifetimes of the electronically excited parent dication.

113
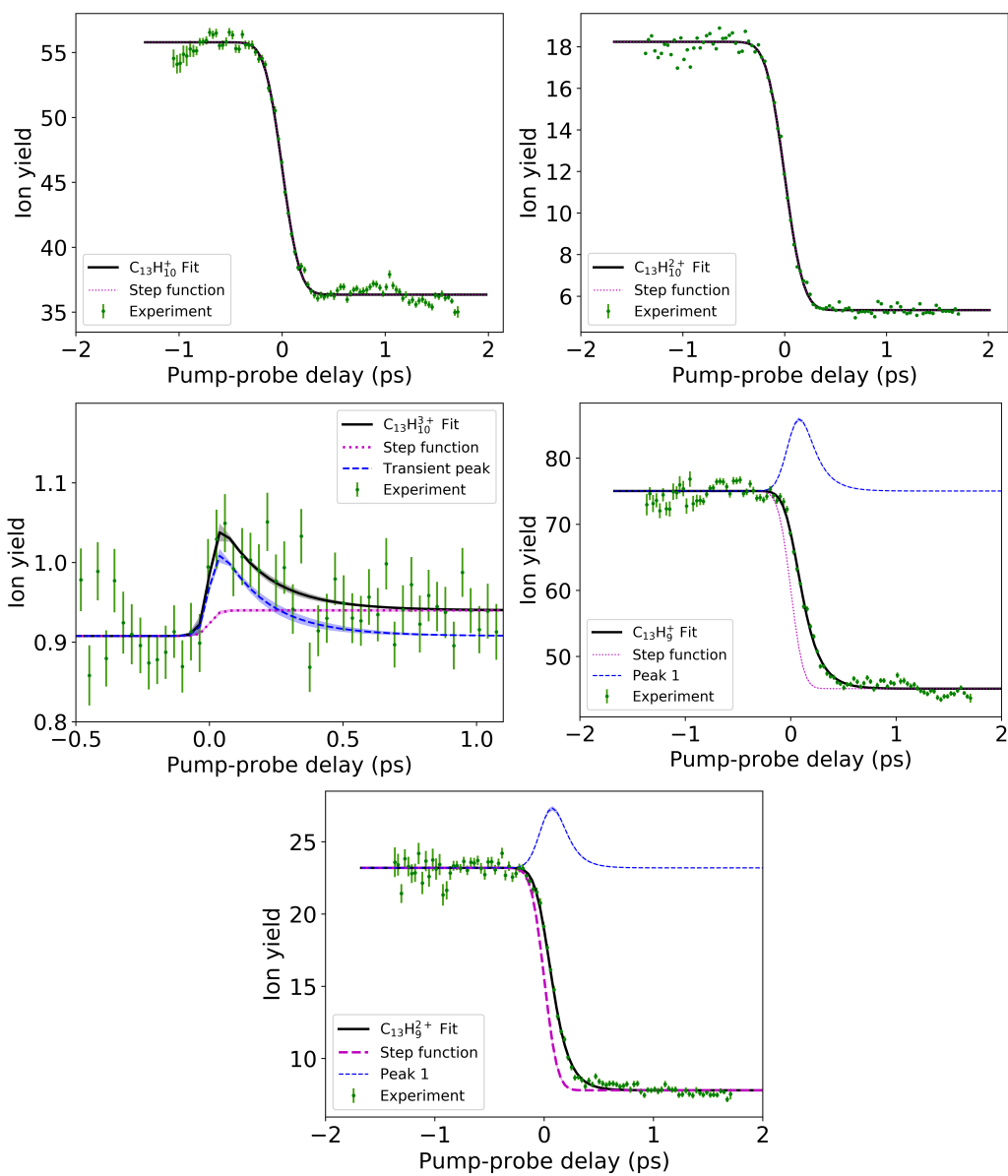
Figure 8.6: Pump-probe delay time dependent ion yields for the parent monocation, parent dication, parent trication, dehydrogenated parent monocation, dehydrogenated parent dication.
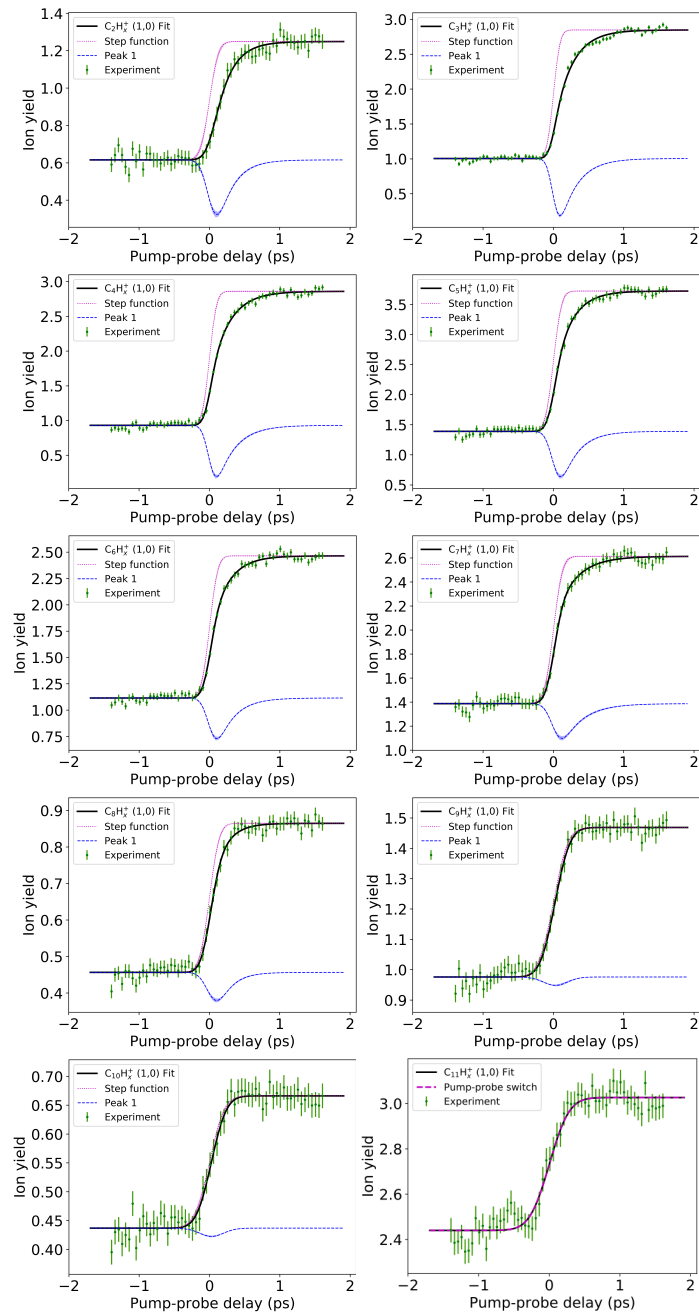
Figure 8.7: Pump-probe delay time dependent ion yields for the (1,0) channel of all the fragment ions.
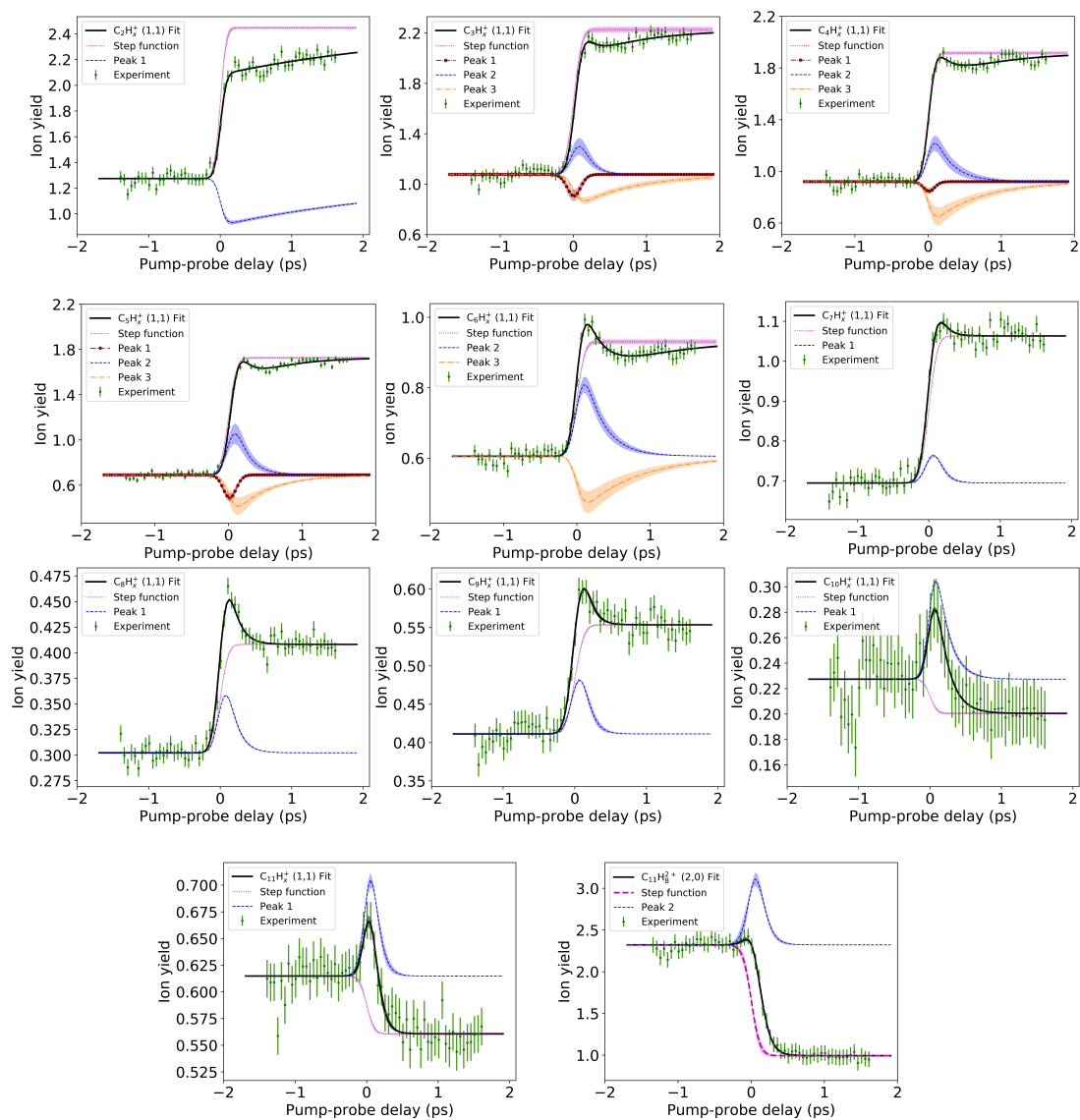
Figure 8.8: Pump-probe delay time dependent ion yields for the (1,1) channel of all the fragment ions, and also the (2,0) channel of the acetylene loss from the parent dication.

116

Ion	Channel	cross-correlation time (fs)	transient peak lifetime (fs)
$C_{13}H_{10}^+$	-	189±3	-
$C_{13}H_{10}^{2+}$	-	201±4	-
$C_{13}H_{10}^{3+}$	-	39±15	180±36 ↑
$C_{13}H_9^+$	-	133±5	136±5 ↑
$C_{13}H_9^{2+}$	-	134±6	112±7 ↑
$C_2H_x^+$	(1,0)	143±16	217±11 ↓
	(1,1)	93±10	2,985±8 ↓
$C_3H_x^+$	(1,0)	105±6	259±9 ↓
	(1,1)	127±14	7±5 (peak 1) ↓
			129±18 (peak 2) ↑
			814±232 (peak 3) ↓
$C_4H_x^+$	(1,0)	114±8	259±14 ↓
	(1,1)	106±8	13±12 (peak 1) ↓
			238±59 (peak 2) ↑
			661±108 (peak 3) ↓
$C_5H_x^+$	(1,0)	129±9	226±17 ↓
	(1,1)	122±7	15±8 (peak 1) ↓
			170±33 (peak 2) ↑
			502±94 (peak 3) ↓
$C_6H_x^+$	(1,0)	130±9	238±10 ↓
	(1,1)	121±7	260±31 (peak 1) ↓
			744±32 (peak 2) ↑
$C_7H_x^+$	(1,0)	143±13	289±20 ↓
	(1,1)	133±8	96±22 ↑
$C_8H_x^+$	(1,0)	157±12	190±15 ↓
	(1,1)	124±8	129±8 ↑
$C_9H_x^+$	(1,0)	235±17	29±22 ↓
	(1,1)	144±12	94±18 ↑
$C_{10}H_x^+$	(1,0)	238±19	31±15 ↓
	(1,1)	111±17	165±15 ↑
$C_{11}H_x^+$	(1,0)	-	- ↓
	(1,1)	118±23	81±10 ↑
$C_{11}H_x^{2+}$	(2,0)	136±31	82±24 ↑

Table 8.1: The average relaxation lifetimes of the parent monocation and the parent dication. The upward arrow shows the transient enhancement of the signal, whereas the downward arrow shows the transient depletion in the formation of ion yield. The pink-shaded and blue-shaded cells correspond to the parent monocation and dication relaxation lifetimes, respectively.

8.2.3   TOF-TOF partial covariance maps

The partial TOF-TOF covariance maps are shown in figure 8.9. The explanation of the TOF-TOF partial covariance is given in reference [109].
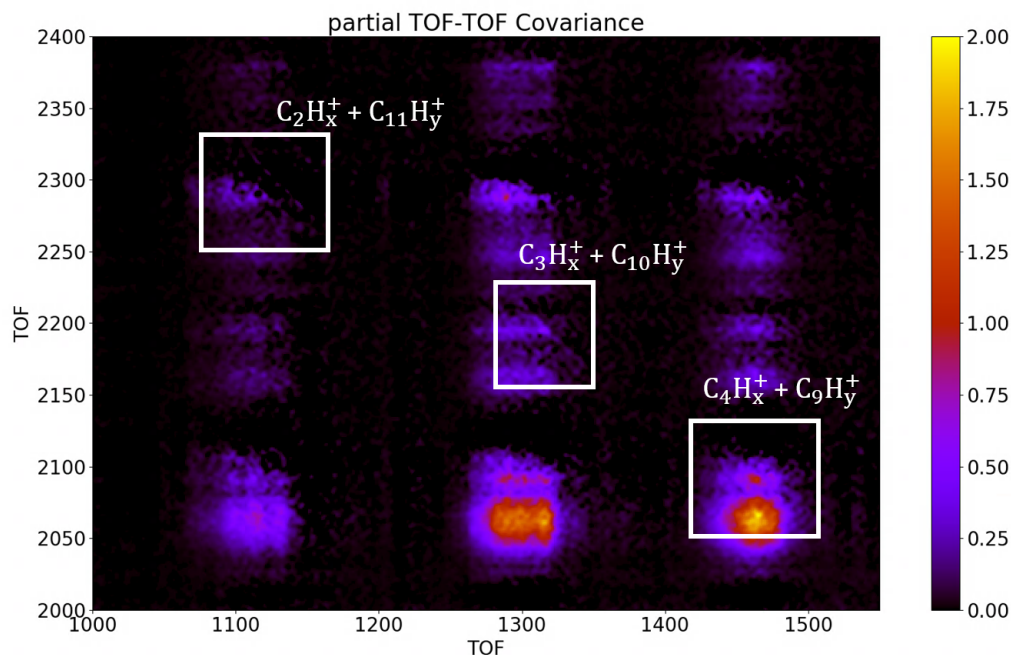
Figure 8.9: Partial TOF-TOF covariance map is shown. Three dissociation pathways are indicated in the figure.

8.2.4   Dissociation of parent mono- and di- cations *via* acetylene loss

The monocation, $C_{11}H_x^+$ is mostly produced in the (1,0) channel as can be seen in the figure 8.5 as a dissociation product from the parent monocation. Besides the parent monocation, the parent dication can dissociate in the (1,1) channel to form $C_{11}H_x^+$ with charged acetylene and the (2,0) channel to form $C_{11}H_x^{2+}$ with neutral acetylene. For small fragments, the formation of (2,0) channel is rare as compared to a large fragment for example $C_{11}H_x^{2+}$. This is why, when the parent dication dissociates into a very large fragment and a small fragment, the (1,1) channel and (2,0) channel, both are accessible. In order to know the preference of these possibilities, we calculated their dissociation energy using the Orca 4 program [130], applying the RIJCOSX approximation with def2/J auxiliary basis sets. The structures for all the species involved in each equation were optimized using the ωB97/def2-TZVPP

Reaction	dissociation energy in eV
$^1C_{13}H_{10}^{2+} \longrightarrow {}^2C_{11}H_8^+ + {}^1C_2H_2^+$	4.2 eV
$^3C_{13}H_{10}^{2+} \longrightarrow {}^2C_{11}H_8^+ + {}^1C_2H_2^+$	3.9 eV
$^1C_{13}H_{10}^{2+} \longrightarrow {}^1C_{11}H_8^{2+} + {}^1C_2H_2$	5.1 eV
$^3C_{13}H_{10}^{2+} \longrightarrow {}^1C_{11}H_8^{2+} + {}^1C_2H_2$	4.7 eV

Table 8.2: The dissociation energy of the parent dication into the (1,1) channel and the (2,0) channel involving the production of $C_{11}H_8^+$ are calculated through optimized geometry energy values. The values are calculated for singlet and triplet multiplicity of fluorene dication.

method. A previous study reported the dissociation energy of neutral and charged acetylene from the parent ions, where the position of acetylene loss and the spin state involved leading to low dissociation energy pathways are also reported [28]. Two adjacent carbon loss from the position depicted in figure 8.10 is used for the geometry optimization calculations with spin multiplicity two for a monocation, and one for dication. The parent structure was optimized using both the singlet and the triplet state for the dication, and the doublet state structure for the monocation. The involved reactions and the calculated dissociation energies are summarized in Table 8.2.
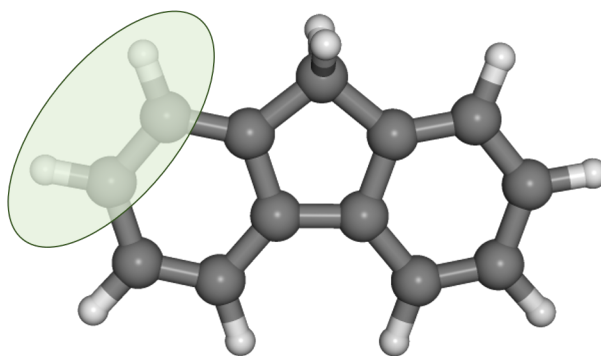
Figure 8.10: The shaded region shows the places from where the two carbons are removed.

8.2.5 Correction for FEL energy fluctuation

The pump-probe dependent ion yield were corrected for the shot-to-shot fluctuation in the FEL pulse energy by calculating the approximate number of photons involved in the ionization. The data was then corrected for the number of photons involved in the processes and are given in Table 8.3 for each fragment. To implement the correction, the ion-yield intensity was divided by the (FEL-pulse energy)^n, where 'n' is the calculated number of photons, and multiplied by the average FEL pulse energy.

Fragments	effective number of photons
$C_2H_x^+$	1.54 ± 0.07
$C_3H_x^+$	1.40 ± 0.05
$C_4H_x^+$	1.43 ± 0.05
$C_5H_x^+$	1.35 ± 0.05
$C_6H_x^+$	1.38 ± 0.06
$C_7H_x^+$	1.33 ± 0.05
$C_8H_x^+$	0.87 ± 0.08
$C_9H_x^+$	1.07 ± 0.06
$C_{10}H_x^+$	0.71 ± 0.09
$C_{11}H_x^+$	0.96 ± 0.04
$C_{11}H_x^{2+}$	1.36 ± 0.07
$C_{13}H_{10}^+$	0.58 ± 0.02
$C_{13}H_{10}^{2+}$	1.05 ± 0.06
$C_{13}H_{10}^{3+}$	1.01 ± 0.12

Table 8.3: The number of photons are calculated *via* a linear fit of the ln(signal) versus ln(FEL power) curve. The slope of the linear fit thus indicates the number of photons involved for a given fragment or parent ion. The number of absorbed photons absorbed is varied by one, illustrating the one-photon absorption process when PAH fluorene interacts with the XUV pulse.

8.2.6 Dependence of fragment ion size on the cross-correlation time and ion yield intensity
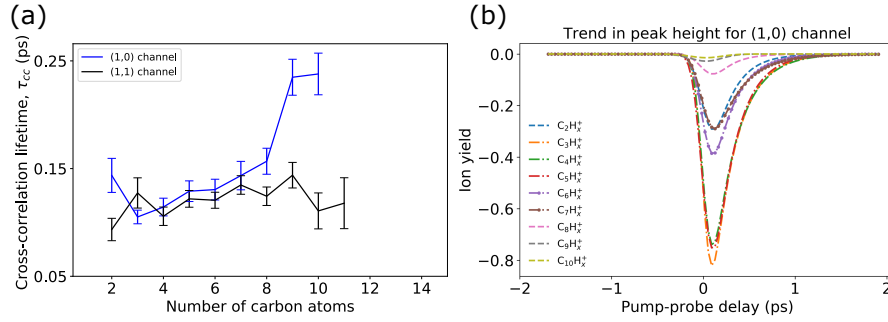
Figure 8.11: A) The cross-correlation times of the two pulses are shown as a function of the number of carbon atoms of the fragments involved in the dissociation process. These are plotted for both, the (1,0) (blue peak) and the (1,1) channel (black peak). B) The intensity of the depletion transient feature is plotted as a function of the number of carbon atoms of all the fragments in their (1,0) channel.

The fitting procedure provides the cross-correlation times of the two pulses (τ_{cc}) for each fragment ion's pump-probe delay time dependent ion yields. These cross-correlation times show the increasing trend for small and medium-sized fragments, which then decreases for the large fragments, $C_{10}H_x^+$ and $C_{11}H_x^+$ (figure 8.11A). τ_{cc} depends on the number of photons absorbed by the system and the dependence can be depicted through the following equation:

$$\tau_{cc}^2 = \frac{\tau_{pump}^2}{n_{pump}} + \frac{\tau_{probe}^2}{n_{probe}} + \tau_{jitter}^2 \tag{8.1}$$

where τ_{pump} and τ_{probe} are the pulse durations of the XUV and Vis pulses, respectively, n_{pump} and n_{probe} are the absorbed XUV photons and Vis photons, respectively, and τ_{jitter} describes the fluctuation in the arrival time of the XUV pulse that affects the pump-probe delay time duration. Since medium-sized fragments have generally lower ionization potentials than the smaller fragments, the small-sized fragment ions are possibly produced through a multiple photons process, which leads to a decrease in the cross-correlation time (τ_{cc}) according to equation (1). The fragmentation channels involving the production of large fragments also include further dissociation, which may be due to multiple photon absorption, leading to higher cross-correlations times for $C_{10}H_x^+$ and $C_{11}H_x^+$. Figure 8.11B shows a decreasing trend in the relative intensity of the transient peak for the (1,0) channel. This trend can be explained *via* by the

fact that large fragments have a dominating (1,0) channel, resulting in less intense depletion as compared to smaller fragments.

8.3 Analysis details for the IR-Vis pump-probe experiments

8.3.1 Pump-probe dependent ion yields

The delay time *vs.* ion yield curves fitted using the software Pump-probe Multiple Channels Markov Chain Monte-Carlo [106] are shown here for all the observed ions. In figure 8.12, all the parent ions and the dehydrogenated monocation are shown. In Figure 8.13 all the channels of monocations of small fragments (C-C_8) are shown. In Figure 8.14 all the channels of monocations of large fragments (C_9-C_{12}) are shown. In Figure 8.15 all the observed dications are shown C_5, C_7, and C_{11}. The transient lifetimes obtained from the electron data are also shown in Figure 8.16.
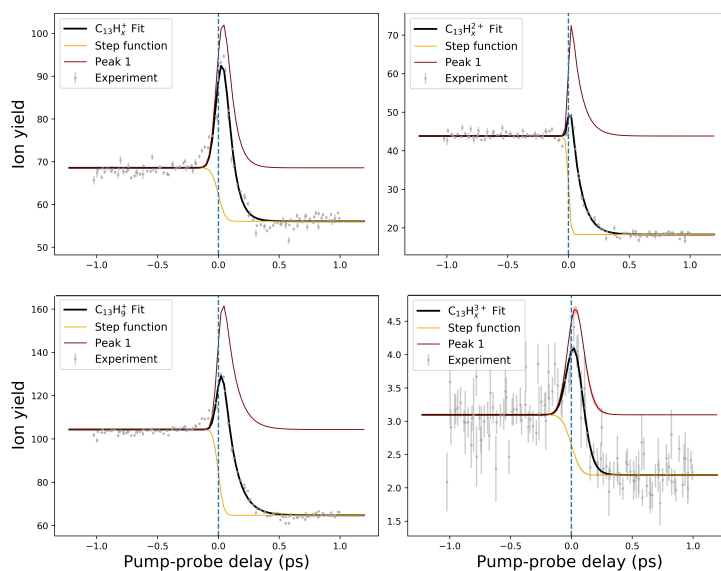
Figure 8.12: The pump-probe delay time *vs.* ion yield curves for parent ions and the dehydrogenated monocation are shown here.
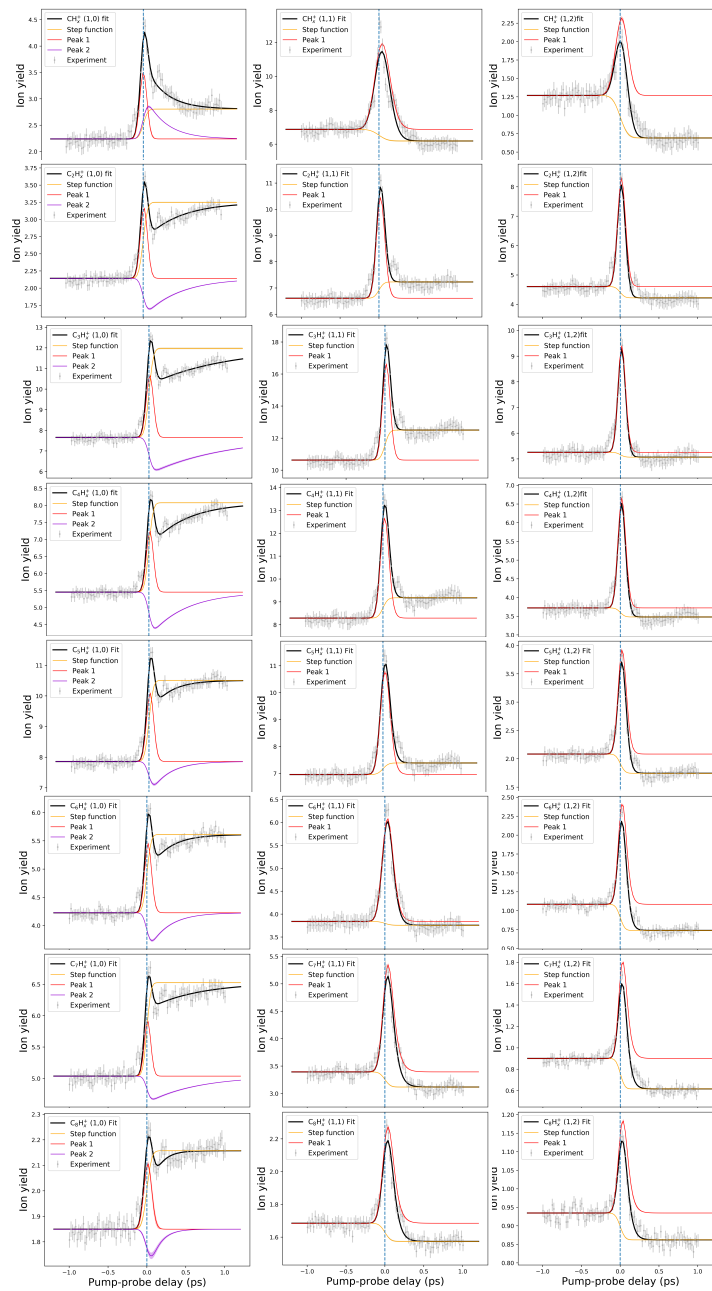
Figure 8.13: The pump-probe delay time *vs.* ion yield curves for all the channels of small fragments (C-C$_8$). The (1,0) channel for all these small fragment ions except carbon monocation shows a transient depletion due to dissociation into the carbon monocation that shows the corresponding transient increase.
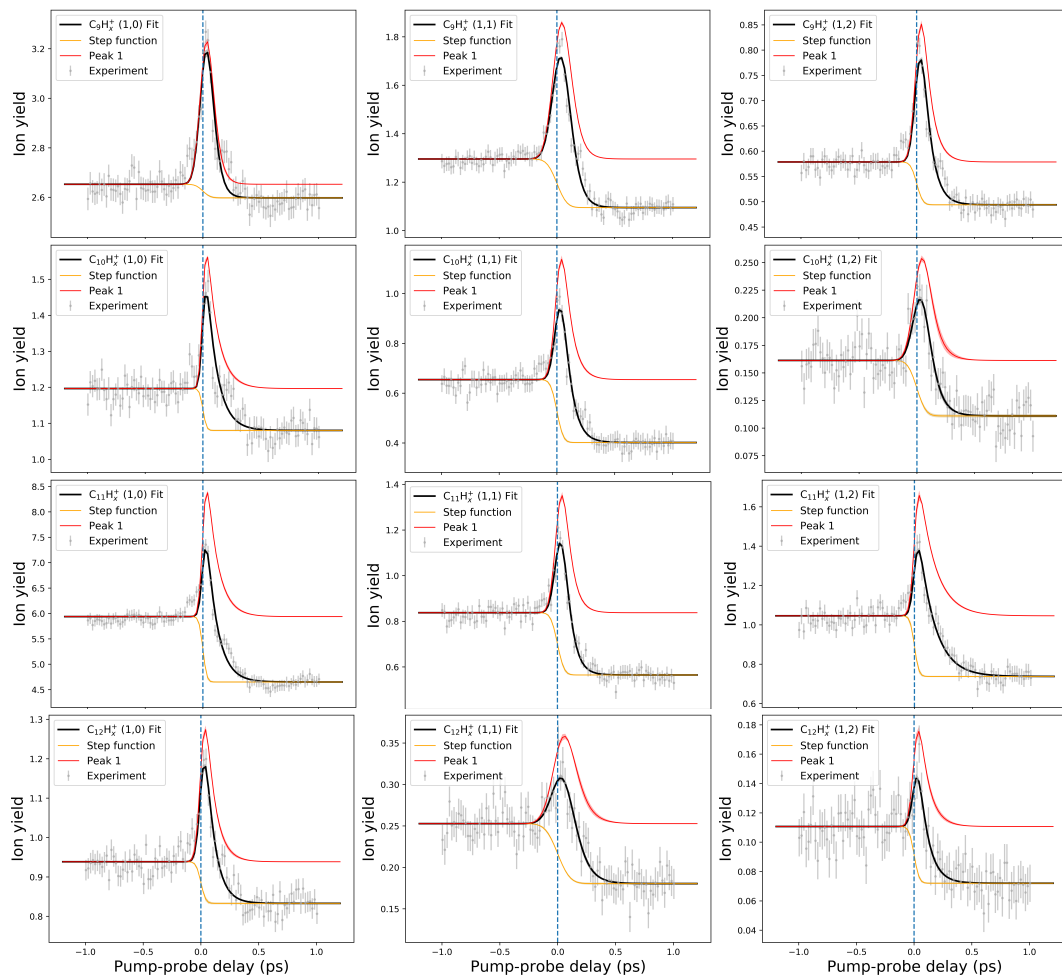
Figure 8.14: The pump-probe delay time *vs.* ion yield curves for all the channels of the large fragments are shown here. A step-down orange curve in the (1,0) channel can be observed in all of them, which points towards their dissociation into small fragments (Figure 8.13), which shows a step-up orange curve in their corresponding (1,0) channel.
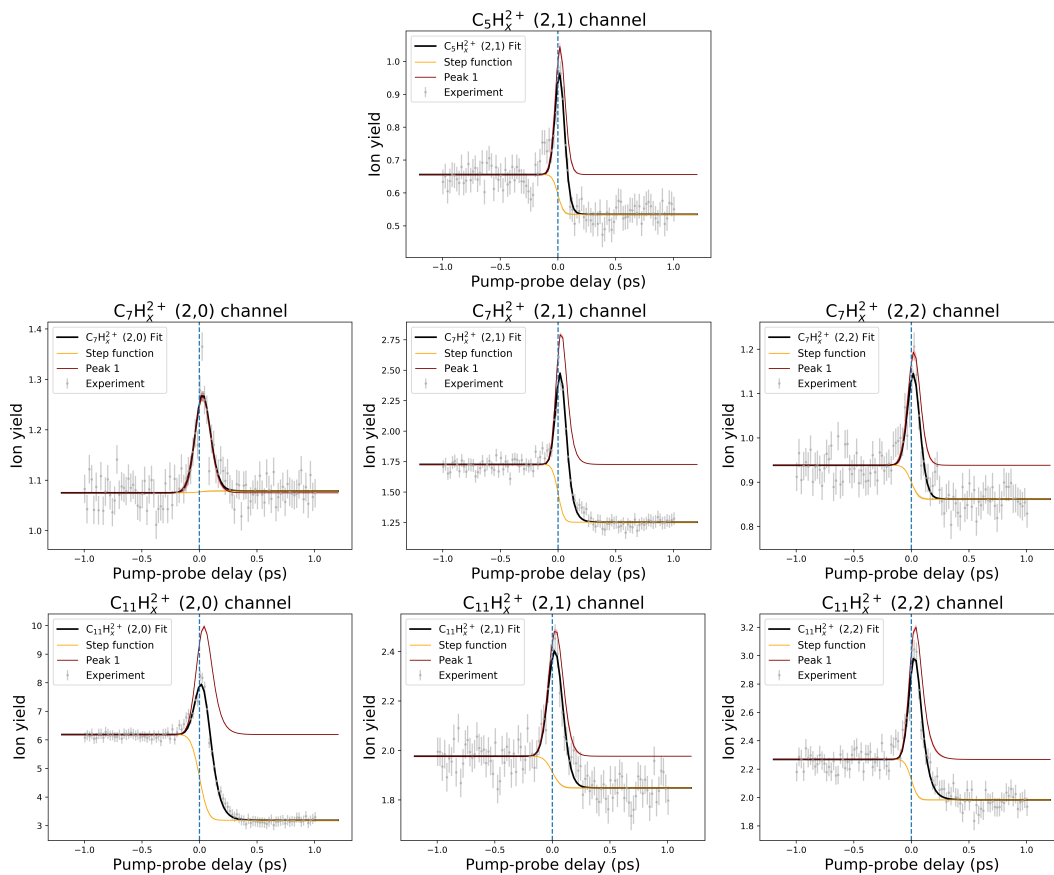
Figure 8.15: The pump-probe delay time *vs.* ion yield curves for the channels observed for a few dications of the large fragments are shown here.
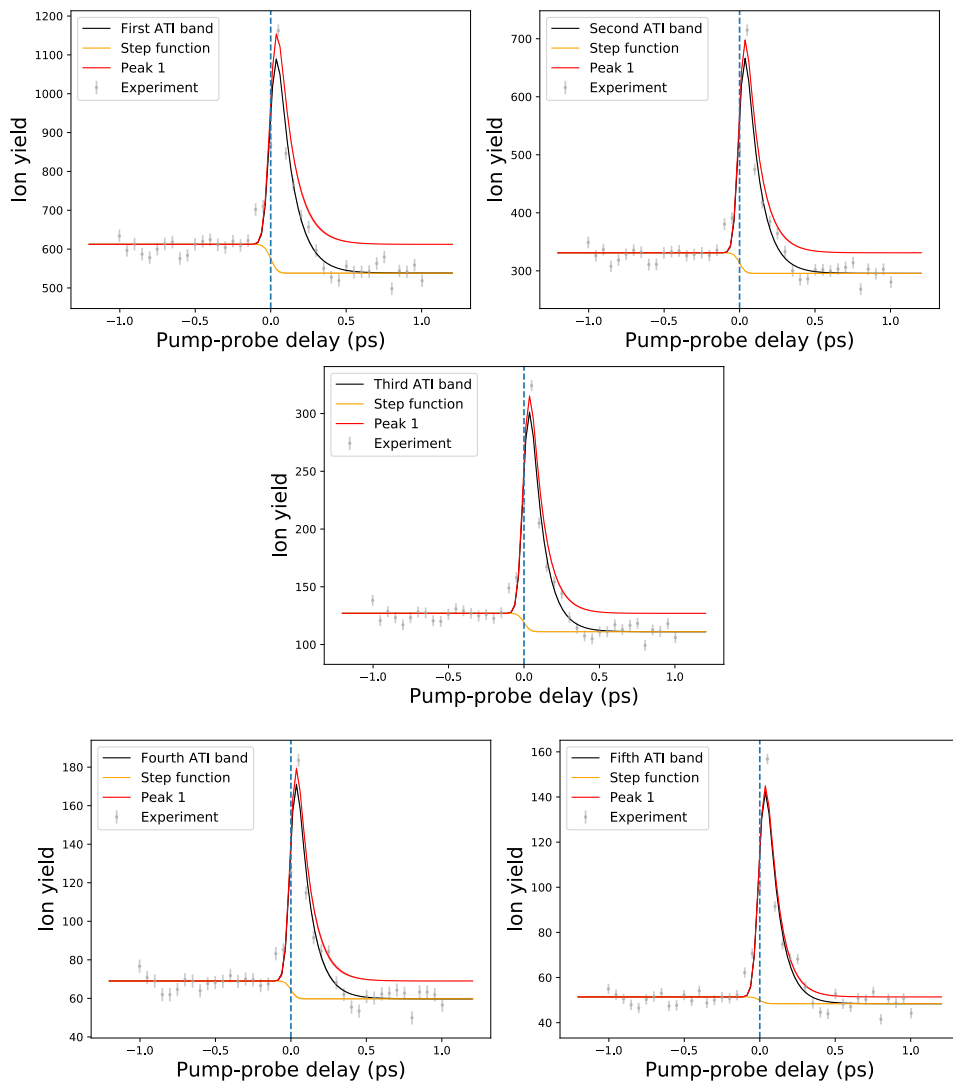
Figure 8.16: The pump-probe delay time *vs.* ion yield curves for the electrons belonging to different ATI bands are plotted here.

8.3.2 Timescales of vibronic relaxation

The transient lifetimes are obtained as a result of the fitted curves shown in the previous subsection. These transient lifetimes indicate the relaxation lifetimes of their precursor. The lifetimes obtained are plotted in Figure 8.17. These are grouped such as the extracted transient lifetimes revealing the vibronic relaxation lifetime of a single species, which is written with each panel. The lifetimes below the 10% of the cross-correlation time correspond to unresolvable dynamics in our experiment.
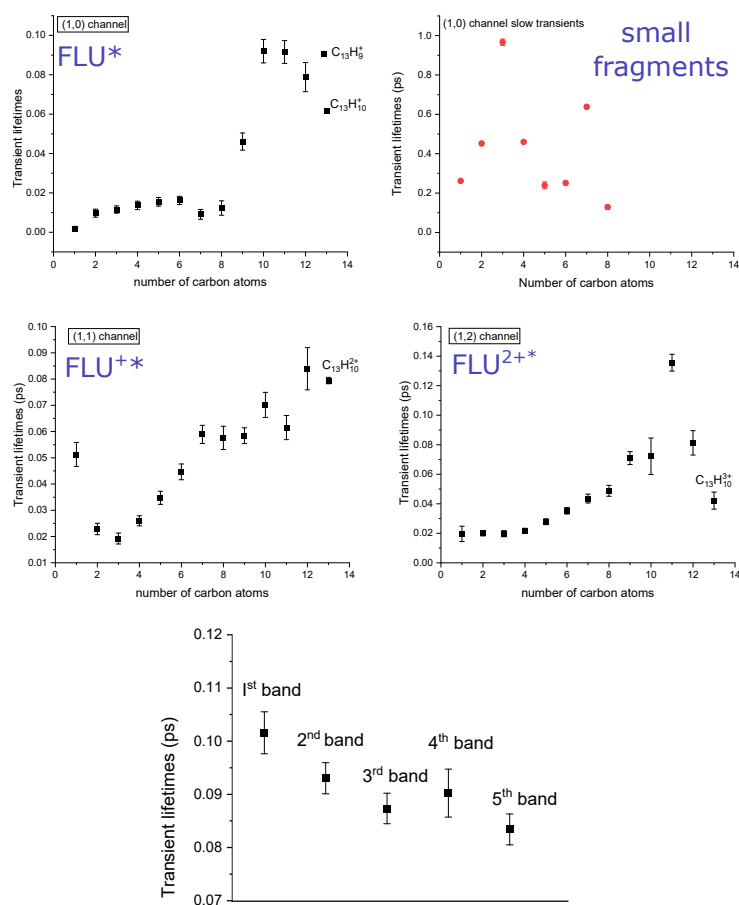
Figure 8.17: The vibronic relaxation lifetime of FLU*, FLU^{+*}, FLU^{2+*}, and small fragments are obtained. The lifetime of the trication is also obtained but only from two channels and are reported to be 27 and 51 fs.

Bibliography

[1] T. P. Snow and B. J. McCall, "Diffuse atomic and molecular clouds", Annual Review of Astronomy and Astrophysics **44**, 367–414 (2006).

[2] T. Dunham Jr, "Interstellar neutral potassium and neutral calcium", Publications of the Astronomical Society of the Pacific **49**, 26–28 (1937).

[3] P. Swings and L. Rosenfeld, "Considerations regarding interstellar molecules", The Astrophysical Journal **86**, 483–486 (1937).

[4] A. McKellar, "Evidence for the molecular origin of some hitherto unidentified interstellar lines", Publications of the Astronomical Society of the Pacific **52**, 187–192 (1940).

[5] B. A. McGuire, "2021 census of interstellar, circumstellar, extragalactic, protoplanetary disk, and exoplanetary molecules", The Astrophysical Journal Supplement Series **259**, 30 (2022).

[6] F. C. Gillett, F. J. Low, and W. A. Stein, "Infrared observations of the planetary nebula NGC 7027", The Astrophysical Journal **149**, L97 (1967).

[7] O. Berné, C. Joblin, M. Rapacioli, J. Thomas, J.-C. Cuillandre, and Y. Deville, "Extended red emission and the evolution of carbonaceous nanograins in NGC 7023", Astronomy & Astrophysics **479**, L41–L44 (2008).

[8] M. Rapacioli, C. Joblin, and P. Boissel, "Spectroscopy of polycyclic aromatic hydrocarbons and very small grains in photodissociation regions", Astronomy & Astrophysics **429**, 193–204 (2004).

[9] A. G. G. M. Tielens, "The aromatic universe", in *Molecular astrophysics* (Cambridge University Press, Jan. 2021), pp. 567–628.

[10] E. Peeters, S. Hony, C. V. Kerckhoven, A. G. G. M. Tielens, L. J. Allamandola, D. M. Hudgins, and C. W. Bauschlicher, "The rich 6 to 9 μm spectrum of interstellar PAHs", A&A **390**, 1089–1113 (2002).

[11] P. Ehrenfreund and M. A. Sephton, "Carbon molecules in space: from astrochemistry to astrobiology", Faraday Discussions **133**, 277 (2006).

[12] E. Herbst and E. F. van Dishoeck, "Complex organic interstellar molecules", Annual Review of Astronomy and Astrophysics **47**, 427–480 (2009).

[13] A. G. G. M. Tielens, "Interstellar polycyclic aromatic hydrocarbon molecules", Annual Review of Astronomy and Astrophysics **46**, 289–337 (2008).

[14] L. M. Ziurys, "The chemistry in circumstellar envelopes of evolved stars: following the origin of the elements to the origin of life", Proceedings of the National Academy of Sciences **103**, 12274–12279 (2006).

[15] J. Cernicharo, M. Agúndez, C. Cabezas, B. Tercero, N. Marcelino, J. R. Pardo, and P. de Vicente, "Pure hydrocarbon cycles in TMC-1: Discovery of ethynyl cyclopropenylidene, cyclopentadiene, and indene", Astronomy & Astrophysics **649**, L15 (2021).

[16] A. M. Burkhardt, K. L. K. Lee, P. B. Changala, C. N. Shingledecker, I. R. Cooke, R. A. Loomis, H. Wei, S. B. Charnley, E. Herbst, M. C. McCarthy, and B. A. McGuire, "Discovery of the Pure Polycyclic Aromatic Hydrocarbon Indene (c-C9H8) with GOTHAM observations of TMC-1", The Astrophysical Journal Letters **913**, L18 (2021).

[17] B. A. McGuire, R. A. Loomis, A. M. Burkhardt, K. L. K. Lee, C. N. Shingledecker, S. B. Charnley, I. R. Cooke, M. A. Cordiner, E. Herbst, S. Kalenskii, M. A. Siebert, E. R. Willis, C. Xue, A. J. Remijan, and M. C. McCarthy, "Detection of two interstellar polycyclic aromatic hydrocarbons via spectral matched filtering", Science **371**, 1265–1269 (2021).

[18] P. J. Sarre, "The diffuse interstellar bands: a major problem in astronomical spectroscopy", Journal of Molecular Spectroscopy **238**, 1–10 (2006).

[19] E. K. Campbell, M. Holz, D. Gerlich, and J. P. Maier, "Laboratory confirmation of C60+ as the carrier of two diffuse interstellar bands", Nature **523**, 322–323 (2015).

[20] A. Chuvilin, U. Kaiser, E. Bichoutskaia, N. A. Besley, and A. N. Khlobystov, "Direct transformation of graphene to fullerene", Nature chemistry **2**, 450–453 (2010).

[21] O. Berné and A. G. G. M. Tielens, "Formation of buckminsterfullerene (C60) in interstellar space", Proceedings of the National Academy of Sciences **109**, 401–406 (2012).

[22] J. Montillaud, C. Joblin, and D. Toublanc, "Evolution of polycyclic aromatic hydrocarbons in photodissociation regions-Hydrogenation and charge states", Astronomy & Astrophysics **552**, A15 (2013).

[23] V. Le Page, T. P. Snow, and V. M. Bierbaum, "Hydrogenation and charge states of PAHs in diffuse clouds. I. development of a model", The Astrophysical Journal Supplement Series **132**, 233 (2001).

[24] J. Zhen, S. R. Castillo, C. Joblin, G. Mulas, H. Sabbah, A. Giuliani, L. Nahon, S. Martin, J.-P. Champeaux, and P. M. Mayer, "VUV photo-processing of PAH cations: Quantitative study on the ionization versus fragmentation processes", The Astrophysical Journal **822**, 113 (2016).

[25] O. V. Egorov, K. Kreckel, K. M. Sandstrom, A. K. Leroy, S. C. O. Glover, B. Groves, J. M. D. Kruijssen, A. T. Barnes, F. Belfiore, F. Bigiel, G. A. Blanc, M. Boquien, Y. Cao, J. Chastenet, M. Chevance, E. Congiu, D. A. Dale, E. Emsellem, K. Grasha, R. S. Klessen, K. L. Larson, D. Liu, E. J. Murphy, H.-A. Pan, I. Pessa, J. Pety, E. Rosolowsky, F. Scheuermann, E. Schinnerer, J. Sutter, D. A. Thilker, E. J. Watkins, and T. G. Williams, *PHANGS-JWST First Results: Destruction of the PAH molecules in HII regions probed by JWST and MUSE*, 2022.

[26] U. of Western Ontario, *Https://physics.uwo.ca/ jcami/dibs.shtml*.

[27] A. Marciniak, V. Despré, T. Barillot, A. Rouzée, M. Galbraith, J. Klei, C.-H. Yang, C. Smeenk, V. Loriot, S. N. Reddy, A. Tielens, S. Mahapatra, A. I. Kuleff, M. Vrakking, and F. Lépine, "XUV excitation followed by ultrafast non-adiabatic relaxation in PAH molecules as a femto-astrochemistry experiment", Nature Communications **6**, `10.1038/ncomms8909` (2015).

[28] J. W. L. Lee, D. S. Tikhonov, P. Chopra, S. Maclot, A. L. Steber, S. Gruet, F. Allum, R. Boll, X. Cheng, S. Düsterer, et al., "Time-resolved relaxation and fragmentation of polycyclic aromatic hydrocarbons investigated in the ultrafast XUV-IR regime", Nature Communications **12**, 1–11 (2021).

[29] D. Garg, J. W. L. Lee, D. S. Tikhonov, P. Chopra, A. L. Steber, A. K. Lemmens, B. Erk, F. Allum, R. Boll, X. Cheng, et al., "Fragmentation dynamics of fluorene explored using ultrafast XUV-Vis pump-probe spectroscopy", Frontiers in Physics, 450 (2022).

[30] A. H. Zewail, "Femtochemistry: atomic-scale dynamics of the chemical bond using ultrafast lasers (nobel lecture)", Angewandte Chemie International Edition **39**, 2586–2631 (2000).

[31] A. H. Zewail, "Laser femtochemistry", Science **242**, 1645–1653 (1988).

[32] H. N. Chapman, P. Fromme, A. Barty, T. A. White, R. A. Kirian, A. Aquila, M. S. Hunter, J. Schulz, D. P. DePonte, U. Weierstall, et al., "Femtosecond X-ray protein nanocrystallography", Nature **470**, 73–77 (2011).

[33] T. Pino, Y. Carpentier, G. Féraud, H. Friha, D. L. Kokkin, T. P. Troy, N. Chalyavi, P. Bréchignac, and T. W. Schmidt, "Electronic spectroscopy of PAHs", PAHs and the Universe, 355–372 (2021).

[34] K. Balewski, W. Brefeld, W. Decking, Y. Li, G. K. Sahoo, and R. Wanzenberg, "PETRA III: A new high brilliance synchrotron radiation source at DESY", EPAC-2004, Lucerne, 2302–2304 (2004).

[35] DESY.

[36] M. Chergui and E. Collet, "Photoinduced structural dynamics of molecular systems mapped by time-resolved X-ray methods", Chemical reviews **117**, 11025–11065 (2017).

[37] R. Jenkins, R. Manne, R. Robin, and C. Senemaud, "IUPAC—nomenclature system for x-ray spectroscopy", X-Ray Spectrometry **20**, 149–155 (1991).

[38] J. A. Bearden and A. F. Burr, "Reevaluation of X-ray atomic energy levels", Reviews of Modern Physics **39**, 125 (1967).

[39] A. R. Milosavljević, A. Giuliani, and C. Nicolas, "Gas-phase near-edge x-ray absorption fine structure (NEXAFS) spectroscopy of nanoparticles, biopolymers, and ionic species", in *X-ray and Neutron techniques for Nanomaterials Characterization* (Springer, 2016), pp. 451–505.

[40] J. Stöhr, *NEXAFS spectroscopy*, Vol. 25 (Springer Science & Business Media, 1992).

[41] F. Neese, "The ORCA program system", Wiley Interdisciplinary Reviews: Computational Molecular Science **2**, 73–78 (2012).

[42] E. Runge and E. K. U. Gross, "Density-functional theory for time-dependent systems", Physical review letters **52**, 997 (1984).

[43] R. E. Stratmann, G. E. Scuseria, and M. J. Frisch, "An efficient implementation of time-dependent density-functional theory for the calculation of excitation energies of large molecules", The Journal of chemical physics **109**, 8218–8224 (1998).

[44] A. D. Laurent and D. Jacquemin, "TD-DFT benchmarks: a review", International Journal of Quantum Chemistry **113**, 2019–2039 (2013).

[45] C. Joblin, A. G. G. M. Tielens, H. Kaneda, T. Onaka, I. Sakon, D. Ishihara, A. Mouri, M. Yamagishi, and A. Yasuda, "PAH evolution in the harsh environment of the ISM", European Astronomical Society Publications Series **46**, 157–168 (2011).

[46] M. H. Stockett, J. N. Bull, J. T. Buntine, E. Carrascosa, M. Ji, N. Kono, H. T. Schmidt, and H. Zettergren, "Unimolecular fragmentation and radiative cooling of isolated PAH ions: a quantitative study", The Journal of Chemical Physics **153**, 154303 (2020).

[47] M. Hervé, V. Despré, P. C. Nash, V. Loriot, A. Boyer, A. Scognamiglio, G. Karras, R. Brédy, E. Constant, A. G. G. M. Tielens, A. I. Kuleff, and F. Lépine, "Ultrafast dynamics of correlation bands following XUV molecular photoionization", Nature Physics **17**, 327–331 (2020).

[48] A. Boyer, M. Hervé, V. Despré, P. C. Nash, V. Loriot, A. Marciniak, A. Tielens, A. Kuleff, and F. Lépine, "Ultrafast vibrational relaxation dynamics in XUV-excited polycyclic aromatic hydrocarbon molecules", Physical Review X **11**, 041012 (2021).

[49] V. S. Reddy, S. Ghanta, and S. Mahapatra, "First principles quantum dynamical investigation provides evidence for the role of polycyclic aromatic hydrocarbon radical cations in interstellar physics", Physical Review Letters **104**, 111102 (2010).

[50] W. Domcke and D. R. Yarkony, "Role of conical intersections in molecular spectroscopy and photoinduced chemical dynamics", Annual Review of Physical Chemistry **63**, 325–352 (2012).

[51] M. C. E. Galbraith, S. Scheit, N. V. Golubev, G. Reitsma, N. Zhavoronkov, V. Despré, F. Lépine, A. I. Kuleff, M. J. J. Vrakking, O. Kornilov, H. Köppel, and J. Mikosch, "Few-femtosecond passage of conical intersections in the benzene cation", Nature Communications **8**, `10.1038/s41467-017-01133-y` (2017).

[52] B. F. E. Curchod and T. J. Martínez, "Ab initio nonadiabatic quantum molecular dynamics", Chemical Reviews **118**, 3305–3336 (2018).

[53] C. E. Crespo-Hernández, G. Burdzinski, and R. Arce, "Environmental photochemistry of nitro-PAHs: direct observation of ultrafast intersystem crossing in 1-nitropyrene", The Journal of Physical Chemistry A **112**, 6313–6319 (2008).

[54] J. Cao, H. Ihee, and A. H. Zewail, "Ultrafast electron diffraction and direct observation of transient structures in a chemical reaction", Proceedings of the National Academy of Sciences **96**, 338–342 (1999).

[55] W. E. Stephens, "A pulsed mass spectrometer with time dispersion", Phys. Rev. **69**, 691 (1946).

[56] A. E. Cameron and D. F. Eggers Jr, "An ion "velocitron"", Review of Scientific Instruments **19**, 605–607 (1948).

[57] W. C. Wiley and I. H. McLaren, "Time-of-flight mass spectrometer with improved resolution", Review of scientific instruments **26**, 1150–1157 (1955).

[58] J. W. G. Mastenbroek, C. A. Taatjes, K. Nauta, M. H. M. Janssen, and S. Stolte, "Two-dimensional imaging of the photolysis of oriented molecules", The Journal of Physical Chemistry **99**, 4360–4363 (1995).

[59] D. W. Chandler and P. L. Houston, "Two-dimensional imaging of state-selected photodissociation products detected by multiphoton ionization", The Journal of chemical physics **87**, 1445–1447 (1987).

[60] A. T. J. B. Eppink and D. H. Parker, "Velocity map imaging of ions and electrons using electrostatic lenses: application in photoelectron and photofragment ion imaging of molecular oxygen", Review of Scientific Instruments **68**, 3477–3484 (1997).

[61] D. W. Chandler, J. W. Thoman Jr, M. H. Janssen, and D. H. Parker, "Photofragment imaging: the 266 nm photodissociation of CH3I", Chemical physics letters **156**, 151–158 (1989).

[62] J. N. Bull, J. W. L. Lee, S. H. Gardiner, and C. Vallance, "Account: an introduction to velocity-map imaging mass spectrometry (VMImMS)", European Journal of Mass Spectrometry **20**, 117–129 (2014).

[63] T. Gerber, Y. Liu, G. Knopp, P. Hemberger, A. Bodi, P. Radi, and Y. Sych, "Charged particle velocity map image reconstruction with one-dimensional projections of spherical functions", Review of Scientific Instruments **84**, 033101 (2013).

[64] S. Schippers, T. Buhr, A. Borovik, K. Holste, A. Perry-Sassmannshausen, K. Mertens, S. Reinwardt, M. Martins, S. Klumpp, K. Schubert, S. Bari, R. Beerwerth, S. Fritzsche, S. Ricz, J. Hellhund, and A. Müller, "The photon-ion merged-beams experiment PIPE at PETRA III—the first five years", X-Ray Spectrometry **49**, 11–20 (2019).

[65] M. Waitz, D. Metz, J. Lower, C. Schober, M. Keiling, M. Pitzer, K. Mertens, M. Martins, J. Viefhaus, S. Klumpp, T. Weber, H. Schmidt-Böcking, L. Schmidt, F. Morales, S. Miyabe, T. Rescigno, C. McCurdy, F. Martìn, J. Williams, M. Schöffler, T. Jahnke, and R. Dörner, "Two-particle interference of electron pairs on a molecular level", Physical Review Letters **117**, 083002 (2016).

[66] M. Waitz, R. Y. Bello, D. Metz, J. Lower, F. Trinter, C. Schober, M. Keiling, U. Lenz, M. Pitzer, K. Mertens, M. Martins, J. Viefhaus, S. Klumpp, T. Weber, L. P. H. Schmidt, J. B. Williams, M. S. Schöffler, V. V. Serov, A. S. Kheifets, L. Argenti, A. Palacios, F. Martìn, T. Jahnke, and R. Dörner, "Imaging the square of the correlated two-electron wave function of a hydrogen molecule", Nature Communications **8**, `10.1038/s41467-017-02437-9` (2017).

[67] J. Viefhaus, F. Scholz, S. Deinert, L. Glaser, M. Ilchen, J. Seltmann, P. Walter, and F. Siewert, "The variable polarization XUV beamline P04 at PETRA III: optics, mechanics and their performance", Nuclear Instruments and Methods in Physics Research Section A: Accelerators, Spectrometers, Detectors and Associated Equipment **710**, 151–154 (2013).

[68] R. Trassl, P. Hathiramani, F. Broetz, J. B. Greenwood, R. W. McCullough, M. Schlapp, and E. Salzborn, "Characterization and recent modifications of a compact 10 GHz electron cyclotron resonance (ECR) ion source for atomic physics experiments", Physica Scripta **1997**, 380 (1997).

[69] F. Broetz, R. Trassl, R. W. McCullough, W. Arnold, and E. Salzborn, "Design of compact all-permanent magnet electron cyclotron resonance (ECR) ion sources for atomic physics experiments", Physica Scripta **T92**, 278–280 (2001).

[70] S. Schippers, A. D. Kilcoyne, R. A. Phaneuf, and A. Müller, "Photoionisation of ions with synchrotron radiation: from ions in space to atoms in cages", Contemporary Physics **57**, 215–229 (2016).

[71] M. Domke, C. Xue, A. Puschmann, T. Mandel, E. Hudson, D. Shirley, and G. Kaindl, "Carbon and oxygen K-edge photoionization of the CO molecule", Chemical physics letters **173**, 122–128 (1990).

[72] P. Chopra, "Astrochemically relevant Polycyclic aromatic Hydrocarbons Investigated using Ultrafast Pump-probe Spectroscopy and Near-edge X-ray Absorption Fine Structure Spectroscopy", en, PhD thesis (2022).

[73] J. Feldhaus, "FLASH—the first soft x-ray free electron laser (FEL) user facility", Journal of Physics B: Atomic, Molecular and Optical Physics **43**, 194002 (2010).

[74] B. Erk, J. P. Müller, C. Bomme, R. Boll, G. Brenner, H. N. Chapman, J. Correa, S. Düsterer, S. Dziarzhytski, S. Eisebitt, H. Graafsma, S. Grunewald, L. Gumprecht, R. Hartmann, G. Hauser, B. Keitel, C. von Korff Schmising, M. Kuhlmann, B. Manschwetus, L. Mercadier, E. Müller, C. Passow, E. Plönjes, D. Ramm, D. Rompotis, A. Rudenko, D. Rupp, M. Sauppe, F. Siewert, D. Schlosser, L. Strüder, A. Swiderski, S. Techert, K. Tiedtke, T. Tilp, R. Treusch, I. Schlichting, J. Ullrich, R. Moshammer, T. Möller, and D. Rolles, "CAMP@FLASH: an end-station for imaging, electron- and ion-spectroscopy, and pump–probe experiments at the FLASH free-electron laser", Journal of Synchrotron Radiation **25**, 1529–1540 (2018).

[75] P. Kirkpatrick and A. V. Baez, "Formation of optical images by X-rays", JOSA **38**, 766–774 (1948).

[76] O. Altenmueller, R. Larsen, and G. A. Loew, "Investigations of traveling-wave separators for the stanford two-mile linear accelerator", Review of Scientific Instruments **35**, 438–442 (1964).

[77] C. Behrens, N. Gerasimova, C. Gerth, B. Schmidt, E. A. Schneidmiller, S. Serkez, S. Wesch, and M. V. Yurkov, "Constraints on photon pulse duration from longitudinal electron beam diagnostics at a soft x-ray free-electron laser", Physical Review Special Topics - Accelerators and Beams **15**, 030707 (2012).

[78] B. Faatz, E. Plönjes, S. Ackermann, A. Agababyan, V. Asgekar, V. Ayvazyan, S. Baark, N. Baboi, V. Balandin, N. Von Bargen, et al., "Simultaneous operation of two soft x-ray free-electron lasers driven by one linear accelerator", New Journal of physics **18**, 062002 (2016).

[79] K. Honkavaara, "Flash status",

[80] H. Redlin, A. Al-Shemmary, A. Azima, N. Stojanovic, F. Tavella, I. Will, and S. Düsterer, "The FLASH pump–probe laser system: setup, characterization and optical beamlines", Nuclear Instruments and Methods in Physics Research Section A: Accelerators, Spectrometers, Detectors and Associated Equipment **635**, S88–S93 (2011).

[81] S. Schulz, I. Grguraš, C. Behrens, H. Bromberger, J. T. Costello, M. K. Czwalinna, M. Felber, M. C. Hoffmann, M. Ilchen, H. Y. Liu, T. Mazza, M. Meyer, S. Pfeiffer, P. Prędki, S. Schefer, C. Schmidt, U. Wegner, H. Schlarb, and A. L. Cavalieri, "Femtosecond all-optical synchronization of an X-ray free-electron laser", Nature Communications **6**, `10.1038/ncomms6938` (2015).

[82] E. Savelyev, R. Boll, C. Bomme, N. Schirmel, H. Redlin, B. Erk, S. Düsterer, E. Müller, H. Höppner, S. Toleikis, et al., "Jitter-correction for IR/UV-XUV pump-probe experiments at the FLASH free-electron laser", New Journal of Physics **19**, 043009 (2017).

[83] U. Even, "The even-lavie valve as a source for high intensity supersonic beam", EPJ Techniques and Instrumentation **2**, `10.1140/epjti/s40485-015-0027-5` (2015).

[84] P. pulsed valves, *Http://ph.parker.com/us/12051/en/pulse-valves-miniature-high-speed-high-vacuum-dispense-valve.*

[85] A. T. Clark, J. P. Crooks, I. Sedgwick, R. Turchetta, J. W. Lee, J. J. John, E. S. Wilman, L. Hill, E. Halford, C. S. Slater, et al., "Multimass velocity-map imaging with the pixel imaging mass spectrometry (PImMS) sensor: an ultrafast event-triggered camera for particle imaging", The Journal of Physical Chemistry A **116**, 10897–10903 (2012).

[86] K. Amini, S. Blake, M. Brouard, M. B. Burt, E. Halford, A. Lauer, C. S. Slater, J. W. L. Lee, and C. Vallance, "Three-dimensional imaging of carbonyl sulfide and ethyl iodide photodissociation using the pixel imaging mass spectrometry camera", Review of Scientific Instruments **86**, 103113 (2015).

[87] S. Schippers, "Analytical expression for the convolution of a fano line profile with a gaussian", Journal of Quantitative Spectroscopy and Radiative Transfer **219**, 33–36 (2018).

[88] K. Schulz, G. Kaindl, M. Domke, J. D. Bozek, P. A. Heimann, A. S. Schlachter, and J. M. Rost, "Observation of new rydberg series and resonances in doubly excited helium at ultrahigh resolution", Physical review letters **77**, 3086 (1996).

[89] H. Kjeldsen, "Photoionization cross sections of atomic ions from merged-beam experiments", Journal of Physics B: Atomic, Molecular and Optical Physics **39**, R325 (2006).

[90] M. Abramowitz and I. A. Stegun, *Handbook of mathematical functions with formulas, graphs, and mathematical tables*, Vol. 55 (US Government printing office, 1964).

[91] G. P. M. Poppe and C. M. J. Wijers, "More efficient computation of the complex error function", ACM Transactions on Mathematical Software (TOMS) **16**, 38–46 (1990).

[92] M. Sampoorna, K. N. Nagendra, and H. Frisch, "Generalized Voigt functions and their derivatives", Journal of Quantitative Spectroscopy and Radiative Transfer **104**, 71–85 (2007).

[93] J. Humlíček, "An efficient method for evaluation of the complex probability function: the Voigt function and its derivatives", Journal of Quantitative Spectroscopy and Radiative Transfer **21**, 309–313 (1979).

[94] R. J. Wells, "Rapid approximation to the Voigt/Faddeeva function and its derivatives", Journal of Quantitative Spectroscopy and Radiative Transfer **62**, 29–48 (1999).

[95] F. Schreier, "Optimized implementations of rational approximations for the Voigt and complex error function", Journal of Quantitative Spectroscopy and Radiative Transfer **112**, 1010–1025 (2011).

[96] M. R. Zaghloul and A. N. Ali, "Algorithm 916: computing the Faddeeva and Voigt functions", ACM Transactions on Mathematical Software (TOMS) **38**, 1–22 (2012).

[97] S. Schippers, A. Müller, B. M. McLaughlin, A. Aguilar, C. Cisneros, E. D. Emmons, M. F. Gharaibeh, and R. A. Phaneuf, "Photoionization studies of the B+ valence shell: experiment and theory", Journal of Physics B: Atomic, Molecular and Optical Physics **36**, 3371 (2003).

[98] S. Schippers, S. Kieslich, A. Müller, G. Gwinner, M. Schnell, A. Wolf, A. Covington, M. E. Bannister, and L.-B. Zhao, "Interference effects in the photorecombination of argon like Sc 3+ ions: Storage-ring experiment and theory", Physical Review A **65**, 042723 (2002).

[99] S. Scully, I. Álvarez, C. Cisneros, E. Emmons, M. Gharaibeh, D. Leitner, M. Lubell, A. Müller, R. Phaneuf, R. Püttner, et al., "Doubly excited resonances in the photoionization spectrum of Li+: experiment and theory", Journal of Physics B: Atomic, Molecular and Optical Physics **39**, 3957 (2006).

[100] G. Van Rossum and F. L. Drake Jr, *Python reference manual* (Centrum voor Wiskunde en Informatica Amsterdam, 1995).

[101] A. T. Clark, J. P. Crooks, I. Sedgwick, R. Turchetta, J. W. L. Lee, J. J. John, E. S. Wilman, L. Hill, E. Halford, C. S. Slater, B. Winter, W. H. Yuen, S. H. Gardiner, M. L. Lipciuc, M. Brouard, A. Nomerotski, and C. Vallance, "Multimass velocity-map imaging with the pixel imaging mass spectrometry (PImMS) sensor: an ultra-fast event-triggered camera for particle imaging", The Journal of Physical Chemistry A **116**, 10897–10903 (2012).

[102] K. Amini, S. Blake, M. Brouard, M. B. Burt, E. Halford, A. Lauer, C. S. Slater, J. W. L. Lee, and C. Vallance, "Three-dimensional imaging of carbonyl sulfide and ethyl iodide photodissociation using the pixel imaging mass spectrometry camera", Review of Scientific Instruments **86**, 103113 (2015).

[103] D. S. Tikhonov, D. Garg, and P. Chopra, *The campfancyanalysis software*, 2019.

[104] D. S. Tikhonov and D. Garg, *Campfancyanalyis home* (2019).

[105] A. Jaycen, "Open-source software compares abel transforms for easy use", Scilight **2019**, 260003 (2019).

[106] D. S. Tikhonov, *Mcmcmcfitting*, 2019.

[107] S. P. A. H. Zewail, "Femtosecond real time probing of reactions XXII kinetic description of probe absorption fluorescence depletion and mass spectrometry", Molecular Physics **89**, 1455–1502 (1996).

[108] D. S. Tikhonov, *Https://confluence.desy.de/display/cfa/tof-tof+covariance+analysis* (2019).

[109] L. J. Frasinski, "Covariance mapping techniques", Journal of Physics B: Atomic, Molecular and Optical Physics **49**, 152004 (2016).

[110] C. S. Slater, S. Blake, M. Brouard, A. Lauer, C. Vallance, J. J. John, R. Turchetta, A. Nomerotski, L. Christensen, J. H. Nielsen, M. P. Johansson, and H. Stapelfeldt, "Covariance imaging experiments using a pixel-imaging mass-spectrometry camera", Physical Review A **89**, 011401 (2014).

[111] C. S. Slater, S. Blake, M. Brouard, A. Lauer, C. Vallance, C. S. Bohun, L. Christensen, J. H. Nielsen, M. P. Johansson, and H. Stapelfeldt, "Coulomb-explosion imaging using a pixel-imaging mass-spectrometry camera", Physical Review A **91**, 053424 (2015).

[112] C. Vallance, D. Heathcote, and J. W. L. Lee, "Covariance-map imaging: a powerful tool for chemical dynamics studies", The Journal of Physical Chemistry A **125**, 1117–1133 (2021).

[113] D. S. McClure, "First singlet-singlet electronic transition in the phenanthrene molecule and the band structure of the phenanthrene crystal", The Journal of Chemical Physics **25**, 481–485 (1956).

[114] S. Düsterer, M. Rehders, A. Al-Shemmary, C. Behrens, G. Brenner, O. Brovko, M. DellAngela, M. Drescher, B. Faatz, J. Feldhaus, U. Frühling, N. Gerasimova, N. Gerken, C. Gerth, T. Golz, A. Grebentsov, E. Hass, K. Honkavaara, V. Kocharian, M. Kurka, T. Limberg, R. Mitzner, R. Moshammer, E. Plönjes, M. Richter, J. Rönsch-Schulenburg, A. Rudenko, H. Schlarb, B. Schmidt, A. Senftleben, E. Schneidmiller, B. Siemer, F. Sorgenfrei, A. Sorokin, N. Stojanovic, K. Tiedtke, R. Treusch, M. Vogt, M. Wieland, W. Wurth, S. Wesch, M. Yan, M. Yurkov, H. Zacharias, and S. Schreiber, "Development of experimental techniques for the characterization of ultrashort photon pulses of extreme ultraviolet free-electron lasers", Physical Review Special Topics - Accelerators and Beams **17**, 120702 (2014).

[115] D. A. Dahl, J. E. Delmore, and A. D. Appelhans, "SIMION PC/PS2 electrostatic lens design program", Review of Scientific Instruments **61**, 607–609 (1990).

[116] A. Steber and E. Müller, *Https://stash.desy.de/projects/cs/repos/pah/browse*, 2016.

[117] L. J. Frasinski, K. Codling, and P. A. Hatherly, "Covariance mapping: a correlation method applied to multiphoton multiple ionization", Science **246**, 1029–1031 (1989).

[118] R. Dabestani and I. N. Ivanov, "A compilation of physical, spectroscopic and photophysical properties of polycyclic aromatic hydrocarbons", Photochemistry and Photobiology **70**, 10–34 (1999).

[119] A. I. S. Holm, H. A. B. Johansson, H. Cederquist, and H. Zettergren, "Dissociation and multiple ionization energies for five polycyclic aromatic hydrocarbon molecules", The Journal of Chemical Physics **134**, 044301 (2011).

[120] M. V. Vinitha, A. M. Nair, K. Ramanathan, and U. R. Kadhane, "Understanding dehydrogenation sequence in fluorene$^+$ by multiphoton ionisation-excitation processes", International Journal of Mass Spectrometry **471**, 116704 (2022).

[121] C. Bagdia, S. Biswas, A. Mandal, S. Bhattacharjee, and L. C. Tribedi, "Ionization and fragmentation of fluorene upon 250 keV proton impact", The European Physical Journal D **75**, `10.1140/epjd/s10053-020-00001-7` (2021).

[122] B. J. West, L. Lesniak, and P. M. Mayer, "Why do large ionized polycyclic aromatic hydrocarbons not lose C_2H_2?", The Journal of Physical Chemistry A **123**, 3569–3574 (2019).

[123] A. Sánchez, K. Amini, S.-J. Wang, T. Steinle, B. Belsa, J. Danek, A.-T. Le, X. Liu, R. Moshammer, T. Pfeifer, et al., "Molecular structure retrieval directly from laboratory-frame photoelectron spectra in laser-induced electron diffraction", Nature communications **12**, 1–9 (2021).

[124] F. A. Ilkov, J. E. Decker, and S. L. Chin, "Ionization of atoms in the tunnelling regime with experimental evidence using Hg atoms", Journal of Physics B: Atomic, Molecular and Optical Physics **25**, 4005 (1992).

[125] R. Dabestani and I. N. Ivanov, "A compilation of physical, spectroscopic and photophysical properties of polycyclic aromatic hydrocarbons", Photochemistry and photobiology **70**, 10–34 (1999).

[126] S. Tobita, S. Leach, H. Jochims, E. Rühl, E. Illenberger, and H. Baumgärtel, "Single-and double-ionization potentials of polycyclic aromatic hydrocarbons and fullerenes by photon and electron impact", Canadian Journal of Physics **72**, 1060–1069 (1994).

[127] M. J. DeWitt and R. J. Levis, "Near-infrared femtosecond photoionization/dissociation of cyclic aromatic hydrocarbons", The Journal of chemical physics **102**, 8670–8673 (1995).

[128] N. Nakashima, S. Shimizu, T. Yatsuhashi, S. Sakabe, and Y. Izawa, "Large molecules in high-intensity laser fields", Journal of Photochemistry and Photobiology C: Photochemistry Reviews **1**, 131–143 (2000).

[129] K. W. D. Ledingham and R. P. Singhal, "High intensity laser mass spectrometry—a review", International journal of mass spectrometry and ion processes **163**, 149–168 (1997).

[130] F. Neese, "The ORCA program system", WIREs Computational Molecular Science **2**, 73–78 (2011).

Acknowledgements

I am grateful to pursue my doctoral research at the DESY research institute, which offers great opportunities to bring scientific ideas to reality. I thank the International Max Planck research school (IMPRS) to provide me access to useful courses during my Ph.D. The projects would not have been possible without the great collaboration around the world and the research funding agencies.

I would like to acknowledge the great guidance, support, opportunities, flexibility, and ideas from my Ph.D. supervisor, Prof. Dr. Melanie Schnell. I am glad to have all-time support from Dr. Denis S. Tikhonov and Dr. Jason W. L. Lee. I would like to thank Dr. Denis, for all the scientific (specifically about the analysis), intellectual, and fun discussions that motivated me to keep on going on even during challenging times and make me think out of the box. I thank Dr. Jason for giving me the tremendous opportunities to learn a lot about multiple beamlines and especially learning a lot about the imaging technique. I thank a lot to Dr. Pragya Chopra for starting me up with my Ph. D. projects and also for making me welcome in Germany (also Dr. Rizallina Tama Saragi and Pranay Bhalla) with her companionship which made life easy for me. I thank Sonu Kumar for helping me with the technical details of the projects. I thank Freya Berggoetz for her help in providing feedback and german translation on short notice. I would like to thank all my group members (Dr. Dan, Dr. Pablo, Dr. Ben, Dr. Mariyam, Dr. Wenhao, Dr. Wiexing, Dr. Maria, Dr. Sergio, Dr. Amanda, Dr. Cristobol, Dr. Fan, and Dr. Alcides) for being very friendly and nice. Together the group activities provide a very comfortable environment to carry out research with flexible ideas sharing.

I am very glad to thank my parents, Mr. Mohan Lal Garg and Mrs. Sangeeta Garg, who are always very supportive of my education and encouraged me to achieve more every time. I thank my siblings Tushar Garg and Purvashi Garg (and her husband Abhinav Garg) for always being so proud of me even in my failures. I would really like to thank my fiance Mr. Aniket Vats for just being there, supporting my goals unconditionally in every possible way, and motivating me to never settle for less. I am very much thankful to my Master's thesis supervisor who introduced spectroscopy to me and is the starting point of my research.

I would like to thank my friends Alisha, Arun, Akshat, Bidisha, Denis, Dipali,

Eva, Freya, Gayatri, Himanshi, Kritika, Kunj, Mukhtar, Nidhi, Perveer, Pragya, Sheetal, Sonu, Sravya, Srashta, Surabhi, and more friends without whom it would be impossible to have fun-loving Ph.D..

<u>Declaration on oath</u>

I, Diksha Garg, hereby declare in lieu of oath that I have written this dissertation myself and that I have not used any auxiliary materials or sources other than those indicated.

Hamburg, **02.02.2023**

Signature of the doctoral student